CHALMERS

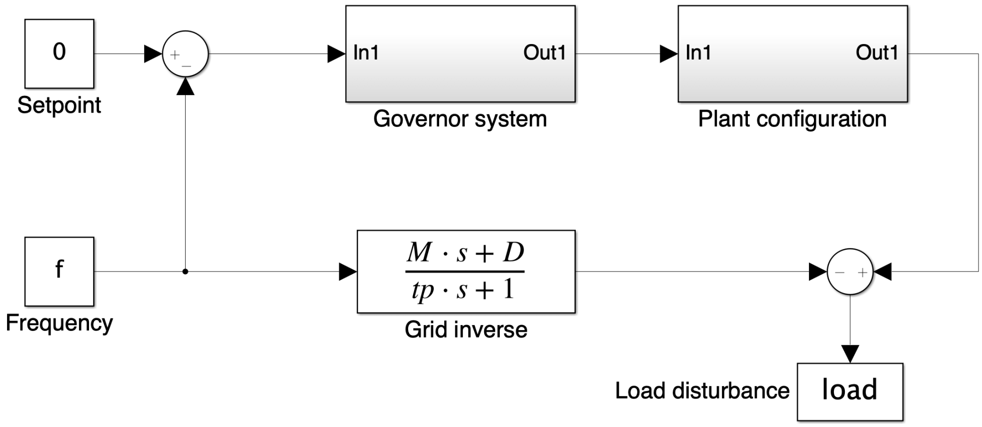

Wind power penetration levels impact on net load variations using an inverse grid model

Different generation mixes and inertia estimations impact on the power system frequency quality and control

Master of Science Thesis in Electric Power Engineering

ERIK WEIHS

Department of Electrical Engineering
CHALMERS UNIVERSITY OF TECHNOLOGY
Gothenburg, Sweden 2019

MASTER THESIS EENX30

Wind power penetration levels impact on net load variations using an inverse grid model

Different generation mixes and inertia estimations impact on the power system frequency quality and control

CHALMERS

Department of Energy and Environment
Division of Electric Power Engineering
CHALMERS UNIVERSITY OF TECHNOLOGY
Gothenburg, Sweden 2019

Wind power penetration levels impact on net load variations using an inverse grid model
Different generation mixes and inertia estimations impact on the power system frequency quality and control

Erik Weihs

Department of Energy and Environment
Division of Electric Power Engineering
Chalmers University of Technology
SE-412 96 Gothenburg
Sweden
Telephone +46(0)76 831 1719

Thesis supervisor
Mattias Persson, Ph.D. EPE, Researcher
Research Institutes of Sweden
Telephone +46(0)70 356 50 18
Email mattias.persson@ri.se

Thesis examiner
Peiyuan Chen, Associate professor
Department of Energy and Environment
Division of Electric Power Engineering
Chalmers University of Technology, Gothenburg, Sweden
Telephone +46(0)31 772 16 39
E-mail peiyuan@chalmers.se

Typeset in LaTeX
Gothenburg, Sweden 2019

Abstract

Recently, the renewable energy production and integration of intermittent energy sources have increased in the Nordic Power System (NPS) and are replacing the aging nuclear power plants. In order to address certain concerns regarding a lower inertia power system a grid inverse model of the power system is proposed with governor and plant configurations for different generation mixes in the Nordic region. The purpose of the grid inverse model is to evaluate how the net load disturbances, and thus the frequency quality, is affected by different inertia estimations and weather years for distinct scenarios for the year 2040. In the NPS, the frequency containment reserve for normal operation is mainly provided by hydro units and is modelled by a hydro-fleet with corresponding turbine types based on installed capacity per country. By utilizing estimated production data for 2040, distinct scenarios can be evaluated based on the regulatory strength of the system, inertia estimations and different weather years. The inertia estimation showed a lowered kinetic energy from an average of 223 GWs in 2019 to 175 GWs in 2040. The scenario 2040ref has been developed by the Nordic TSOs as a common reference scenario and is based on estimated production data for 2040. The scenario showed a higher frequency variation outside the normal band 50±0.1 Hz, i.e. a worsened frequency quality. The number of events for the hour evaluated increased from 0.4% to 5.0%, which indicates that the amount of events outside the normal band increases considerably for the lower inertia condition, for the same regulating strength. The weather year sensitivity analysis shows that the inflow of water, weather and temperature during the distinct years significantly influence the estimation, where the number of events varied between 1.1 – 5.0%. From the sensitivity analysis of the regulating strength for the 2040ref scenario it is observed that the relationship between the regulatory strength and the kinetic energy give an acceptable indication of how much regulatory strength is needed to accommodate a decreased inertia in the NPS. However, since the hydro-fleet model encompass the FCR-N, additional work is required to account for instability issues that may arise from a too high regulatory strength and coordination with other frequency reserve products in the Nordic region. The results provide a valuable basis for indicating how the frequency quality and overall kinetic energy in the Nordic region can come to change in the foreseeable future.

Keywords– *Nordic power system, grid inverse, frequency control, scenario 2040, inertia estimation, low inertia power system*

Sammanfattning

De senaste åren har förnyelsebar energiproduktion och integration av intermittenta energikällor ökat i det nordiska elsystemet (NPS) och ersätter de åldrande kärnkraftverken. För att adressera problemet angående en lägre mängd tröghetsmassa i elsystemet föreslår rapporten en elnätsinversmodell av elsystemet med guvernör och anläggningskonfigurationer för olika generationsblandningar i Norden. Syftet med elnätsinversmodellen är att utvärdera hur nettolastvariationerna, och därmed frekvenskvaliteten, påverkas av olika tröghetsestimeringar och väderår för olika scenarier för år 2040. I NPS består frekvensbegränsningsreserven för normal operation till mestadels av vattenkraftverk och modelleras av en hydroflotta med motsvarande turbintyper baserat på installerad kapacitet per land. Genom att använda estimerad produktionsdata för 2040 kan olika scenarier utvärderas utifrån systemets regleringsstyrka, tröghetsestimeringar och olika väderår. Tröghetsuppskattningen visade en minskad kinetisk energi från i genomsnitt 223 GWs 2019 till 175 GWs år 2040. Scenariot 2040ref har utvecklats av de nordiska TSO:erna som ett gemensamt referensscenario och bygger på estimerad produktionsdata för 2040. Scenariot visade en högre frekvensvariation utanför det normala bandet 50$\pm$0.1 Hz, vilket medför en försämrad frekvenskvalitet. Antalet händelser för den utvärderade timmen ökade från 0.4% till 5.0%, vilket indikerar att antalet händelser utanför det normala bandet ökar avsevärt för det lägre tröghetsförhållandet, för samma regleringsstyrka. Väderkänslighetsanalysen visar att inflödet av vatten, väder och temperatur under de olika åren väsentligt påverkar uppskattningen, där antalet händelser varierade mellan 1.1 – 5.0%. Från känslighetsanalysen av reglerstyrkan för 2040ref scenariot observeras att förhållandet mellan reglerstyrkan och den kinetiska energin ger en acceptabel indikation av hur mycket regleringsstyrka som behövs för att tillgodose en minskad tröghet i NPS. Eftersom modellen av hydroflottan omfattar FCR-N krävs dock ytterligare arbete för att ta hänsyn till instabilitetsproblem som kan uppstå genom en alltför hög reglerstyrka och samordning med andra frekvensreservprodukter i Norden. Resultaten ger en värdefull grund för att indikera hur frekvenskvaliteten och den totala kinetiska energin i Norden kan komma att förändras inom överskådlig framtid.

Keywords– *Nordiska elsystemet, elnätsinvers, frekvensstyrning, scenario 2040, tröghetsestimering*

Acknowledgements

My sincere gratitude goes to my supervisor, Mattias Persson, for the many lengthy discussions in the office and at the coffee machine, for always being available, easy-going and considerate in our conversations. I would also like to thank Assoc. Prof. Peiyuan Chen for being my examiner and providing thoughtful and constructive feedback throughout the project.

A big thanks to Robert Eriksson and Niklas Modig at Svenska Kraftnät for our discussions, their inputs and willingness to share and provide the wind power data and relevant reports for the project.

A special thanks goes to Jonas Alterbeck and Kristin Brunge at Svenska Kraftnät for providing the production data for their scenario analysis of 2040.

I would also like to thank the colleagues in the department of Safety and Transport, MTx, at RISE Eklandagatan for the friendly and welcoming work environment.

Finally, I would like to thank my family for their continued support throughout my studies in the highs and lows.

List of Acronyms

DSO	Distribution System Operator
ENTSO-E	European Network of Transmission System Operators for Electricity
FCR-N	Frequency Containment Reserve for Normal operation
FCR-D	Frequency Containment Reserve for Disturbed operation
FFR	Fast Frequency Response
(a)FRR	Automatic Frequency Restoration Reserve
(m)FRR	Manual Frequency Restoration Reserve
GV	Guide Vane
GVO	Guide Vane Opening
HPP	Hydro Power Plant
MoNB	Minutes outside Normal Band
NPS	Nordic Power System
PMU	Phasor Measurement Unit
PoNB	Percent outside Normal Band
RISE	Research Institutes of Sweden
SvK	Svenska Kraftnät
TSO	Transmission System Operator

List of Symbols

Model parameters

Symbol	Description	Unit
α	Angle of the runner blade	$^\circ$
A_{m}	Gain margin	$^\circ$
BL_{α}	Amplitude of backlash runner regulation	%
BL_{Y}	Amplitude of backlash main servo valve	%
BL_{gv}	Amplitude of backlash guide vane stem	%
D	System damping, load frequency dependency	MW/Hz
E_p	Droop, E_{p}-setting for the governor	Hz/%
E	Energy	MWh
f	Grid frequency	Hz
f_0	Grid nominal frequency	Hz
φ_{m}	Phase margin	$^\circ$
H_{r}	Rated head	m
H	Inertia constant	s
K_{p}	Controller proportional gain	-
K_{i}	Controller integral gain	-
M	Inertia constant, $2H$	s
M_{s}	Maximum sensitivity	-
P	Power	MW
P_{L}	Load disturbance	MW
r	Sensitivity margin radius	-
R	System frequency response	%/Hz
R_{Y}	Power alteration servo valve	%/Hz
R_{α}	Power alteration servo runner	%/Hz
s	Laplace operator	-
S	Apparent power	MVA
S_b	System loading and power base	MVA

$S_{n,FCR-N}$	Individual rating of a unit n	MVA
T_α	Servo runner time constant	s
$T_{\mathrm{del,Y}}$	Servo valve time delay	s
$T_{\mathrm{del},\alpha}$	Servo runner time delay	s
T_{i}	Integrator time constant	s
T_{w}	Water time constant	s
T_{y}	Actuator time constant	s
T_{Y}	Servo valve time constant	s
Y	Guide vane opening	%
ω	Angular frequency	rad/s
Y_0	Loading of the unit	%

Note that the units are often presented in per unit values.

Table of Contents

1 Introduction

1.1 Background

Recently, the renewable energy production and integration of intermittent energy sources have increased in the Nordic Power System (NPS) and are replacing the aging nuclear power plants. This has caused concerns regarding the state of the power system inertia, since a change in the generation mix towards more renewable sources precipitate more recurrent frequency contingencies. The Nordic power grid has a nominal frequency of 50 Hz, where the FCR-N control response in the system for frequency dips is of importance for a more variable frequency in the grid, where minor perturbations will firstly appear. When modelling a power system, usually governor systems and plant configurations are utilized combined with a grid model of the system inertia, where net load disturbances can be analyzed. However, another interesting approach is to create a "grid inverse" of the power system where the system input is frequency data that generates a certain net load disturbance. Using this method different frequency, or generation mixes can be analyzed together with an estimation of the system inertia to generate particular types of net load disturbances to view the impact of e.g. different inertia estimations and increased renewable energy integration. For a certain generation mix the influence on the frequency quality for different grid inverse parameters and inertia estimations can be simulated and then compared in a model of the power system.

1.2 Aim

In order to address concerns regarding a lower inertia power system and weakened grid conditions the thesis address knowledge about future frequency contingencies and indicate where problems can arise for a high penetration of intermittent energy sources in the future grid. The main goals are:

- To develop a grid inverse model of the power system and to implement governor and plant configurations for different generation mixes in the Nordic region.
- To perform a sensitivity analysis, to evaluate the model in terms of grid inverse parameters, regulatory strength, stability and robustness.
- To evaluate how the net load disturbances, and thus the frequency quality, is affected by different inertia estimations, weather conditions and seasonal variations for distinct scenarios for the year 2040.

1.3 Scope

The basic outline of this project is to develop a grid inverse model to evaluate the system net load variations caused by different generation mixes. The model will consist of governors and plant models corresponding to the Nordic generation mix on an hourly basis. The output of the grid inverse model will then be run through a regular model of the power system to confirm that the model works. Then different frequency data series with certain generation mix will be run to evaluate how they impact the model output and to view the effect of higher wind power penetration levels. A sensitivity analysis of inertia estimation will be performed and different levels of control responses for FCR-N will be evaluated, along with an investigation of a future scenario or forecast for the year 2040.

1.4 Limitations

Certain breakpoints were introduced in the start of the project. This was done to create a structure and to act as partial milestones and in the case that not all focus areas could be fulfilled, or if some proved unrealistic to continue pursuing. These breakpoints were:

- To acquire a working model of the grid inverse that could function with simple commands, which was considered as bare minimum for the project.
- To evaluate how increased wind power penetration levels impact the model output, how it affect the net load disturbance and thus the frequency quality.
- To perform a sensitivity analysis of the model with regards to the grid inverse parameters and the inertia estimation.
- To see how a variation in the regulatory strength, FCR-N, would impact the model and investigate how a faster control response than FCR-N could impact the model.

Additional limitations are that sufficient simplifications will be utilized for the governor and plant complexity and the generating units will be considered to be lumped together.

1.5 Methodology

The project will mainly be conducted in the following steps:

- Literature review
- Implementation of a grid inverse model
- Implementation of a regular grid model
- Evaluation of wind power penetration levels
- Sensitivity analysis of system parameters and inertia
- Variations in control responses FCR-N

1.5.1 Literature review

In order to provide a broad base of information, a literature review will be conducted on hydro-, thermal-, nuclear power plant governors, wind powers contribution to net load fluctuations, frequency control, filtering techniques, deadband, inertia estimation, Nordic power system inertia and its future forecasts. This was done in order to get more familiar with the different types of plant governor models, common filtering techniques and control responses for the Nordic grid. Further, the NPS inertia was reviewed for an inertia estimation along with future forecasts.

1.5.2 Implementation of a grid inverse model

Before implementing the governor and control systems in a Matlab® Simulink model, different considerations had to be made regarding the elaboration of the governor models, to achieve a suitable level of complexity. After assessment of these elements, a model of the grid inverse was built in Simulink.

1.5.3 Implementation of regular grid model

To verify that the grid inverse functions as intended a regular grid model was implemented in order to validate the inverse model.

1.5.4 Evaluation of wind power penetration levels

After the completion of the grid inverse model different generation mixes was studied to determine what mix predominately introduce higher levels of net load disturbances to the system. The main focus of this was to view and evaluate how higher wind power penetration levels impact the model and to make a correlation between the net load variation, ΔP, the system load level and the wind penetration ratio. Firstly, this was investigated with a series of PMU-data to view the current variation in 2019, how volatile it was to wind power penetration and if a forecast could be made utilizing the model for the year 2040.

1.5.5 Sensitivity analysis of system parameters and inertia

Investigation of how different grid inverse parameter settings impact the system. Also, an evaluation of how the system inertia estimations, H, impact the net load disturbance, ΔP. For example this would be presented as a figure of how the simulated frequency differ from the measured frequency dependant on the kinetic energy of the system.

1.5.6 Variations in control responses FCR-N

Evaluation of how an increased level of FCR-N impact the future frequency quality and if a faster control response could be implemented apart from the FCR-N. This could be implemented by varying the FCR-N reserve for different scenario estimations.

1.6 Sustainable aspects

Regarding the sustainable approach of the work, societal-, ethical and ecological aspects the project infers to facilitate better understanding about how higher levels of wind penetration affect the net load variations. Since a higher level of wind integration is the trend in Sweden it is therefore of interest to further study how a transition into more renewable power integration can impact the frequency in the NPS. This would be in accordance with the sustainable aspects to further information about the shift from the nuclear power plants towards a more green and renewable alternative, while complying with ethical design.

1.7 Previous work

The idea of this thesis work came from a previous study on regulatory strategies for hydro power turbines [1], where a grid inverse model was used to obtain the net load disturbance. The study emphasis guide vane (GV) operation (GVO) in a hydro power plant (HPP) to evaluate how different filtering techniques impact the GVO. The filters investigated were a linear, deadband and floating deadband filter, where the floating deadband had the best performance in general, with an improved frequency quality and not as much GV movement as the other options. The authors further utilized the model in [2], where the concept was developed to investigate wear and tear reduction for hydro power turbines, also emphasizing the frequency quality aspect.

The study address the control aspects of GV movements, with regards to wear and tear reduction, since minor perturbations force the GVs to move more extensively. The article suggest that a floating deadband filter after the GVO controller is more suitable than the commonly used deadband filter. In [3] the distribution of the frequency control reserve for primary and secondary frequency control is considered with regards to volume sold in reserve from a hydro power fleet and how it affect frequency quality, losses in production and wear and tear on the plants. In the paper, Francis and Kaplan turbines are modelled using Virtual Gate Opening (VGO) and then aggregated into a hydro power fleet. The results for low droop of the hydro governor settings were increased load cycles and a poor quality of the FCR due to backlash, while a higher droop incremented the losses of production for primary frequency control. It is also noted that frequency quality is heightened by the automatic secondary response, but the wear and tear is amplified. In [4, 5, 6] control strategies of dynamic Pelton turbines are explored. Reference [4, 5] concern load rejection studies, conservative governor design and discuss improved control design strategies. In [6], parameters extraction of a Pelton turbine is performed using different algorithms based on measurement data.

Regarding inertia estimations for the Nordic region [7] propose an estimation of the kinetic energy in the NPS. The estimation of the NPS inertia constant is made by data from ENTSO-E production data for the year 2015, which is compared to the Nordic Transmission System Operators (TSOs) estimation. Further, a future scenario for higher wind power integration for the year 2025 is explored. The article presents an estimation tool for the NPS kinetic energy for 2015 with a scenario for 2025 and was benchmarked with the TSOs estimation algorithm for the 2015 case with a factor of 0.94 in correlation.

In previous studies [1, 2, 3], the focus of the grid inverse model has been on control strategies to mitigate or relief stress from extensive GV movement and to reduce the wear and tear of HPPs, mainly of the Francis and Kaplan turbine variants. Since most of the frequency regulatory actions for primary frequency control are encompassed by hydro power the approach used in this report is to extend the model to encompass the different hydro turbine types in the NPS, to also cover the Pelton turbine, [4, 5, 6], generation mix and an inertia estimation tool, [7], for investigating future scenarios e.g. the year 2040 and forecasting for lower inertia conditions.

1.8 Thesis structure

The report is divided into several different sections. The introductory chapter lay a foundation for power system modelling and covers system inertia, generator droop settings, frequency control responses and estimations regarding system inertia and future forecasts. Since the FCR-N control response is mainly based on the hydro power fleet in the NPS, basic concepts and terms of hydro units are treated in the second chapter. This is expanded to different hydraulic turbine models, to explain how distinct parts interact in the turbine variants. After the overview of hydro power mechanical parts, control theory is introduced with a simple feedback system that is built up to model different hydro governors and turbines. An one-area model of a hydro power plant is then represented and the final design amalgamates the different parts to a lumped power system model utilizing particular governor and turbine models dependant on the generation mix in the Nordic region. Further, stability and sensitivity analysis is performed and the final chapter discuss different scenarios with lower inertia conditions, based on the inertia estimation tool.

2 Power system model

This report builds on power system analysis and this chapter introduces key concepts in power system modelling and system inertia is discussed with regards to the Nordic region. The NPS consist of Sweden, Norway, Finland and Eastern Denmark, which have different generation mixes and quantities of frequency reserve.

2.1 Power system modelling

The frequency quality of the Nordic system is generally stable, however partly due to inefficiencies in supply and demand balancing there are indications that the frequency quality is slowly deteriorating [8]. When a perturbation is introduced to the power system the kinetic energy changes and the machines in the system either contribute with or consume more energy. By utilizing the swing equation the electrical and mechanical power of a synchronous machine can be modelled as

$$2H\frac{d\omega_r}{dt} = P_m - P_e \tag{2.1}$$

where H is the inertia constant, ω_r is the electrical angular frequency, P_m is the mechanical power and P_e is the electrical power for a base power [9]. Multiple synchronous machines can now be considered as the summation of the previous expression by

$$\sum_n 2H_n\frac{d\omega_{r,n}}{dt} = \sum_n (P_{m,n} - P_{e,n}) \tag{2.2}$$

where sub-index n represents the specific generator. This formulation assumes that there is a system base of S_n and $\frac{d\omega_{r,n}}{dt}$ is the same for all generators. It can be rewritten as (2.1) if H is the inertia for the sum total of the synchronous machines. Thus, from (2.1), using the relationship $M = 2H$ and replacing the derivative term with the Laplace operator the expression can be rewritten as

$$\Delta\omega_r = \frac{\Delta P_m - \Delta P_e}{Ms}. \tag{2.3}$$

The electrical power is dependant on the frequency dependency of the load and the load deviations, therefore the expression can further be expanded by the relation

$$\Delta P_e = \Delta P_L + D\Delta\omega_r, \tag{2.4}$$

where P_L is the load deviation and D is the load frequency dependency. Thus, the final expression of the power system is defined by

$$\Delta\omega_r = \frac{\Delta P_m - \Delta P_L}{Ms + D}, \tag{2.5}$$

which describes a lumped power system model consisting of the connected synchronous generators.

2.1.1 System inertia and droop settings

The expression inertia in the power system refers to the change in rotational speed for the rotating machines in the power system, or the amount of energy required to achieve a change in speed [10]. The trend is that the energy sector is in a state of structural change or reformation. The large synchronous machines are replaced with renewable alternatives such as wind power and the overall rotating mass is lowered, this sets a greater demand for quicker control interactions [10]. The separate inertia constants for the machines in the system is defined by

$$H = \frac{E_k}{S_b}, \tag{2.6}$$

where E_k is the kinetic energy and S_b is the generators rated apparent power. The constant provides information about how long the machine can use its reserved kinetic energy to keep going at rated power. Depending on generation type the inertia constants vary, this is mostly dependant on the speed and weight of the generator. The energy of rotating mass, i.e. the kinetic energy E_k can be represented as

$$E_k = \frac{1}{2}J\omega^2, \tag{2.7}$$

where J is the moment of inertia and ω is the angular speed. The kinetic energy of the power system is influenced by the ratings of the separate generators inertia constants. To share the contribution to the frequency control response many generating units are used to provide the total reserve capacity. This is realized in a hydro power unit by the droop-setting, or

$$\frac{1}{R} = \frac{\Delta f}{\Delta P}, \tag{2.8}$$

where R is the rotor speed adjustment rate, Δf is the frequency deviation from the nominal f_0 and ΔP is the variation in power output. Differences in the units capacity and sizing determine the droop, which is the relation between the frequency and the power output.

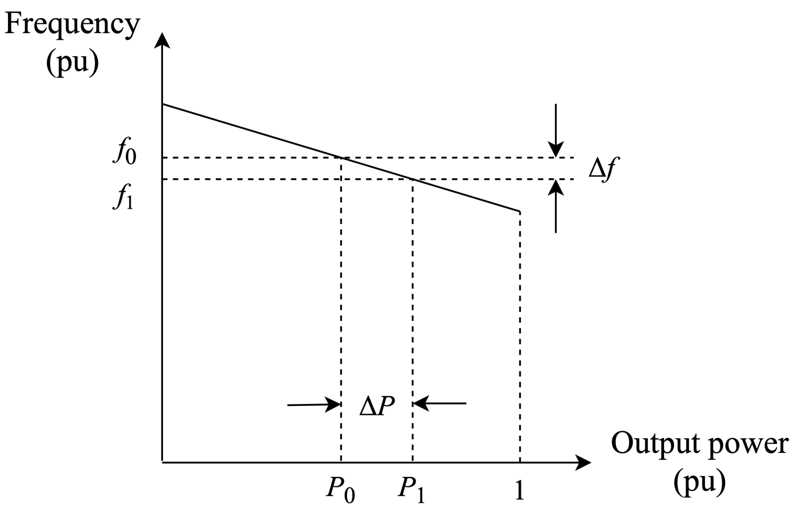

Figure 1: Steady state, or ideal characteristics for droop settings of a governor [11].

To exemplify Figure 1, a 5% droop can be interpreted as a 5% frequency deviation means 100% increase in output power.

2.2 Frequency control in the Nordic region

The objective of power system operation is to keep the system in balance and to meet the active and reactive load demand instantaneously and continuously. The frequency is determined by the balance in active power between the load and the generation and for an acceptable frequency in the grid it should be almost constant. Since the frequency is an all-encompassing aspect of the power system, a change in generation or load is therefore propagated throughout the entire system. To keep the frequency of the overall system within satisfactory operational range different control services are incorporated to fulfill this need.

2.2.1 Primary frequency control

In the NPS the limit for normal operation is 49.9-50.1 Hz, where 50 Hz is the nominal frequency of the system [12]. The Nordic TSOs are responsible for the regulatory actions and frequency control in the power system. In general, the frequency stability in the power system mainly depends on three factors, the total kinetic energy in the grid, the capacity of reserves and the dimensioning fault or incident. When a deviation or fault occurs, there are essentially two levels of control responses in the NPS to counteract or balance it, they are the primary and secondary responses. The primary regulating reserve is characterized by the Frequency Containment Reserves for Normal operation (FCR-N) and for Disturbances (FCR-D), which are mainly incorporated by hydro power plants. They are automatic reserves and initiate when the frequency drops under or goes above $\pm$100 mHz and -500 mHz, respectively [12]. The condition for providing FCR-N is that the corresponding time constant should not exceed 60 s, whereas the proportional gain is required to be at least 2%. Regarding the FCR-D requirement it is stated that 50% of the available capacity shall be utilized within 5 s and fully available at 30 s. In the NPS the regulatory capacity for the FCR-N reserve is 600 MW and for the FCR-D it is enough to cover a N-1 dimensioning fault or incident, often set to 1450 MW [13, 14], which is the power deficit of the nuclear unit *Oskarshamn 3* in Sweden.

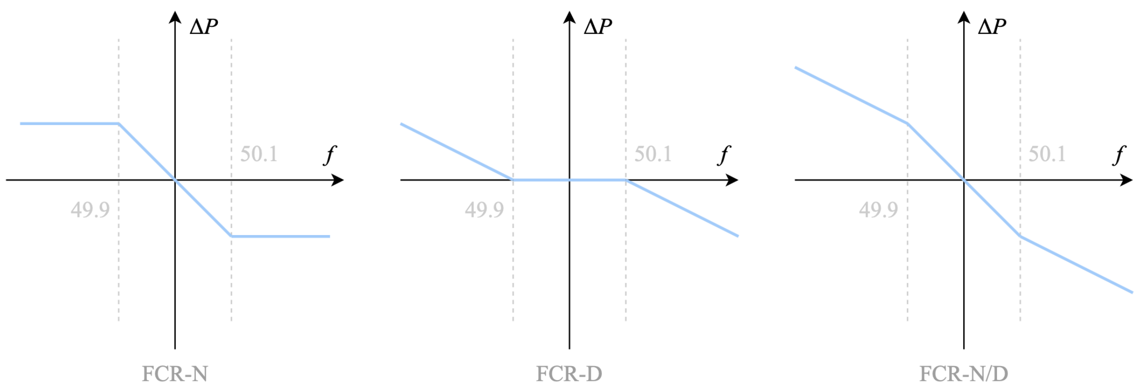

Figure 2: System droop profiles for FCR-N, FCR-D and a joint representation [14].

Figure 2 describes the droop profiles for the FCR-N and FCR-D products. The behavior depicted represent the ideal scenario and in the switch over region from FCR-N to FCR-D there are discrepancies because of the relationship between the settings. For a lower FCR-N droop in relation to the FCR-D settings there will be error in the steady state frequency deviation, while if the FCR-N droop is higher, this can create a state where no equilibrium point is reached for a disturbance in the system [14].

2.2.2 Secondary frequency control

In situations when the power system experience lower inertia conditions the primary control response can prove insufficient to cover the total fault or disturbance to re-balance the system, therefore the secondary response provides additional support. The secondary control response is the automatic frequency restoration reserve (aFRR), which is supplemented by a manual restoration reserve (mFRR). The main purpose of the secondary control action is to restore the primary reserve and the system to the nominal frequency. As compared to the FCR response, the FRR is composed of both thermal and hydro power. Since the secondary control action is much slower then the primary, the primary reserve stabilizes the frequency perturbation and the secondary reserve restores it to the rated value tuning the load reference of the specific units, to later return to normal operation.

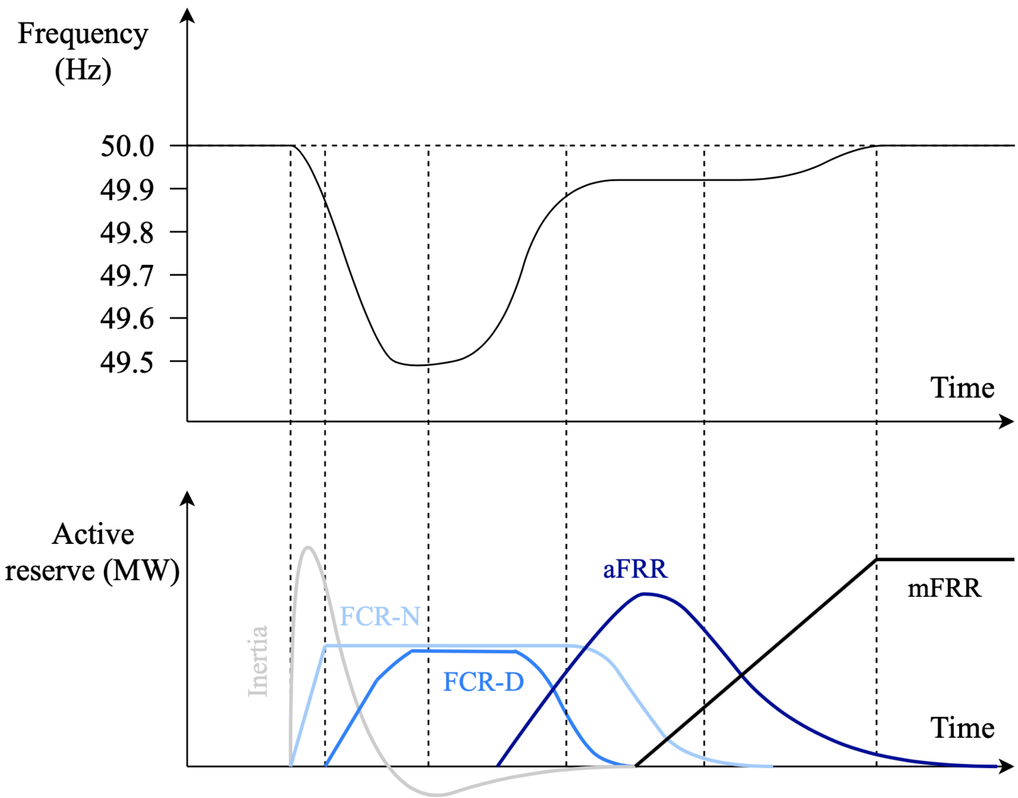

Figure 3: Principles for the frequency regulatory actions in the Nordic power system during a frequency dip for the primary and secondary responses for a fictive frequency dip.

The principle and time intervals for the regulatory actions of the primary and secondary frequency responses are described in Figure 3 for the NPS, along with the initial inertia response of the system.

2.2.3 Generation mix and frequency reserve

Generation mix refers to the amount of different production units in the power system that contributes to the overall energy demand. The generation mix in the NPS mostly consist of hydro, nuclear, thermal and wind power production. In the NPS most of the frequency reserve for primary and secondary control comprise of hydro power units. Therefore it is important to know the split between different turbine types connected to the NPS, since they have different characteristics and governor design. According to [15, 16] there is approximately 45900 MW worth of installed hydro power in the Sweden, Norway and Finland, excluding units below 10 MW capacity, of which are seldom outfitted with droop control [16]. The mix of the turbine types for hydro power production in the NPS are of Francis, Kaplan and Pelton type turbines.

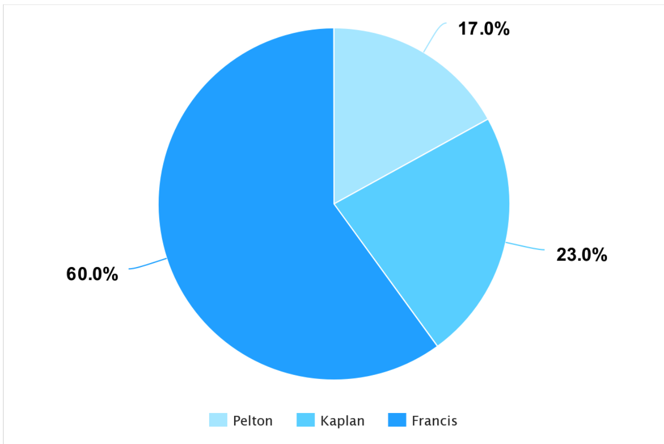

Figure 4: Hydro power turbine split in the Nordic region excluding plants <10MW [16].

The turbine distribution in the Nordic region is illustrated in Figure 4. Here it can be observed that the main contribution is from the Francis type turbine, which is mostly installed in Sweden and Norway for frequency regulation. Kaplan turbines are installed in all three countries and the Pelton turbine is only used in Norway. To further elaborate on the turbines utilized the distribution is differentiated in type per country.

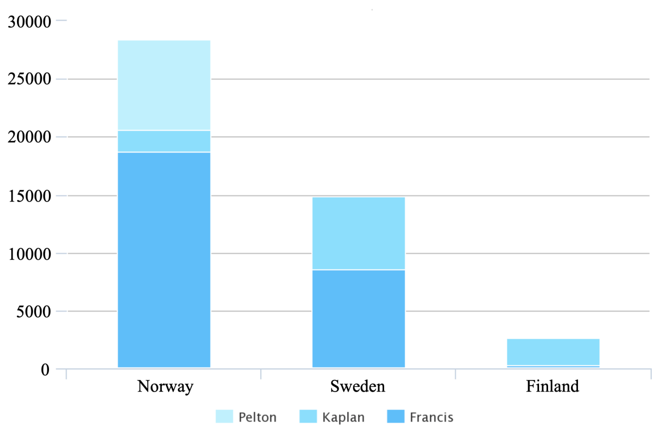

Figure 5: Distribution of installed capacity in MW of Francis, Kaplan and Pelton turbines in the Nordic region excluding plants <10MW [16].

The distribution in MW of the turbine types are presented in Figure 5 for the different countries. From the information about the percentage split of the different turbines utilized in the Nordic region, the unit share of turbines can be calculated assuming that all types of turbines are used for the FCR-N control response. Based on the percentage scaling and the amount of FCR-N in the NPS, an estimation for the rated active power contribution of the distinct turbine types can be attained to scale the hydro models for the different countries.

2.2.4 Minutes outside normal band

In recent years, the overall frequency quality has been on the decline in the Nordic synchronous region [8]. One type of measurement to ensure these variations is Minutes outside Normal Band (MoNB). According to SvK, the normal operating region for the power system should not be breached more than 10000 minutes annually, or 1.9% of the year, i.e. the frequency should not exceed or go below 50±0.1 Hz [17]. The aFRR product was firstly introduced to compensated for this trend, but another feasible option is to revisit the requirement of the FCR-N control reserve currently at 600 MW or introduce new frequency reserve products. The MoNB is defined as following

$$kpi_{MoNB} = \frac{\begin{cases} \int dt, & |\Delta f(t)| > 0.1Hz \\ 0, & |\Delta f(t)| < 0.1Hz \end{cases}}{\int dt}, \tag{2.9}$$

where $f(t)$ is the measurement data and $\int dt$ in the nominator is the amount of time that deviates from the normal operation divided by the whole data set [17]. The term kpi_{MoNB} stand for key performance indicator of the MoNB. Since MoNB is usually utilized in scenarios where yearly data is analyzed, it is therefore more suitable for our purposes to evaluate the percent of minutes outside the normal band hourly. Thus, this will be referred to as Percent outside Normal Band (PoNB) for the analyzed hour.

2.3 Inertia estimation, forecasting and scenarios

While the frequency quality in the Nordic region is almost constant, the trend is towards lower levels of kinetic energy in the grid with the incorporation of intermittent energy sources and thus an overall lowered system inertia [8]. The NPS frequency balance is reliant on the kinetic energy from the rotating mass and is decreased by renewable integration, along with HVDC import. The main influencing factors to keep the frequency in an acceptable frequency band of 49.9-50.1 Hz are the rotating mass, the active power and the dimensioning incident, to avoid under-frequency load-shedding and similarly over-frequency generation shedding.

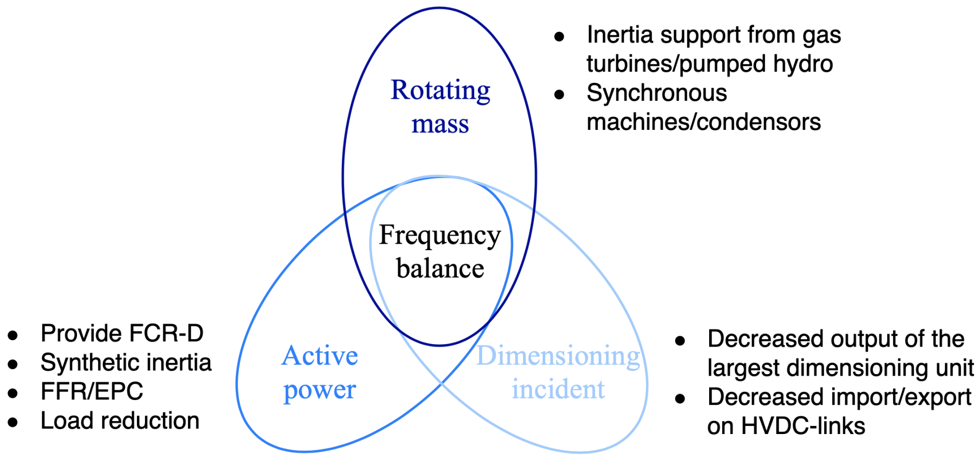

Figure 6: The main functions to support lower inertia conditions and keep the frequency balance of the power system [18].

The main influencing factors to keep the frequency within an acceptable frequency span are depicted in Figure 6. To expand on these three aspects further, in the power system the rotating mass subsist of the grid-connected synchronous machines and condensers. The dimensioning fault, or incident, refers to the loss of the largest production unit available. In more general terms this is referred to as the N-1 fault, which is mostly dependant on the nuclear production facilities. Finally, additional active power can be introduced to the grid to sustain stable grid conditions and restore the frequency, for example by synthetic inertia support, Fast Frequency Response (FFR) and Emergency Power Control (EPC). In this section an inertia estimation tool is examined, along with the balancing issues for wind power integration, scenario data and forecasting for the NPS.

2.3.1 Inertia estimation tool

The Nordic TSOs utilize the Supervisory Control and Data Acquisition (SCADA) system to collect information from the grid and to estimate the power system inertia. In more detail, the system can distinguish whether breaker positions of the generator are switched on to the grid, the generators inertia constant and the apparent power produced [7, 19]. In order to estimate the NPS inertia the inertia constants of different generation types have to be assumed or estimated.

Table 1: NPS assumed inertia constants for different generation types [7].

	SE	NO	FI	DK2
H_{Hydro}	4.5	2.9	2.8	-
$H_{Nuclear}$	6.2	-	6.6	-
$H_{Thermal}$	2.9	2.5	4.4	4.5

The inertia constants for the NPS are presented in Table 1 and the values are from the ENTSO-E transparency platform [20]. Using the inertia constants under the assumptions of [7], the power system inertia can be estimated to

$$H_{sys} = \frac{\frac{P_{H-se}H_{H-se}}{0.8\cos\phi_H} + \frac{P_{H-no}H_{H-no}}{0.8\cos\phi_H} + \frac{P_{H-fi}H_{H-fi}}{0.8\cos\phi_H} + \frac{P_{N-se}H_{N-se}}{\cos\phi_N}\cdots}{\frac{P_{H-se}}{0.8\cos\phi_H} + \frac{P_{H-no}}{0.8\cos\phi_H} + \frac{P_{H-fi}}{0.8\cos\phi_H} + \frac{P_{N-se}}{\cos\phi_N}\cdots} \tag{2.10}$$

for the NPS, where $H_{type-country}$ is the country-specific inertia constant averaged out and $P_{type-country}$ is the generation type of the energy production [7]. It is assumed that all generating units have a power factor of 0.9 apart from wind and solar, which have unity power factor represented by $\cos(\phi_{Unit})$. The HPPs are all assumed to be operating at 0.8 of the rated power of the unit. The kinetic energy of the NPS can then be estimated by multiplying the system inertia constant $H_{sys-nordic}$ with the system base.

Table 2: Expected generation capacity for wind and nuclear power in the NPS in 2025 compared to 2015 [7]. The values for 2025 scenario is marked in bold characters.

Installed capacity	SE	NO	FI	DK2	Unit
Wind	**10500**/5420	**3207**/873	**3900**/1005	**2606**/1036	MW
Nuclear	**6700**/9528	-	**5549**/2749	-	MW

A future scenario of installed generation capacity for the Nordic region in the year 2025 is presented in Table 2, accounting for the development of nuclear projects in the Nordic region and assuming the wind power integration persists as current trends indicate. The system inertia can then be estimated for the year 2040 using the same approach as mentioned above. The contribution from the installed nuclear power generation counterbalance and weighs up for the wind power integration, although it has a negative impact on the overall inertia.

2.3.2 Wind power integration and balancing

The increasing interest of intermittent energy sources on the commercial power market is a positive trend concerning CO_2-emission levels and renewable integration, but it comes with its own share of issues. A crucial aspect in the market deregulation and re-structuring is balancing and to address the uncertainties that renewables entails. Generally when talking about balancing, the time-period concerned is of interest, since it encompass both annual shifts, like seasonal variations, down to the hourly regulatory level. In the Nordic region the trend is towards an increase in wind power generation and decommissioning of older production units, therefore the system will be more interdependent on meteorological data, which increase the need for estimations and proactive resources to account for the irregularities of wind power generation. A feasible option is to provide additional services from the wind farms for synthetic inertia support, i.e. Fast Frequency Response (FFR). The FFR would start to contribute before the FCR in a matter of seconds, to lower the initial frequency dip which would be beneficial for a more volatile grid condition.

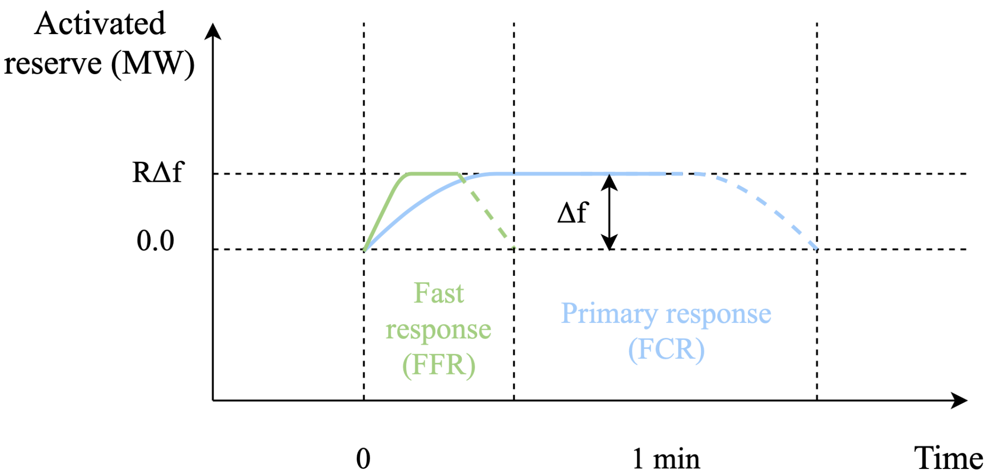

Figure 7: Frequency regulatory actions during a frequency dip for the primary response with the fast frequency response product introduced to the system [14].

The FFR concept is presented in Figure 7, recalling the system response to a larger frequency deviation from Figure 3. To take advantage of the installed wind power capacity, different methods for wind power responses for reserve interactions include pitch control, derated operation, synthetic inertia support, DC-link applications and load voltage control [19]. Other workable solutions not relying solely on wind power plants include demand response, vehicle-to-grid solutions, pumped hydro power plants, flywheels and battery storage facilities.

2.3.3 Future scenarios in the Nordic region, ENTSO-E

Predictions and future scenario data are crucial when trying to anticipate or evaluate future trends or conditions. In Europe, ENTSO-E is an association of the European TSOs to promote closer association and cooperation within the EU with regards to energy and climate policies. In 2018 ENTSO-E released their TYNDP2018 report, which is a network developmental plan and describes different scenarios for the energy sector for 2040.

Table 3: Installed capacity of different energy sources for Sweden, for distinct scenarios ranging from 2020-2040 [21].

Production type (MW)	2020	ST2040	DG2040	GCA2040
Hydro	16300	16300	16300	16300
Nuclear	8600	3500	3500	3500
Wind	7500	16000	15000	19000
Solar	500	2250	12000	7000
Thermal and other	5900	4000	4000	4000
Total	38800	42050	50800	49800

Data from ENTSO-E have been compiled in Table 3 for Sweden for different scenarios ranging from a conservative case to of a more radical climate action case with elevated levels of renewable energy present in the power system [22]. In Appendix A Tables 20-22 the installed capacity are presented for Finland, Norway and Denmark respectively, encompassing the Nordic region. The different scenarios are presented in bar diagrams in [23] for a better visualization. The different abbreviations stand for Sustainable Transition (ST), Distributed Generation (DG) and Global Climate Action (GCA) [22, 21]. ST is focused on a stable decline in the fossil fuel plants currently installed to reduce CO_2-emission levels and assumes a steady but slower pace in the structural changes in the energy sector. DG is more concerned with a scenario emphasizing prosumers, thus relying heavily on decentralization and end-user interactions, e.g. smart houses, high vehicle-to-grid integration, solar PV solutions, etc. GCA is the most drastic scenario, with significant decarbonisation efforts, electric vehicle dominance in the transport sector and an overall high efficiency for renewable alternatives.

2.3.4 Future scenarios in the Nordic region, SvK

The Swedish TSO Svenska Kraftnät (SvK) updates their long-term scenario predictions every other year for the Scandinavian and northern European power system [24]. The scenario project is called LMA2018, with stand for long-term market analysis, where three distinct scenarios are considered based on one reference scenario. The scenario 2040ref has been developed by the Nordic TSOs as a common reference scenario of the current expansion in the energy sector. The development of scenario data is part of the project Nordic Grid Development Plan, where all the Nordic TSOs are involved [24]. From the reference a high and low scenario have been composed by varying the electricity consumption, emission levels and fuel prices, for a more conservative and radical climate action scenario supporting the reference. The scenarios are called 2040ref, for the reference scenario, 2040high and 2040low for the higher and lower estimations, respectively. The electricity production and consumption is reliant on annual variations and weather conditions in the NPS. The scenarios are therefore based on historical weather conditions such as temperature, inflow of water, wind and solar conditions for 31 weather years which are split between the different countries and zones.

Table 4: Installed capacity in Sweden per production type [24].

Production type (MW)	2018/2019	2040low	2040ref	2040high
Hydro	16300	16300	16300	16300
Nuclear	8590	0	0	0
Wind	7150	25920	24730	31710
Solar	460	4010	7380	7380
Thermal and other	5880	4450	4450	4910
Total	32860	50680	52860	60300

The installed capacity is presented in Table 4 in Sweden for 2018/2019 and the different scenario estimates. The production data used for the different scenarios 2040ref, 2040high and 2040low will be used to estimate the system inertia M and the load frequency dependency, D, to evaluate how the simulated frequency behave during a more volatile power system than in 2018/2019. In LMA2018 the total installed capacity for the Nordic region is also estimated, here an assumption is made that the wind and solar power will be increased while the nuclear and thermal power plants are successively decommissioned. As previously mentioned, the Finnish nuclear expansion project involving the reactors *Olkiluoto 3* and *Hanikivi* are considered along with an expansion of hydro power in Norway.

Table 5: Installed capacity in the Nordic region per production type for Sweden, Norway, Finland and Denmark [24].

Production type (GW)	2020	2040low	2040ref	2040high
Hydro	51.9	53.8	53.8	53.8
Nuclear	7.7	2.8	2.8	2.8
Wind	23.8	54.6	54.3	69.3
Solar	1.6	8.4	17.6	17.6
Thermal and other	18.4	13.5	13.5	14.4
Total	103.4	133.1	142	157.9

The estimated installed capacity for the Nordic region is presented in Table 5, in order to characterize the different countries and zones installed capacity for 2040.

3 Hydraulic governor and plant models

Hydro power is a mature and well-established source of renewable energy production and is an inherent part of a sustainable power system. Since hydro power is an old technology it is often considered that the innovation in the area has stagnated, or plateaued. On the contrary, many niche research projects seek to fine-tune or optimize hydro power plants to decrease operational costs and improve the efficiency of the generation. Due to the transition to a more deregulated power market, small increments in e.g. wear and tear on HPPs, frequency reserve product balancing and efficient control strategies can be the distinction between earnings or increased costs. The main impediment to these developments are the demands of dependability and safety on the source of production to secure the supply and demand, since the Nordic region relies heavily on hydro power for much of its bulk energy production. In this chapter physical descriptions of the turbines used in the Nordic region are presented and described to formulate representations suitable for dynamic studies using mathematical models, feedback systems and illustrations.

3.1 General aspects and terminology

Hydro power plants are highly conditional, since they are very dependant on the specific site they are constructed. The location usually determines what type of plant can be built, the power generation capacities and which type of turbine variant that is suitable.

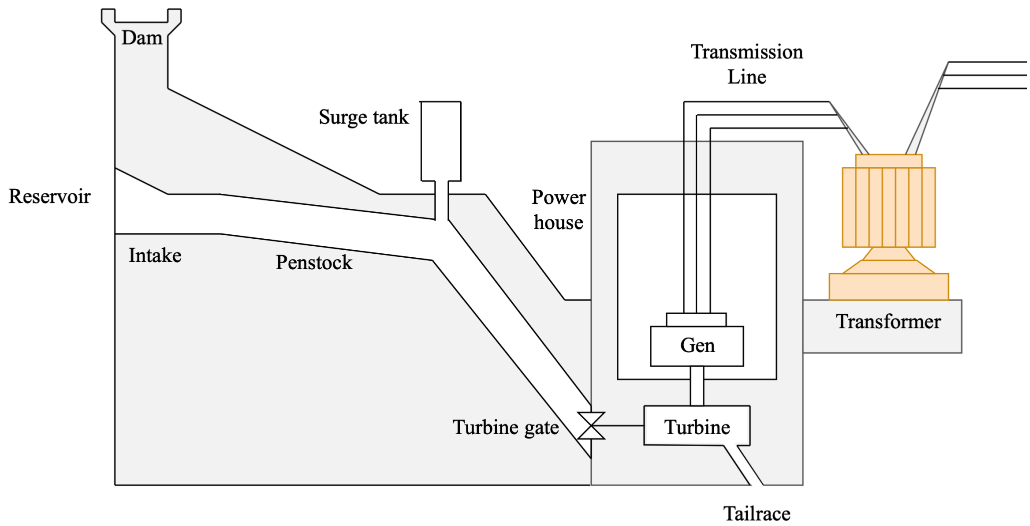

Figure 8: A general overview of a hydraulic power plant with reservoir, intake, penstock, surge chamber, turbine, generator and tailrace.

The main characteristic features of a hydro power plant is described in Figure 8. The reservoir with water upstream is connected to the turbine through the tunnel with a surge tank and the penstock, the water is then let out in the tailrace downstream. The difference between the elevation levels between the reservoir and the tailbay is called the head, which is split into three categories, high-, medium- and low-head hydro power plants. The produced mechanical power in MW from the turbine is represented by

$$P = \rho g Q H_r \eta, \tag{3.1}$$

where ρ is the water density in kg/m^2, g the gravitational acceleration, Q the water flow rate in m^3/s, H_r the effective head in m and η the efficiency of the generator. The efficiency of a particular plant is mainly dependant on the specific turbine features and flow rate, it denotes how effectively the potential energy is utilized from the reservoir.

3.2 Hydraulic turbines

There are many types and categories of turbines in hydro power applications, but they are usually classified in two general types; reactionary and impulse turbines. In the case of reactionary turbines, the water flow encompass the girth of the runner from a spiral or scroll curve casing and run through the guide vanes. Two of the most commonly used variants are the Francis and Kaplan type turbines. The Francis turbine has a high- to medium head and is an example of a radial-flow turbine, where the water flow is mainly pushed in one direction. The incoming water flow from the penstock is fed into the rotator at a specific radius then escapes the turbine at another. The Francis turbine can typically generate an output power from 1 kW to 1000 MW and can be designed for many types of flows, while having a high efficiency and is therefore extensively used [25]. Kaplan turbines are of low- to medium head and are instead of axial-flow type, whereas the water flow is in parallel to the rotational axis of the turbine. Kaplan is an innovation of the Francis turbine and is better suited to low-head application and higher flows. The output power of Kaplan turbine typically range between 1 kW to 150 MW [25].

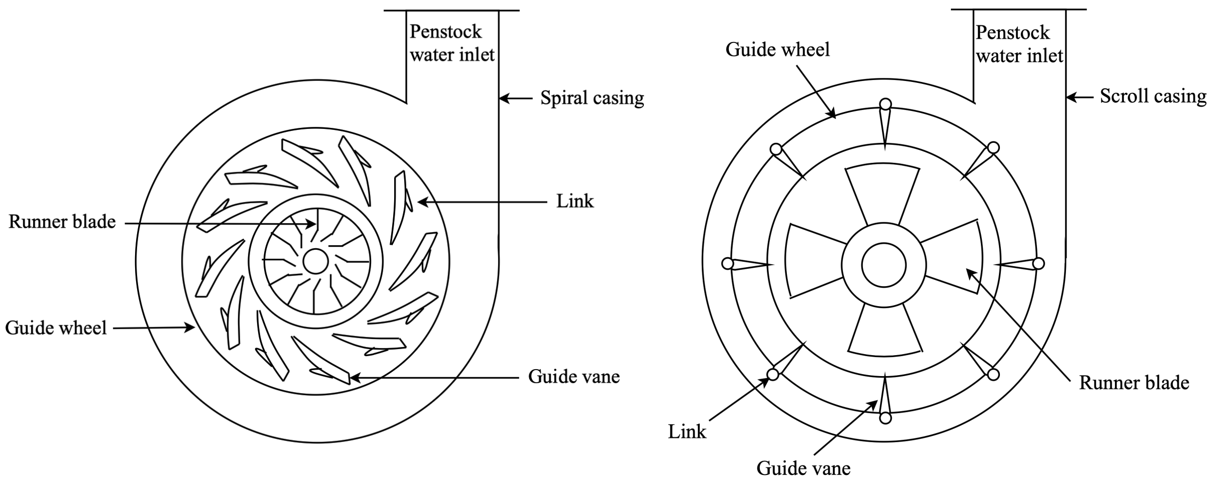

(a) Francis turbine crossection (b) Kaplan turbine crossection

Figure 9: Schematic overview of Francis and Kaplan reactionary turbines [26].

A schematic overview of the reactionary turbines utilized in the NPS can be observed in Figure 9, the Francis variant in Figure 9a) and Kaplan in 9b). As observed in Figure 9, the turbines utilize similar regulatory elements. The main distinguishing factor is that the Kaplan model has an additional control element composed of a runner servomotor. The Francis model rely on solely controlling the guide vane (GV), while the Kaplan model configuration attempt to achieve an optimized behavior by balancing the runner servomotor and the GV.

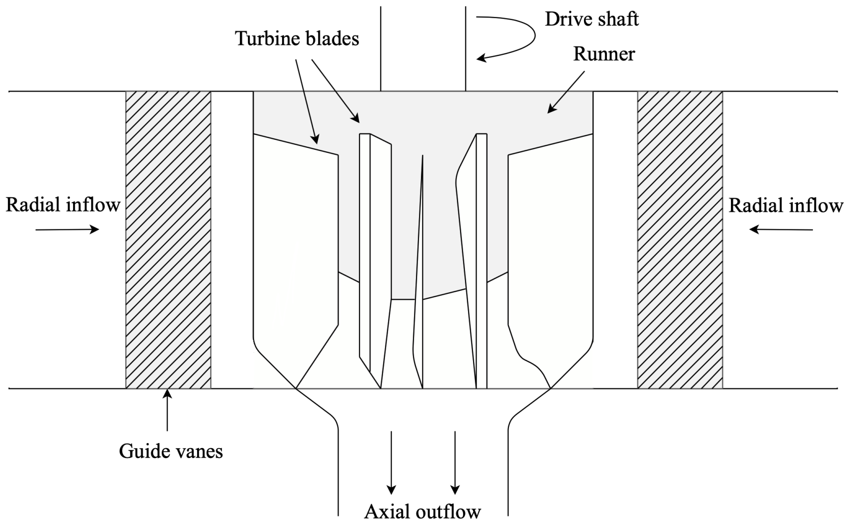

Figure 10: A simplified Francis turbine runner in cross-section [27].

A cross-section of a Francis runner is illustrated in Figure 10 to better present the water intake, shaft interactions and the draft tube, where the water flows downstream through the tailrace to the tailbay. The incoming water flows through the spiral or scroll outer casing enclosing the runner, which shrink in size the further down the turbine it goes, to ensure that the velocity of the water is constant. The water enters the runner mechanism through the guide vanes that direct the water flow, they change in conformity and is necessary to control the generated power of the turbine. The last turbine used in the NPS is the Pelton turbine of the impulse turbine type, a vertical multi-nozzle variant with multiple water jets. It usually has a higher head than the reactionary turbines and is only used in Norway of the Nordic countries.

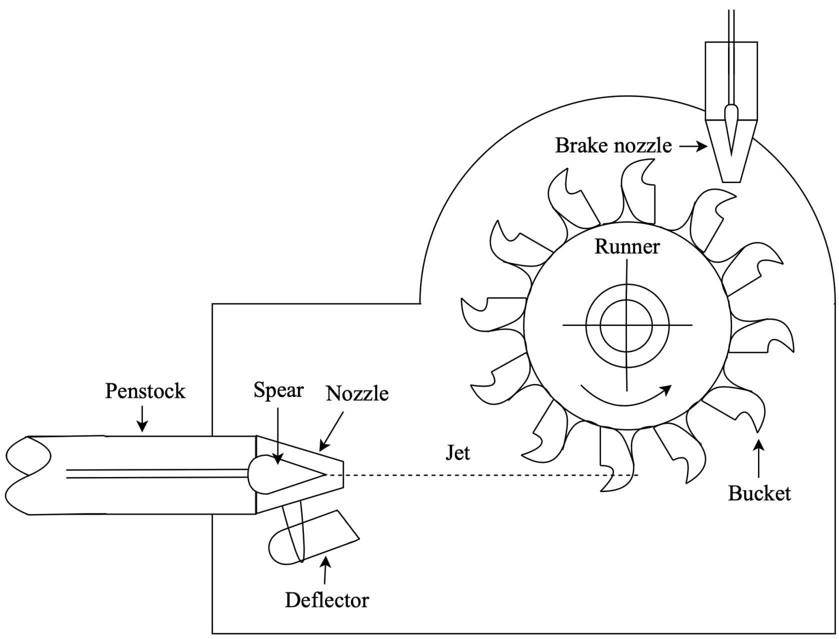

Figure 11: Pelton turbine with water jet, deflector and brake nozzle visualized [26].

An overview of the Pelton turbine is described in Figure 11. The nozzle converts the pressurized energy to a high velocity jet, to control the amount of water discharged a spear is utilized as a regulating mechanism. For larger Pelton variants a brake nozzle is also installed in order to stop the turbine to a halt if needed. The deflector is either mounted on top of the nozzle or as presented in the Figure 11. The deflector is used to cut off a part of the water jet to reduce the influx of water.

3.3 Feedback systems

In this section a general formulation and theoretical background for control systems are provided, which includes performance and stability criterion and concepts for general control system layouts. This is to transition more smoothly into the following sections where the different types of governor configurations are presented. In general, there are always non-linear elements in every type of system but linear control design is commonly used and the non-linear components can be modelled in the form of a backlash to later confirm and verify the linear model.

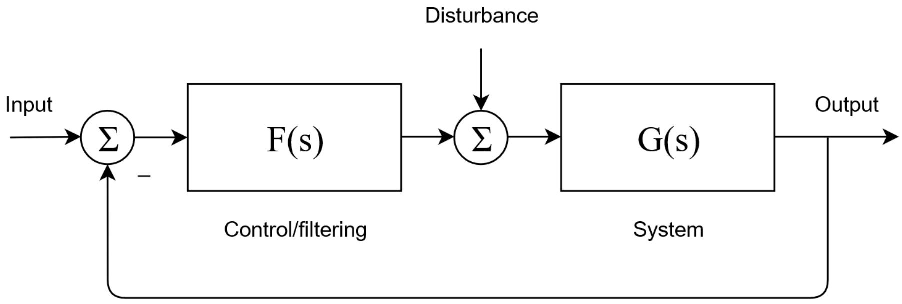

Figure 12: A simple feedback system consisting of a control unit, $F(s)$ and a system $G(s)$ with an introduced disturbance.

For a general closed-loop system as illustrated in Figure 12, the system is modelled by $F(s)$, the control unit and $G(s)$ which is the system model with a disturbance introduced [28]. The method of loop analysis can be utilized to establish system stability for the model, it uses a sinusoidal signal through the system to evaluate if the signal increases or decreases. The method apply the Nyquist criterion to create the transfer function of the loop, where the sensitivity of the system can be described as

$$S(s) = \frac{1}{1 + G_0(s)}, \quad G_0(s) = F(s)G(s) = RF_0(s)G(s) \tag{3.2}$$

where $G_0(s)$ is the loop gain of the system [28]. The parameter R represents the regulating strength and $F_0(s)$ is the normalized unit response of the system. If the frequency dependency of the load is neglected from (2.5) the loop gain can be rewritten as

$$G_0(s) = \frac{R}{E_k}\left[\frac{F_0(s)}{2s/S_b}\right], \tag{3.3}$$

where the relation between the regulating strength R in MW/Hz and the kinetic energy of the grid E_k in GWs can be visualized. Regarding closed-loop stability, if the regulating strength balance out the change in kinetic energy stability is ensured [14]. An example of this is the current conditions compared to a future grid with lower kinetic energy

$$\frac{R}{E_k} = \frac{6000}{120} = \frac{4500}{90},$$

where it can be seen that the regulating strength should be lowered to accommodate a lower inertia system, in this case 90 GWs, to keep the system at the present condition [14]. Therefore it is not clear-cut that an increase in the regulatory strength is beneficial and it has to be adjusted accordingly to the power systems kinetic energy, not to cause concerns regarding instability issues for a fixed hourly regulating strength.

The stability of the system can in turn be determined by the term in the denominator, from (3.2). According to Nyquist, the system is stable if the curve does not enclose -1. The robustness and the stability of the system is described by the phase margin φ_m and gain margin A_m, both in degrees. The gain margin of a system is the gain from the crossover frequency to the instability point, i.e. where the Nyquist curve intersect the real axis to the point $-1 + j0$. The phase margin is defined as the angle for where the gain of the crossover line has to be rotated from the origin to pass through the instability point.

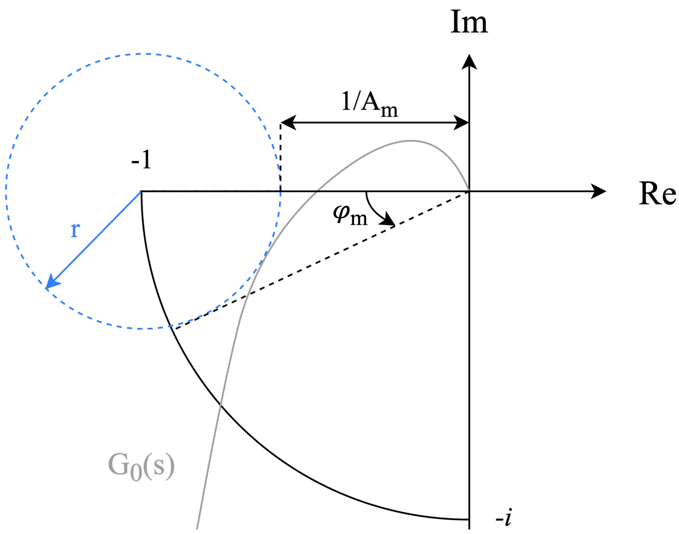

Figure 13: Nyquist stability criterion with phase margin and gain margin quantified [17, 28]

As can be seen in Figure 13 the gain margin can be expressed as

$$A_m \geq \frac{1}{1-r} \tag{3.4}$$

and the phase margin is described as

$$\varphi_m \geq 2 \arcsin{(\frac{r}{2})}. \tag{3.5}$$

The stability margin of the system can then be expressed by

$$|S(s)| \leq M_s = \frac{1}{r}, \tag{3.6}$$

which is the sensitivity function of the system, in this case M_s represents the maximum sensitivity [28], which represent the highest, or worst disturbance amplification.

Further information regarding system stability and feedback systems can be found in [28] pages 95-115. If a disturbance is introduced to the system the transfer function can be described as

$$\frac{G(s)}{1+G_0(s)} \cdot d = S(s)G(s) = \Delta f, \tag{3.7}$$

where the output is Δf. The sensitivity $S(s)$ is therefore not only an important aspect of the stability of the system, but also describes how a the system responds to a disruption.

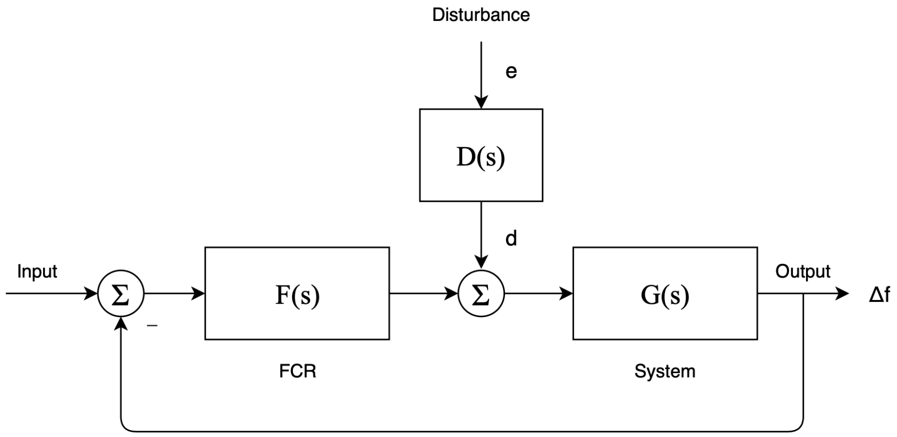

Figure 14: A feedback system with an introduced disturbance signal.

Figure 14 describes a feedback system where a disturbance d is introduced. Since multiple suppliers assist in the control of the FCR-N response it can be represented by multiple FCR-units or $F(s)$, however this does not necessarily mean that all vectors of the different suppliers are in alignment but the sum of them represent the total control response. Therefore an assumption has to be made that the response is consistent across the system.

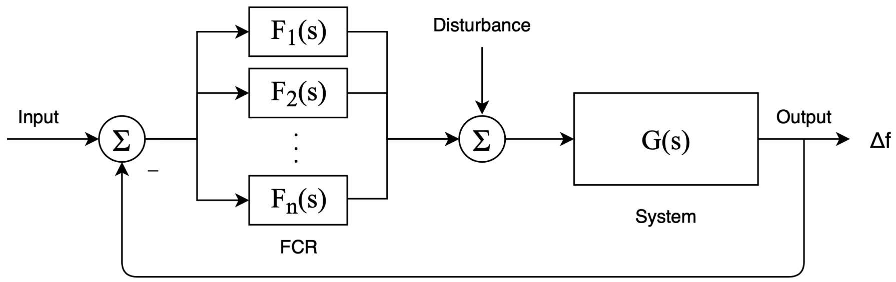

Figure 15: A feedback system with multiple $F(s)$, i.e. many FCR-N suppliers.

A feedback system where multiple FCR-units are utilized is depicted in Figure 15, such that multiple turbine variants can be represented.

3.4 Governor performance and tuning

Regarding the tuning and adjustment of controller settings there may be misconceptions that the hydro power plant parameters are largely static and unchanging. However, in the NPS it is commonplace that the production facilities accommodating primary frequency control are able to regulate their droop-settings, provided that the plant is not of an older model. Since the NPS is mostly dependant on the hydro units, it is a current research area; tuning, optimization of control parameters for plants providing FCR regulatory actions as well as robustness and performance requirements. The hydro governor model is a feedback system that can vary the output of the power and speed to regulate a turbine. From a reference setpoint, the hydro model gain a unit speed feedback to produce a speed regulation for the grid-connected unit. Depending on the application and research topic the detail of the plant differs in terms of complexity, non-linearities and feedback functions in the system. For load rejection studies a non-linear turbine equation and an elastic penstock is necessary, also the surge tank and a split waterway configuration may have to be taken into account [29]. For this study, concerning modelling of a dynamic system where disturbances are in the range of ±0.1 Hz a linear model of the turbine and penstock is often suitable [16, 29, 30].

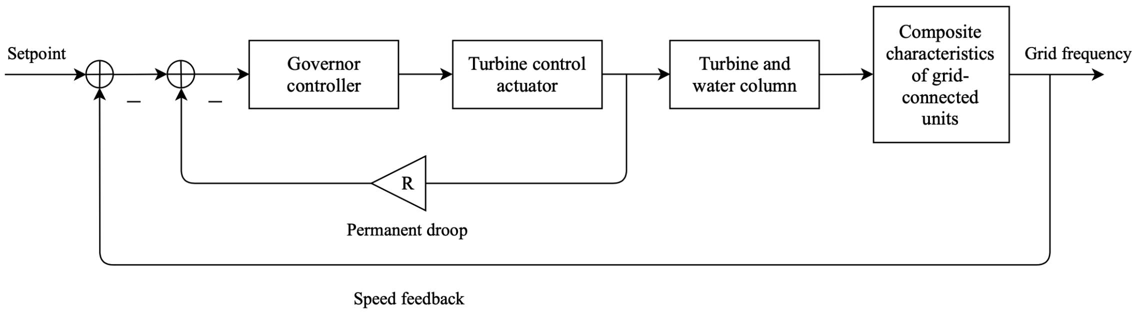

Figure 16: Governor control system of a hydro unit with feedback showcasing the key elements, controller, actuator and waterways [25].

A general model of a grid-connected hydro system is presented in Figure 16 where the controller, actuator, turbine, waterways and the feedback loops are described. The guide vane operation of the Francis and Kaplan turbines can be seen in Figure 9, where the governor controller determine the behavior of the GVs. The turbine, water column and penstock is illustrated in Figure 8. For our purpose, the generating units will be considered as lumped together behaving as described in (2.5).

3.4.1 PI-control in hydro power applications

For primary and secondary control interactions in the power system PI-controllers are generally used. Governor settings and parameter tuning for hydro power plants is a continuous field of research, also including H_∞-controller applications. H_∞-control synthesize is utilized to guarantee a stable and robust system and disturbance rejection, however it is somewhat limited to analyzing distinct cases and is usually of a very high order, which lead to heavy control work [31]. The governors in modern hydro plants are often electric governors and are commonly modelled by a PI-controller with droop R according to

$$\frac{\Delta Y}{\Delta f} = \frac{1}{R}\left[\frac{K_p s + K_i}{(K_p + 1/R)s + K_i}\right], \tag{3.8}$$

where K_p, K_i are the proportional and integral gains, respectively. The output ΔY represents the variation in the gate opening and Δf is the frequency variation, both in per unit. The expression can be formulated in a more compact way, then the representation is

$$\frac{\Delta Y}{\Delta f} = \frac{1}{R}\left[\frac{1+T_1 s}{1+T_2 s}\right], \tag{3.9}$$

where

$$T_1 = \frac{K_p}{K_i}, \quad T_2 = \frac{1+K_p R}{K_i R}. \tag{3.10}$$

The expression can also be visualized in a block diagram, where it is represented by a feedback control loop with Δf as input and ΔY as output.

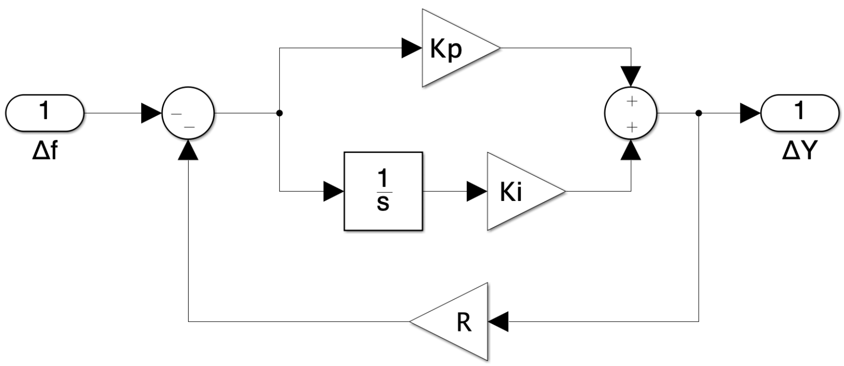

Figure 17: Governor control system of a hydro unit with feedback showcasing a PI controller and the permanent droop.

A conventional governor model with PI control along with the permanent droop settings is depicted in Figure 17. PI is more commonly used as compared to the PID controller, the derivative part of the expression is seldom used for modelling hydro power governors for grid-connection, since a high gain generates oscillations that can move the system towards instability. However, as noted for island operation it can be advantageous to include it [16, 32].

3.4.2 Turbine and penstock modelling

To model the turbine and penstock the subsequent two definitions are introduced [33], where the parameters are in per unit;

$$q = a_{11}h + a_{12}n + a_{13}z \tag{3.11}$$

$$m = a_{21}h + a_{22}n + a_{23}z. \tag{3.12}$$

Here, q is the flow rate and m is the torque of the turbine. The head is represented by h, q is the flow rate, z is the gate position for the turbine and a_{ij} are partial derivatives describing the system, which vary based on the initial conditions. The water time constant is equal to

$$T_w = \frac{\sum lv}{gH_r}, \tag{3.13}$$

where $\sum lv$ is the speed and length of the different segments where the water flows through from the intake, g the gravitational acceleration and H_r is the rated head. In physical terms, the water time constant is the time it takes for the water in the penstock to reach velocity v, from standstill. The rated flow variation is

$$Dq = \frac{-h}{T_w}, \tag{3.14}$$

where D is the differential operator and

$$h = \frac{-a_{12}T_wDn - a_{13}T_wDz}{1 + a_{11}T_wD}. \tag{3.15}$$

Thus, from (3.12) we get

$$m = \frac{[(a_{11}a_{22} - a_{12}a_{21})T_wD + a_{22}]}{1 + a_{11}T_wD}n + \frac{[(a_{11}a_{23} - a_{13}a_{21})T_wD + a_{23}]}{1 + a_{11}T_wD}z. \tag{3.16}$$

An approximate characterization of the expression can be done by disregarding the term with n, the speed of the turbine, under the assumption that there will be very minor speed deviations for a grid-connected hydro power unit [34]. The transfer function representing the turbine and penstock can then be expressed as

$$\frac{m}{z} = \frac{[(a_{11}a_{23} - a_{13}a_{21})T_wD + a_{23}]}{1 + a_{11}T_wD}. \tag{3.17}$$

Table 6: Turbine and penstock transfer function partial derivatives [34].

PD	Full load	Ideal	Description
a_{11}	0.58	$0.5Y_0$	PD of the turbine flow rate with regard to the head
a_{13}	1.1	1	PD of the turbine flow rate with regard to the gate position
a_{21}	1.4	$1.5Y_0$	PD of the turbine torque with regard to the head
a_{23}	1.5	1	PD of the turbine torque with regard to the gate position

The partial derivatives of the terms in the transfer function are described in Table 6. By inserting the ideal values for the turbine and penstock we get

$$\frac{m}{z} = \frac{-T_wY_0s + 1}{0.5T_wY_0s + 1}, \tag{3.18}$$

which is the commonly used representation, where Y_0 is the loading of the turbine. In this report the term Y_0 is assumed to be 0.8, to keep in line with the previous assumption in the inertia estimation and forecast.

3.4.3 Droop and E_p-settings

Vattenfall is one of the largest Distribution System Operators (DSOs) in Sweden and is responsible for the majority of Swedens hydro power facilities. The governor in many of Vattenfalls plants is usually a PI controller with a certain droop setting [29]. Regarding the droop-settings of the hydro governors, Vattenfall has different so called E_p-settings for their governors characterized by the regulating strength R of the unit in %/Hz.

Table 7: E_p-settings for the droop in Vattenfalls hydro plants [2, 29, 35].

E_p-value	R [%/Hz]	Droop, E_p [pu/pu]
E_{p0}	20	0.10
E_{p1}	50	0.04
E_{p2}	100	0.02
E_{p3}	200	0.01

The different E_p-settings are described in Table 7, where the regulating strength and the E_p-setting relation can be expressed by

$$E_p = \frac{1}{R}\left[\frac{Hz}{\%}\right] \cdot \frac{100}{50}\left[\frac{\%}{Hz}\right]. \tag{3.19}$$

For each droop setting, there is a corresponding value for the proportional gain K_p and the integral gain, K_i. The integral gain can also be refereed to as T_i, the integrator time constant.

Table 8: K_p, K_i and T_i values related to a specific droop-setting [2, 29].

	E_{p0}	E_{p1}	E_{p2}	E_{p3}
E_p	0.1	0.04	0.02	0.01
K_p	1	1	1	2
K_i	1/6	5/12	5/6	5/3
T_i	6	2.4	1.2	1.2

The values corresponding the the different droop-settings are presented in Table 8. Swedish hydro governors are commonly based on ASEA/ABB HYC, while Norway have the Hymatek Hyx governor type [16]. The transfer function for the Swedish governor HYC can be expressed by

$$H_{SE}(s) = \frac{\Delta P}{\Delta f} = \frac{K_p s + K_i}{s + [E_p(K_p s + K_i)]} \frac{1 + K_d s}{1 + T_f s} \frac{1}{1 + T_y s} \frac{-T_w Y_0 s + 1}{0.5 T_w Y_0 s + 1} \tag{3.20}$$

and the Norwegian governor Hyx is expressed by

$$H_{NO}(s) = \frac{\Delta P}{\Delta f} = \frac{1}{E_p}\left(\frac{1 + T_i s}{1 + \frac{1}{E_p K_P} T_i s}\right) \frac{1 + T_d s}{1 + T_f s} \frac{1}{1 + T_y s} \frac{-T_w Y_0 s + 1}{0.5 T_w Y_0 s + 1}. \tag{3.21}$$

Here, the different parts of the hydro unit can be distinguished; PI-controller with permanent droop, actuator along with the turbine and penstock. As previously mentioned, the derivative gain K_d for hydro power units is usually set to zero so the expressions can be further simplified. By disregarding the derivative gains the expression for the Swedish HYC governor becomes

$$H_{SE}(s) = \frac{\Delta P}{\Delta f} = \frac{K_p s + K_i}{s + [E_p(K_p s + K_i)]} \frac{1}{1 + T_y s} \frac{-T_w Y_0 s + 1}{0.5 T_w Y_0 s + 1} \tag{3.22}$$

and the Norwegian governor Hyx is expressed by

$$H_{NO}(s) = \frac{\Delta P}{\Delta f} = \frac{1}{E_p}\left(\frac{1 + T_i s}{1 + \frac{1}{E_p K_P} T_i s}\right) \frac{1}{1 + T_y s} \frac{-T_w Y_0 s + 1}{0.5 T_w Y_0 s + 1}. \tag{3.23}$$

3.5 Hydro one-area model

In a more applied model of the hydro power unit it can be described by a one-area model. This means that the model serve as the lumped hydro power produced for the FCR-N reserve. The one-area model consist of a PI-controller, a servomotor modelled as a LP-filter and a feedback system with droop. The penstock and turbine are described by (3.18) with a lumped grid model according to (2.5).

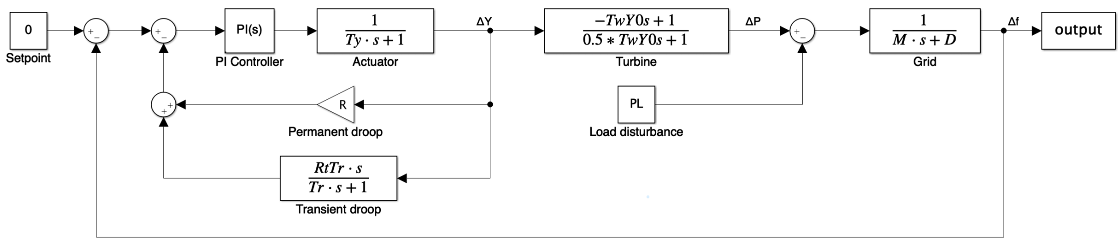

Figure 18: Linear one-area hydro system and grid model.

Figure 18 describes a linear one-area model of a hydro power unit. The input of the model is a reference setpoint and the frequency deviation in per unit (pu). The controller settings K_p, K_i and the droop R determine how the frequency control will be carried out by the hydro power plant, i.e. how much the unit will contribute to the FCR-N. The proportional gain, K_p tries to adjust and counteract the disturbance and the integral term K_i seek to reduce the residual error. The T_y parameter signifies the time constant for the main servomotor or the actuator, T_w is the water time constant for the penstock and Y_0 is the loading. R_r and T_r are parameters for the transient droop setting, which is mainly used to reduced the governor gain and is discounted in this case as seen in (3.22), (3.23). Regarding the grid model, M is twice the system inertia constant and D is the load frequency dependency. The model output is the frequency deviation from the nominal, Δf, in per unit. It has been argued that a time delay could be introduced for the main servo motor [35, 36], i.e.

$$H_{actuator}(s) = \frac{1}{T_y s + 1} \cdot e^{-sT_{del}}. \tag{3.24}$$

However, [37] consider it sufficient to utilize a model with a first order lag. The authors of [36] included the lag since they performed measurements on a hydro unit and the delay was present in the findings, also [35] carried out measurements which could explain why a lag was used in the modelling. Since the parameter settings are largely from measurements of hydro power units [16], the servo motor model from [36] is adapted, thus T_{del} is considered to account for the delay.

Table 9: Typical values and range of parameters for a hydro power plant model [34].

Symbol	Description	Typical value	Range	Unit
T_r	Reset time	5.0	2.5 - 25.0	[s]
T_y	Actuator time constant	0.2	0.2 - 0.4	[s]
T_w	Water time constant	1.0	0.5 - 5.0	[s]
M	System inertia	8.0	6.0 - 12.0	[s]
R	Permanent droop	0.04	0.03 - 0.06	[pu]
R_t	Temporary droop	0.31	0.2 - 1.0	[pu]

In Table 9 typical values and range of parameters are presented for a hydro power unit. Here, the transient droop aspect of the governor is addressed, regarding typical spans and also the actuator time constant which is usually very stable. As can be seen the water time constant has a big span, since it is heavily dependant on the type of turbine that is modelled. Typical values for the Francis turbine are in the range of $T_w = 1 - 1.4$ [3], Kaplan $T_w = 1.6$ or higher [16], and the high-head Pelton turbines $T_w = 0.4$ or less [38].

3.5.1 Backlash and non-linear elements

Concerning hydro power governor configurations, there are usually three types of filtering techniques that are discussed. They are the linear, deadband and floating deadband filters. Floating deadband can be described as a filter that produces an unchanged output for a certain range of inputs, i.e. no action occurs regardless of input signal. Floating deadband filters, or backlash can be utilized to prevent oscillations in a mechanical system. It is defined as the loss of motion within a system and can for instance occur between gears, in the short time span where one gear is not enacting a force on the next one in a sequence.

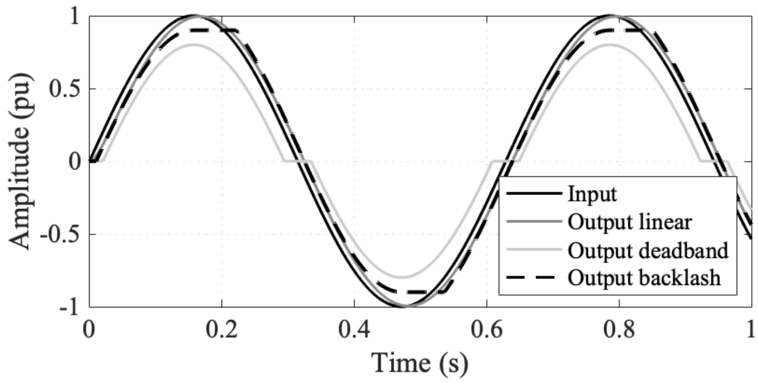

Figure 19: An example of a sinusoidal input signal and corresponding outputs filtered through a linear, deadband and floating deadband filter.

A common occurrence in hydro modelling is backlash, in Figure 19 the influence of a linear, deadband and floating deadband filter, or backlash can be seen for a sinusoidal input signal. Here, the deadband filter is $BL_{db} = \pm 0.2$, the floating deadband $BL_{fdb} = 0.2$ and the linear filter is $F_{lf}(s) = \frac{1}{0.1s+1}$. Note that the values are used to distinguish the differences between the filter types. The linear filter produce a phase shift, whereas the deadband filters produce an unchanged output signal. From Figure 18 backlash is introduced to form a non-linear representation of the one-area system, where the transient droop is omitted.

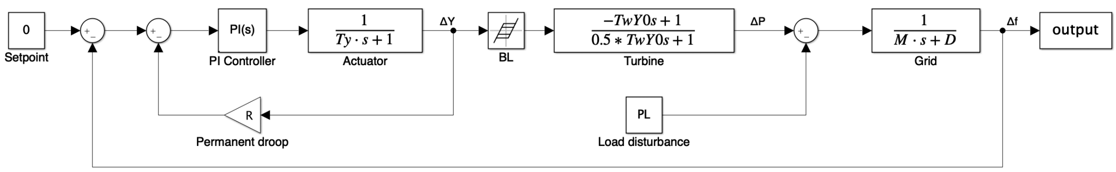

Figure 20: Non-linear one-area hydro system and grid model.

A non-linear one-area system with backlash introduced is presented in Figure 20. In the NPS the predominant part of the FCR-N control response consists of hydro power plants, more specifically, mainly the Francis and Kaplan variant turbines. They utilize similar regulatory elements, the main distinguishing factor is that the Kaplan model has an additional control composed of a runner servomotor. The Francis model rely on solely controlling the GV, while the Kaplan model configuration attempt to achieve an optimized behavior by the balancing the runner servomotor and the GV. Apart from the Francis and Kaplan turbines, Norway is the only country in the Nordic region that also utilize Pelton turbines in their hydro-fleet.

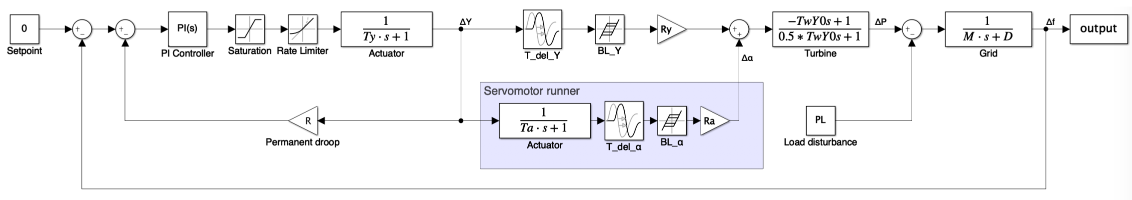

Figure 21: Hydro system layout for a split model for Francis, Kaplan and Pelton with a runner servomotor, non-linearities and time delays.

In Figure 21 a split representation of the different turbines are illustrated where the addition for the Kaplan model is highlighted, for the Francis and Pelton model $R_\alpha = 0$, i.e. it is considered neglected. For Kaplan it is assumed that the power alteration is split in half, where $R_\alpha = R_Y = 0.5$ pu [3]. The parameters R_α and R_Y are representative of the power change of the GV and runner, where the spread is equal for both the servo valve and servo runner. The input of the system is the frequency deviation from the nominal or Δf in pu. The signal ΔY is the change in setpoint for the GVO, similarly $\Delta\alpha$ is the change in the runner blade angle for the servomotor runner. The servomotor runner is exclusive for the Kaplan models where T_α is the time constant of the runner servomotor, R_α, R_Y are the GV power alteration and Y_0 is the unit loading. The system output is the power deviation or ΔP.

Turbine measurements and tests have been carried out by [16] for different Francis and Kaplan turbines. Table 23 in Appendix A illustrate the measured parameters for these types of turbines, where S2, S3 are Kaplan turbines and S4, S5 are Francis turbines. All the units presented are Swedish, which implies that they are of the ASEA/ ABB HYC governor type. In the data from [16] the backlash throughout different HPPs are also thoroughly documented. Apart from the measured values provided in the Table 23, [16] also outline average backlash values from a database consisting of 964 turbines. The average values of the different types of backlash are presented in Table 24 in Appendix A. Other sources [1, 2] have used values of $BL_{gv} = 0.00029$ pu and [3] has set $BL_Y = BL_a = 0.001$ pu. Since [16] has averaged out parameters from a large database the values of the backlash from Table 24 is considered for the model. However, for the Swedish Francis governor the value of $BL_Y = 0.001$ pu is used for the total backlash of the specific turbine [3, 39]. The reason that only the total backlash is presented for the Pelton turbine is that the phenomena occurs in the deflector and needle, rather than in a servo valve, as is the case for the reactionary turbines. Additional non-linearities include the gate-opening and closing, or saturation along with the gate opening and closing velocity of the turbines, or rate limiter described in Tables 26, 27. The time delays from the main servo and the runner servomotor are presented in Table 27.

From [14] a study is conducted regarding the installed capacity of units supplying the FCR-D product. The survey include a variety of different HPPs, where the distribution between the installed capacity and the water time constant of the units have been represented for the Nordic region. To get a system view of the water time constants for different HPPs, as with the backlash distribution from [16] the water time constant data T_w is presented in Table 25 in Appendix A. According to [14], hydro units with water time constants higher than $T_w = 1.8$ s are not qualified for FCR support, which also set the upper limit for the parameter. It is also stated that units qualified to deliver FCR seldom have low K_p and high K_i values, whereas the qualified stable units tend towards higher K_p, which allows for a higher K_i value as well.

3.5.2 Turbine efficiency

Hydro power plants are one of the most effective large-scale production facilities for power generation, typically having an efficiency around 95%. Regarding the efficiency aspect of the turbines the Francis and Pelton types efficiency mathematical expressions are simpler to model than the Kaplan turbine, since they are not dependant on the runner blade servomotor piston position. The efficiency for the Francis turbine can be modelled as

$$\eta = \eta_{max}\left(\sqrt{4 - \left(\frac{Y}{A_m} - 1\right)^2} - 1\right), \tag{3.25}$$

where η_{max} is the maximum efficiency factor, typically 1.05 and A_m is the opening section Y at maximum efficiency, typically 0.7 [40]. Note that η_{max} is not the turbine efficiency, but an efficiency factor to describe the expression of the Francis turbine. For the Pelton turbine the efficiency calculation can be described as

$$\eta = \begin{cases} 1, & if \ \ Y \geq 0.3 \\ 0.7 + Y, & if \ \ 0.13 \leq Y < 0.3 \\ 13.83(Y - 0.07), & if \ \ 0.07 \leq Y < 0.13 \\ 0, & if \ \ Y < 0.07 \end{cases} \tag{3.26}$$

which consist of non-linear elements in contrast to the Francis efficiency calculation [40]. In general, it is not possible to formulate a mathematical expression for the behavior of the Kaplan turbine, because of the complex non-linear characteristics of the turbine [41]. The efficiency function for the Kaplan turbine can be expressed by

$$\eta = \eta(H, \omega, Y, \alpha), \tag{3.27}$$

which is dependant on the head, speed, the GVO and the runner blade angle. Since the turbine characteristics has to be determined by measurement data, using for instance a piece-wise approximation of data points to generate look-up tables for the behavior of the gate-opening (Y) and runner blades behavior (α), the efficiency aspect of the Kaplan HPP units are omitted for this study. Depictions of the relationship between the gate-opening, runner blade angle, efficiency and the approach to generate the look-up tables from measurement data is described in [41].

3.6 System model

The Nordic power system can be modelled according to Figure 15 with multiple FCR-units to assist the total FCR-N response. The different units incorporate the distinct turbine types for each country and rated power of each hydro unit.

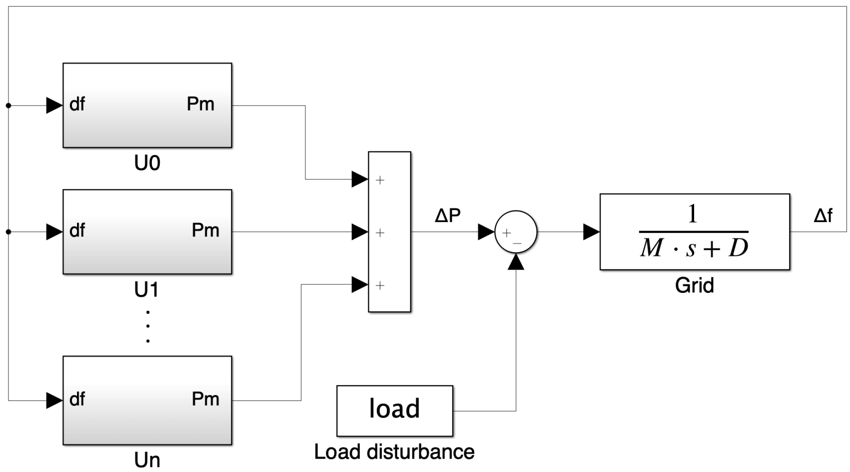

Figure 22: Hydro-fleet model with Francis, Kaplan and Pelton turbines providing FCR-N.

The total FCR-N provided from the sum-total of the combined Francis, Kaplan and Pelton units can be modelled as illustrated in Figure 22, where U_0 represents a Francis unit with the rest of the hydro-fleet up to U_n is the contribution summed together consisting of Francis, Kaplan and Pelton turbine models [3]. The rated power of a hydro unit providing FCR-N is according to the expression

$$S_{n,FCR-N} = E_p \cdot \Delta P \cdot \frac{f_0}{\Delta f}, \tag{3.28}$$

where sub-index n represents the unit, E_p is the droop setting, f_0 the nominal frequency, ΔP is the capacity and Δf is the deviation in frequency [17]. For example, if the capacity is 600 MW and there is a droop setting of 0.06, it would correspond to a rating for the FCR-N providing unit of

$$S_{n,FCR-N} = 0.06 \cdot 600 \cdot \frac{50}{0.1} = 18000\ MVA. \tag{3.29}$$

During normal operational state the FCR-N reserve in the NPS is 600 MW [42]. However, in studies [3, 43] the value of K_{FCR} is set to 73.5 pu, i.e. 7350 MW/Hz. Since it is feasible that the Nordic TSOs buy extra of the FCR-N product from the suppliers and there is an error margin it is unlikely that the value of K_{FCR} is static at 600 MW during an operational hour, therefore the value of $K_{FCR} = 73.5$ pu is considered for this report.

An overview of how the FCR-N product is distributed in the Nordic region is presented in [43], where the 7350 MW/Hz is split as following; FCR-N = 2500 MW/Hz for Sweden, FCR-N = 4230 MW/Hz for Norway and FCR-N = 800 MW/Hz for Finland. With the distribution of the FCR-N and the turbine data from [16], recall Figure 5, it is possible to get an estimate of the FCR-N provided by the specific turbine type, for the different countries.

Table 10: Active FCR-N based on country and turbine type in MW/Hz for the NPS.

Turbine / Country	Francis	Kaplan	Pelton	Total	Unit
Sweden	1435	1065	-	2500	MW/Hz
Norway	2786	283	1161	4230	MW/Hz
Finland	85	715	-	800	MW/Hz

The estimated FCR-N for the different turbine types in the Nordic region is presented in Table 10.

3.6.1 Regulating strength

The regulating strength is an important measurement to categorize the amount of available frequency control capacity that is present in the system. Regulating strength is categorized in MW/Hz, and describes how the power increases for a specific frequency decline. Since the point -1 should not be encircled for a stable system according to Nyquist, the regulatory strength can be analyzed based on the stability margin from (3.6). For our purposes, consider a system following the real axis, in this case the system $F(j\omega_1)G(j\omega_1) = -1$, where the stability criterion required for accepted robustness is established as by the circle formed by the radius $(r-1)+j0$. The loop gain can then be expressed as

$$G_{0|\omega_1} = F(j\omega_1)G(j\omega_1) = \frac{R_0 + \Delta R}{R_0}(1-r)e^{j\pi}, \tag{3.30}$$

where the initial value for the regulatory strength is characterized by $R_0 = 6000$ MW/Hz. The parameter ΔR is the regulating strength that is varied from the initial reserve. The phase margin of a system should generally not be below 20-25°, in [17] it is set to $\varphi_m = 25°$, such that $M_s = \frac{1}{r} = \frac{1}{2sin(\frac{25\pi}{2\cdot 180})} = 2.31$. Thus, to assure a robust design the radius of the circle is $r = 1/M_s = 0.433$. Under these assumptions the maximum increase of the regulatory reserve can be calculated from

$$\frac{(R_0 + \Delta R)}{R_0}(1-r)e^{j\pi} > -1, \tag{3.31}$$

where the maximum regulatory strength that can be used for operation is 10582 MW/Hz. Compared to the current reserve the regulatory strength can increase by $\Delta R = 4582$ MW/Hz and still exert stable behavior during operation [17].

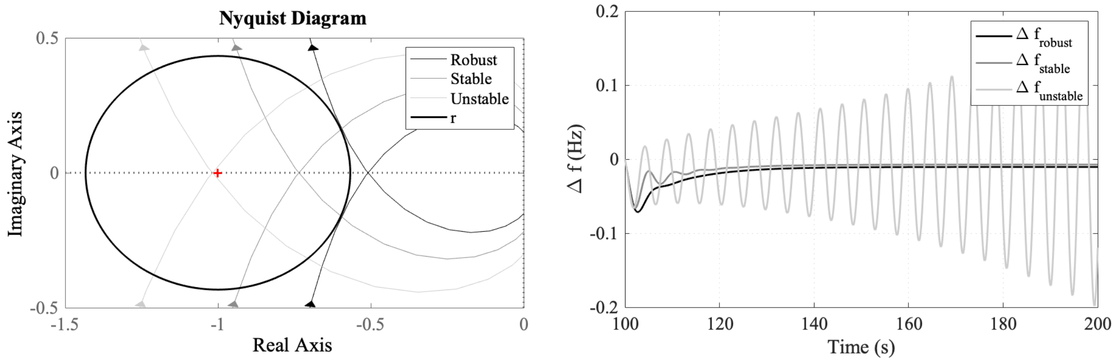

(a) Nyquist curve representing robust stable, stable and unstable operation.

(b) Step response representing robust stable, stable and unstable behavior.

Figure 23: Example visualizing the regulating strengths impact on stability for the loop gain and a step response of (+0.01 pu) for a robust, stable and unstable system.

To illustrate the regulating strengths impact on stability an example case is depicted in Figure 23, where the stability margin for the Nyquist diagram is $r = 0.433$. As can be seen, the robust stable system has a low oscillatory behavior as compared to the system operating inside the stability margin. Once the system reaches beyond the -1 point the system becomes unstable and the oscillations are not dampened out. The regulatory strength is important for system stability and as seen in (2.6), (3.3), since there is a close relationship between the regulating strength R, the kinetic energy of the system E_k and the inertia constant H to evaluate future grid conditions and with regards to frequency balancing products such as FCR, FRR and FFR.

3.6.2 PMU data acquisition

Phasor Measurement Units (PMUs) are monitoring devices in the power system that can provide a wide range of information about the power quality and is mostly used for dynamic monitoring of the grid. Multiple PMU units can act as nodes throughout the power system and provide data on the local conditions and on a more general system level, to view different control areas, or zones. The main application of the PMU in this project is that it produce high accuracy time-synchronization, which results in high resolution frequency data. Since the generation mix varies on an hourly basis, it is important to consider the fine variations down to intra-second levels when analyzing phenomena on shorter time frames. One of the main functionalities of the PMU is to produce a synchrophasor from the data, which is defined as the magnitude and angle of a sinusoidal function time-synchronized at nominal frequency from a Discrete Fourier Transform (DFT). The DFT is expressed as

$$X(j\omega) = \sum_{k=0}^{N-1} x(k) e^{-j\omega k/N}, \tag{3.32}$$

where $x(k)$ is the signal and ω is the discrete angular frequency. The DFT $X(j\omega)$ represents the magnitude and angle of the complex constituent of the signal ($e^{-j\omega k/N}$), with k cycles and N amount of samples.

The PMU utilized can provide a data resolution of 50Hz, i.e. a data update rate of 0.02s. The limitations of the discretization of the signal are a result of the DFT, it also introduce contrived problems including spectral leakage and aliasing. The limitations are mostly base on the length T and the number of samples N, where the relation is

$$f_{limit} = \frac{1}{2\Delta t}, \quad \Delta f = \frac{1}{T}. \tag{3.33}$$

In this case the sampling period is represented by $\Delta t = T/N$. Also, the Nyquist sampling rate must be chosen so that $\Delta t = 1/f_{limit}$.

The PMU utilized in the project is the ABB RES670. The unit is compliant with IEEE Standard for Synchrophasor Measurements for Power Systems, IEEE C37.118-2011 and IEEE C37.118.1-2014. Further, the PMU also utilize IEC 61850-8-1, IEC 61850-9-2 and DNP3.0 for communication protocols.

4 System implementation

In this section the different models are explained separately and the hydro-fleet is built up from the models of the distinct turbine types for Sweden, Norway and Finland. The models are evaluated separately and compared to the hydro-fleet performance using time- and frequency-domain analysis to assess the stability, robustness and performance requirements.

4.1 Linear model

Since the primary frequency control reserve FCR-N predominantly consist of hydro power units [44], the initial step in the modelling was to simulate a hydro power governor and plant to evaluate the net load disturbance.

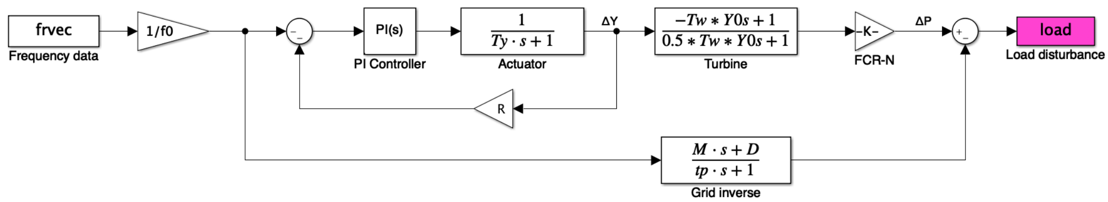

Figure 24: Linear grid inverse, one-area hydro model for generating a net load disturbance from PMU frequency measurements.

The NPS is first modelled according to a linear one-area model of the grid inverse as described in Figure 24. This is investigated to confirm that the model produced a correct net load deviation from the frequency measurements. The model is consistent with the one-area model, but the parameter t_p is introduced in the grid inverse, where $t_p = 0.1$ s. This value is introduced in order to mitigate potential noise from higher-order frequency content. Here, the FCR-N ratio $S_{n,FCR-N}/S_b$ is 15060/65000 for the lumped unit [3]. The ratio calculation is further explained in section 4.3.2.

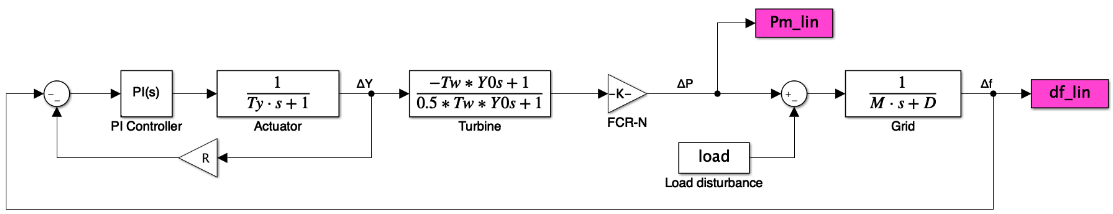

Figure 25: Linear one-area hydro model of the NPS for reconstructing the frequency data from the load disturbance.

The linear representation of the one-area hydro model is described in Figure 25. To validate the load disturbance the from Figure 24 it was utilized, to re-construct the original frequency data, where the input is the load disturbance. The model used for the linear representation of the grid inverse is a lumped Swedish Francis turbine.

Table 11: Parameters for the lumped linear Francis unit [3, 16].

Symbol	Description	Value	Unit
K_p	Proportional gain	1.0	[-]
K_i	Integral gain	0.42	[-]
R	Permanent droop	0.04	[pu/pu]
T_y	Actuator time constant	0.2	[s]
T_w	Water time constant	1.4	[s]
Y_0	Unit loading	0.8	[-]
M	System inertia	7.44	[s]
D	System damping	0.31	[pu]
E_k	Kinetic energy	242	[GWs]
S_b	Power base	65	[GVA]

The parameters for the PI-controller, permanent droop and the turbine parameters for the lumped linear Francis unit are presented in Table 11. The values of M and D are acquired from the frequency data from the PMU. The evaluated hour was 16.00-17.00 15/11-2018, using the inertia estimation tool to extract the values of the inertia and load frequency dependency. The measured PMU frequency data is presented in its entirety on Appendix A.

4.1.1 Results linear model

To evaluate the linear grid inverse model frequency data from 16.00-17.00 15/11-2018 is used as input for the grid inverse.

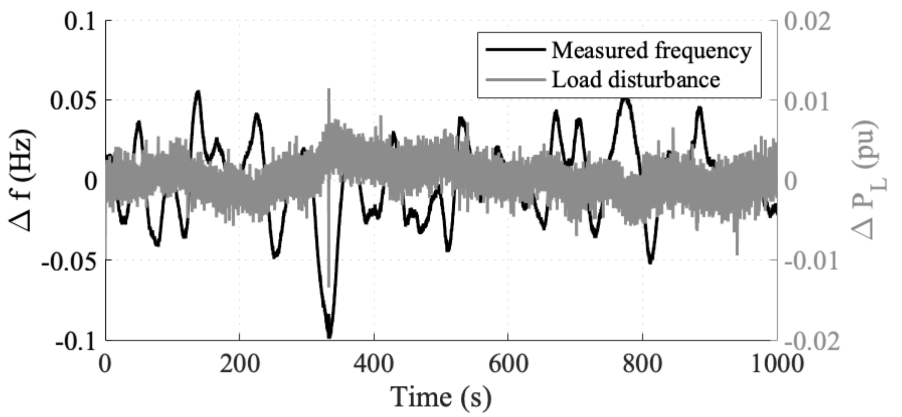

Figure 26: The measured frequency signal from the PMU data 15/11-2018 and the net load disturbance generated from the grid inverse for the first 1000 seconds of the measurement data.

The net load variation from the output of the grid inverse model is presented in Figure 26, along with the measured frequency. The event at 330 seconds is assumed to be a measurement error, since it occurs during 0.1 s. As can be seen a change in frequency corresponds to an opposing change in the load, this can also be derived from (2.1). The output of Figure 24 is utilized as an input to generate a simulated frequency from Figure 25.

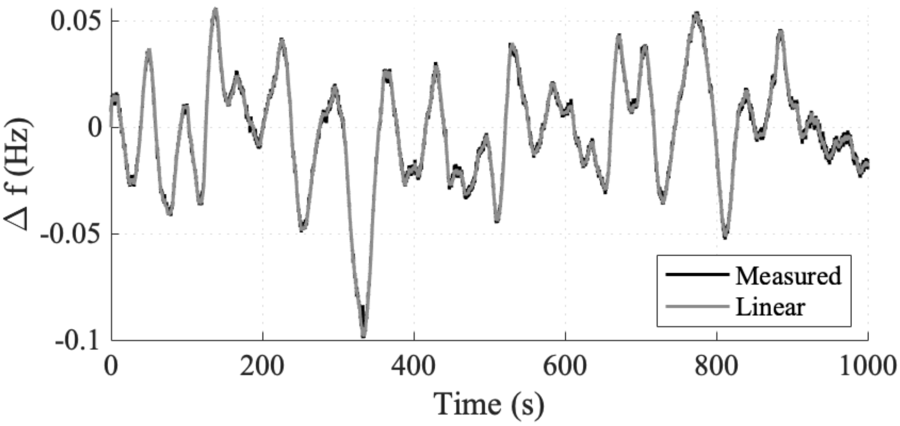

Figure 27: The measured frequency signal from the PMU data 15/11-2018 and the simulated frequency generated from the one-area model for the first 1000 seconds of the measurement data.

In Figure 27 it can be observed that the reconstructed frequency data follows the measured signal well. The more smooth simulated frequency can be explained from the components in the model acting as linear filters, so some amount of noise is mitigated. Since the same approach is used for the hydro-fleet model it is important for further expansion of the model to confirm that the concept functions for a linear model, since the net load disturbance is a central part of the modelling process. The linear model is also used as reference for the hydro-fleet.

4.1.2 Conclusion linear model

From the one-area linear lumped Francis model of the NPS, the simulated frequency data represents the measured frequency well. The simulated data has less noise content, or deviates less than the measured frequency, which can be explained by elements in the models acting as linear filters and therefore there is not a exact match between the data. The linear model is used as a reference for the hydro-fleet, since with less non-linear elements and backlash there is less likelihood of error propagation.

4.2 Non-linear models

To develop the model further from the linear model, the different turbines in the NPS are modelled with non-linear elements implemented, i.e backlash, delays and efficiency calculations. Parameter values for the models are presented in Appendix A.

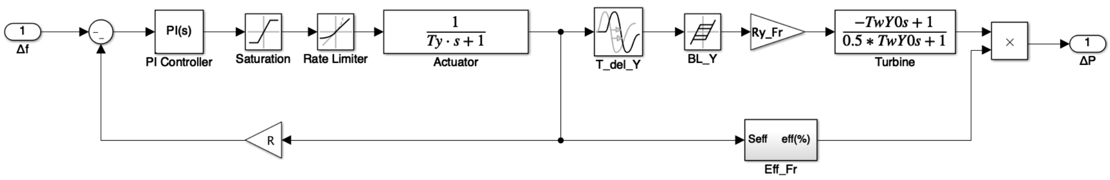

Figure 28: Hydraulic control system overview for a Francis turbine with governor, actuator and non-linear elements.

The control system for the Francis turbine system is described in Figure 28. The main non-linear elements introduced, apart from backlash and the efficiency calculations which have been discussed in sections 3.5.1 and 3.5.2 are the gate opening and closing interactions. This refers to the physical limitation of the wicket gate in terms of maximum gate opening and closing rates for the different turbine. The gate opening and closing is $G_{max} = 1$ and $G_{min} = 0$ according to [2, 40], however since the HPPs must provide up- and down-regulation it is assumed that the values of $G_{max} = 0.5$ and $G_{min} = -0.5$. Physically this would refer to the guide vanes being partially opened, or one regulating unit that is operating at full capacity and one turned off, to be able to provide the regulatory action required.

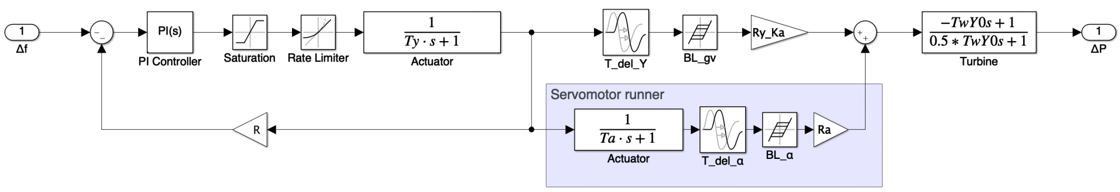

Figure 29: Hydraulic control system overview for a Kaplan turbine with governor, actuator, servomotor runner and non-linear elements.

The control system for the Kaplan turbine system is described in Figure 29. As can be observed, the Kaplan turbine has an additional servomotor, the servomotor runner. The runner blade angle is then regulated to achieve an optimal interaction between the runner and the GV. The values of the backlash are also different from the Francis model, where it is represented by BL_{gv} and BL_{α}.

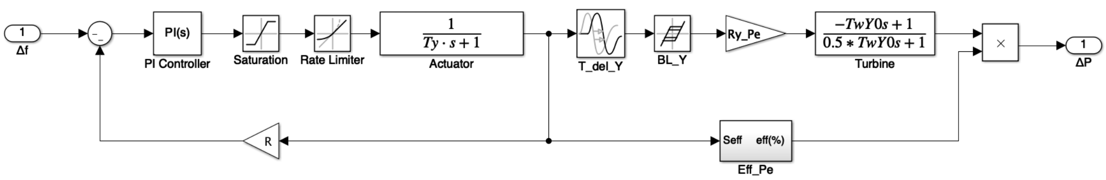

Figure 30: Hydraulic control system overview for a Pelton turbine with governor, actuator and non-linear elements.

The control system for the Pelton turbine system is described in Figure 30. The Pelton model is approximated to a PI-controller system from [16]. As can be seen from the turbine models, the main distinguishing factors are the PI controller parameters, the servomotor runner for the Kaplan model and the water time constant of the turbine and penstock. The backlash elements are distributed throughout the different turbines, where there are backlash for the guide vanes, main servo and the runner servomotor. In the case of the Pelton turbine the backlash accounts for the total backlash, i.e. from the needle and the deflector, since it is of the impulse turbine type.

4.3 Hydro-fleet model

The models are combined into a hydro-fleet for the Nordic region, with the unit share according to the bar diagram in Figure 5, so the generating units are scaled to the order of magnitude that corresponds to its production capacity.

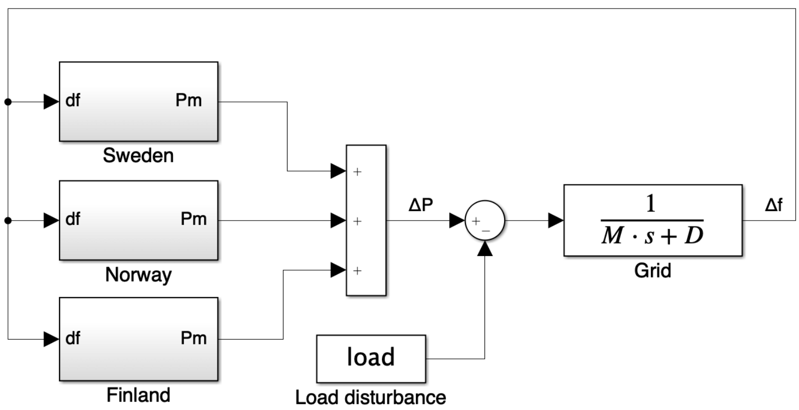

Figure 31: Hydro-fleet model of the frequency response reserve power in the NPS on a country-base.

The hydro-fleet model of the NPS is represented in Figure 31. Each subsystem for the different countries include the non-linear system models from Figures 28-30 based on the specific country.

4.3.1 Parameters and non-linear elements

In order to gain an accurate representation of the different governor and hydro turbine parameter settings, the specifications and documentation from the Nordic TSOs are reviewed. These include Svenska Kraftnät, Statnett and Fingrid for Sweden, Norway and Finland respectively.

Table 12: Parameters specifically tied to the turbine types in the NPS [16].

Symbol	Description	$SE/FI_{Fr,Ka}$	$NO_{Fr,Ka}$	NO_{Pe}	Unit
K_p	Proportional gain	1.0	3	2.5	[-]
K_i	Integral gain	0.42	0.3	0.5	[-]
T_i	Integral time	2.38	10	5	[s]
R	Permanent droop	0.04	0.04	0.04	[pu/pu]

The settings of the PI-controllers and the permanent droops that are distinct for the governors for a specific countries are displayed in Table 12. According to [16], the droop settings for the Swedish and Norwegian governors the standard settings are either 4% or 10%. This is confirmed in [38], where it is stated that the the permanent droop should be regulated between 2-8% in Norway. In the same specification $K_p > 3$ and $T_i < 8$ for good performance, this is also in line with the grid-connected unit measurements performed in [16], although T_i is a bit high, but qualifies for the middle span $8 < T_i < 12$. Therefore the droop of the Norwegian unit is set to 4% to comply with the specification while K_p and K_i are kept as stated in [16] for the 4%-droop case for the Francis and Kaplan turbines. From [16], the values of the Pelton turbine is estimated to $K_p = 2.5$ and $K_i = 0.5$ based on measurements performed on different Pelton HPPs in the NPS. As mentioned previously, the Swedish hydro units usually abide by Vattenfalls E_p-settings. For a 4%-droop setting the corresponding E_p-settings are $K_p = 1$ and $K_i = 5/12 \approx 0.4166$. This seems to fit the parameter settings from [16] well, the K_i parameter is kept since the slight deviation from the formal value could be explained by it being grid-connected. The parameters for Sweden are also compliant with SvKs specification to provide FCR-N [45], i.e.

$$T_{SE} = \frac{1}{E_p K_i} = \frac{1}{0.04 \cdot 0.42} = 59.524 \leq 60\ s. \tag{4.1}$$

Regarding Finland, the recommended setpoint for the permanent droop is also 4% according to [46] with a span of 2-12%. It is assumed that the K_p and K_i settings for the Finnish hydro power units are similar to the Swedish, since they utilize the same governor type in large [16]. In [14], the Nordic TSOs have formulated performance requirements at different kinetic energy levels. Here, the parameter range used was $K_p = 2 - 10$, $K_i = 0.05 - 5$ (scaled to droop), $E_p = 2-8\%$ and $T_w = 1.2-2.2$ s. From the evaluation of different water time constants in the study, it is also stated that the optimal droop setting is $E_p = 0.04$ [14], which is in line with the previous assumptions and droop setting for the chosen governors. The parameters associated with the turbine models are presented in Table 26 in Appendix A.

The values of backlash are the average values throughout the HPPs [16], and the split between the main servo runner and the runner servo motor is half each [3]. The parameters that are common for all the governors and the total system design are described in Table 27 in Appendix A. Note that every HPP is operating at $Y_0 = 0.8$, as from the previous assumption regarding the inertia estimation.

4.3.2 FCR-N ratio and turbine contributions

To scale the different FCR-units contributing to the FCR-N the unit share of turbines are utilized, recalling the turbine split from Figure 5.

Table 13: Unit share of the Francis, Kaplan and Pelton turbine variants for the different countries in the Nordic region [15, 16].

Symbol	Unit share	Sweden	Norway	Finland	Unit
Kr_{Fr}	Francis	0.186	0.408	0.006	[%]
Kr_{Ka}	Kaplan	0.138	0.040	0.051	[%]
Kr_{Pe}	Pelton	-	0.170	-	[%]

The contribution from each production unit in terms of capacity, or the unit share for the different turbines are presented in Table 13. From the production share, under the assumption that the turbine split for the different countries is representative of the FCR-N reserve power contribution that is operated in the power system, an estimation about the rated power of the units can be done. From [3, 30], $S_b = 50000$ MW for the NPS. In 2014 the total installed capacity in the NPS was 102069 MW, where hydro accounted for about 48% of the production [47]. Thus, 48993 MW hydro was installed in 2014 and 50000 MW is therefore a reasonable value for S_b. From the relationship (2.6) the base S_b can be calculated from the production data by the inertia constant and the kinetic energy. Since the power base is known, the system can be scaled by the capacity of units providing the FCR-N response. From (3.28), the relationship between the FCR-N capacity, regulating strength and droop setting is established. The FCR-N capacity can then be calculated according to

$$S_{Nordic,FCR-N} = 0.04 \cdot 753 \cdot \frac{50}{0.1} = 15060\ MVA \tag{4.2}$$

for the hydro-fleet, since the droop-settings are set to $R = 0.04$ and the regulating strength is 753 MW. With the unit share for the different turbine types and the FCR-N capacity ratio the hydro-fleet model can be scaled to the regulating strength of the Nordic grid, for each turbine type.

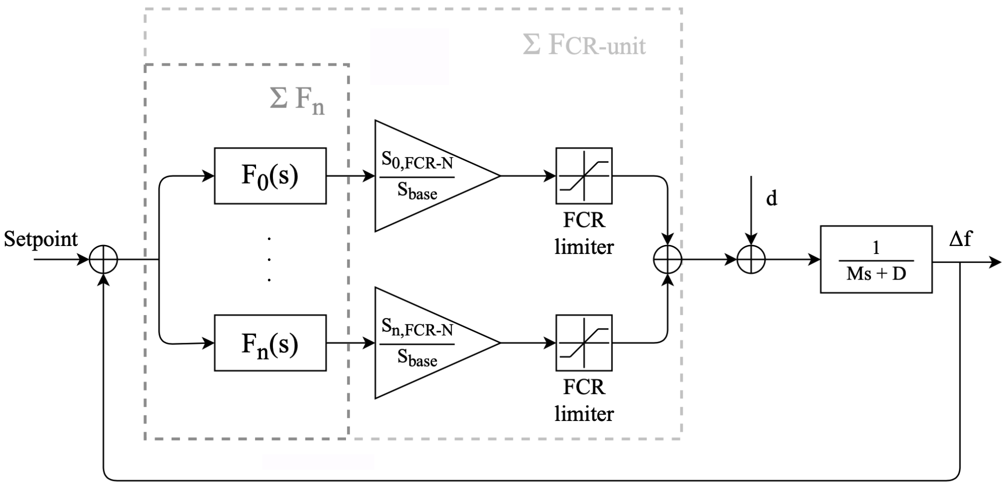

Figure 32: FCR-N capacity scaling for the hydro-fleet model.

The capacity scaling for the hydro-fleet model is presented in Figure 32. Here, $F_0(s)$ represents the transfer function for the normalized unit response, $S_{n,FCR-N}/S_b$ represents the FCR-N capacity in pu and the FCR-limiter is the limitation of the FCR-N capacity, or reserve during a specific hour. However, since the generation mix is not known for the specific hour the estimation is assumed to be constant.

Table 14: Estimation of FCR-N capacity, $S_{n,FCR-N}$, for the different countries in the Nordic region based on turbine type.

Country \ Turbine	Francis	Kaplan	Pelton	Unit
Sweden	2870	2130	-	MW
Norway	5573	565	2322	MW
Finland	170	1430	-	MW

Since the FCR-N capacity is split for the different countries and turbines the contribution for each turbine is presented in Table 14 to clarify, based on the values from Table 10.

Table 15: Estimation of FCR-N limitations for the different countries in the Nordic region based on turbine type.

Country \ Turbine	Francis	Kaplan	Pelton	Unit
Sweden	144	106	-	MW
Norway	279	28	116	MW
Finland	8	72	-	MW

The same principle can be applied to the FCR-limiter, the limitation for the individual units then becomes according to Table 15 in MW and the base S_b depend on the grid condition. To exemplify the ratio calculation, first the assumption is made that the unit share of the turbines are equivalent to the FCR-N contribution. Then, from the value of the regulating strength, in this case 753 MW, the contribution from the specific turbines can be calculated. From [43], the distribution of the FCR-N based on country is known so the capacity can be calculated for the distinct turbine types on a country-base. For the Swedish Francis unit, the FCR-N limitation and capacity would be

$$\begin{aligned} FCR_{type-country} = FCR_{country} \cdot \frac{SE_{type}}{SE_{tot}} = 250 \cdot \frac{0.186}{0.324} = 144\ MW, \\ S_{type-country,FCR-N} = 0.04 \cdot 144 \cdot \frac{50}{0.1} = 2870\ MW. \end{aligned} \tag{4.3}$$

To calculate the FCR limitation, the distribution based on country is multiplied with the unit share of the specific turbine divided by the total unit share of turbines for the country. The capacity scaling is then based on that value and both are divided by the power base to gain per unit values.

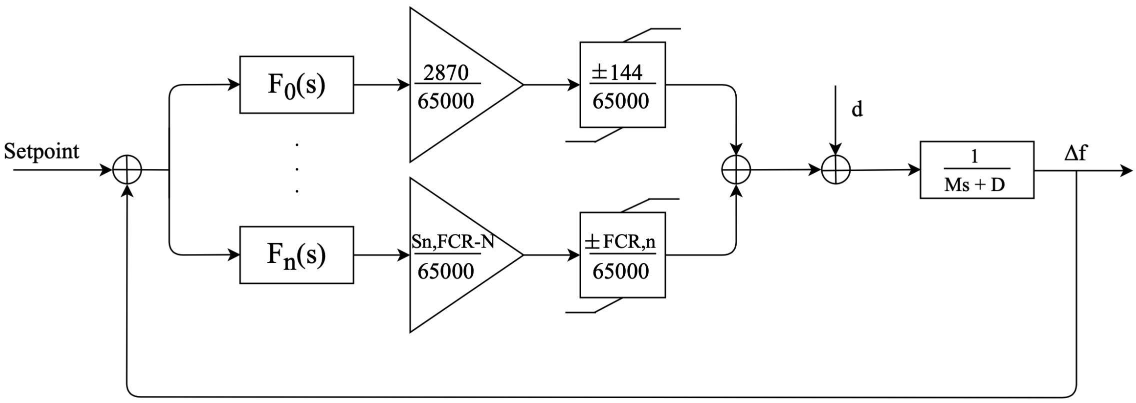

Figure 33: Example of FCR-N capacity scaling for the hydro-fleet model with a specific power base.

To illustrate the capacity and limitation calculation Figure 33 represents a Swedish Francis unit followed by n amount of turbines with a power base of 65000 MVA.

4.3.3 Results hydro-fleet model

The models are combined into a hydro-fleet for the Nordic region, where the FCR-units are scaled according to the ratio contributions. For an overview of the grid inverse model of the hydro-fleet with all sub-elements visible refer to Appendix C.

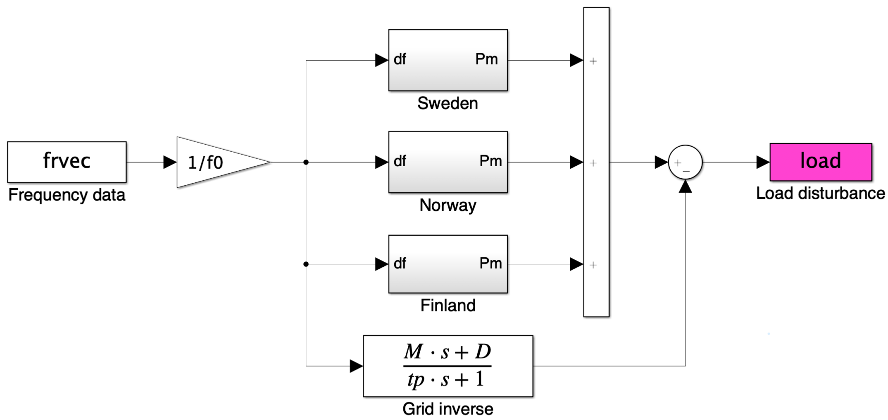

Figure 34: Grid inverse of the hydro-fleet model in the Nordic region.

The grid inverse for hydro-fleet is illustrated in Figure 34, where the input is the frequency data and the output is the net load variation. The output of the grid inverse for the frequency data measured 15/11-2018 and 21/3-2019 is the respective net load variation where a comparison is made with the linear one-area model and the hydro-fleet model. The measured PMU frequency data is presented in its entirety on Appendix A.

Table 16: Inertia estimation for the PMU data based on production data.

Date	M (s)	D (pu)	E_k (GWs)	S_b (GVA)
16-17 15/11-2018	7.44	0.31	242	65
11-12 20/3-2019	7.30	0.34	215	59

The inertia estimations from the PMU data sets are presented in Table 16, where the system inertia, damping, kinetic energy and power base are shown for the specific hour based on production data from ENTSO-E [20].

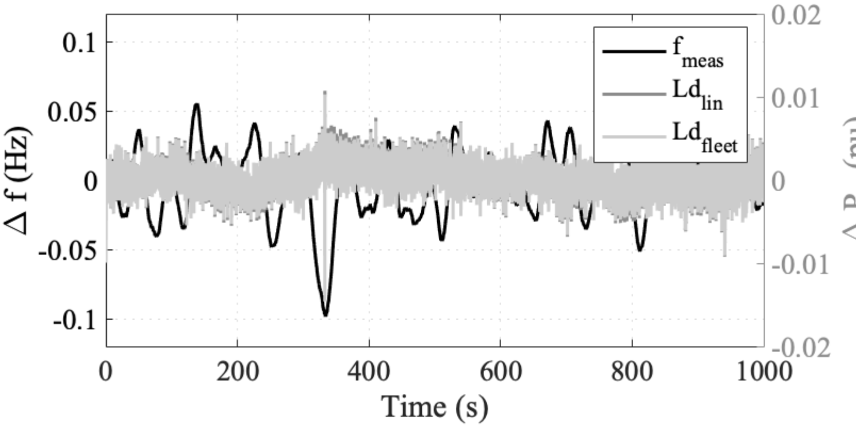

Figure 35: The measured frequency from the PMU data set of 15/11-2018 and the net load disturbance generated from the grid inverse for the first 1000 seconds of the measurement data.

The net load variations from the output of the hydro-fleet model is presented in Figure 35 for 15/11-2018 along with the linear model load variation for reference and the measured frequency.

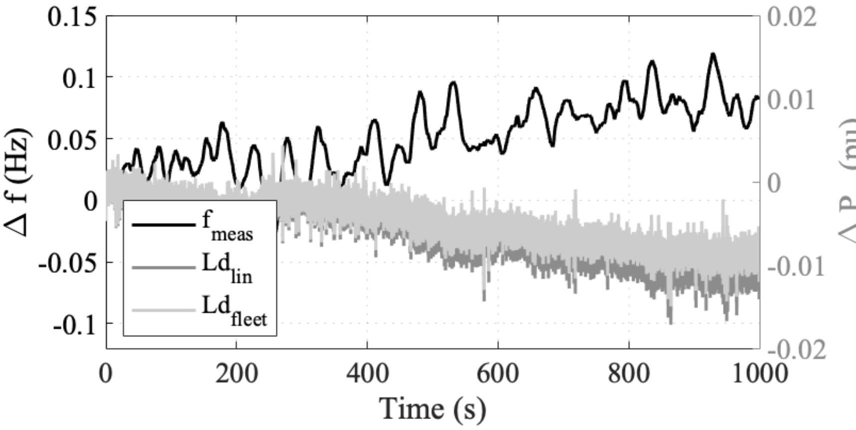

Figure 36: The measured frequency from the PMU data set of 21/3-2019 and the net load disturbance generated from the grid inverse for the first 1000 seconds of the measurement data.

The net load variations from the output of the hydro-fleet model is presented in Figure 36 for 21/3-2019. To validate the load disturbance from the hydro-fleet model the signal was reconstructed to compare with the original frequency data, where the input is the load disturbance from Figures 35 and 36.

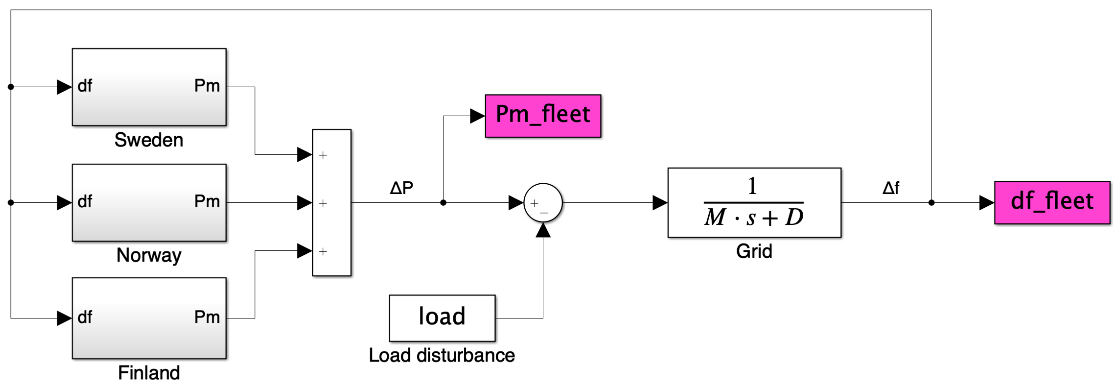

Figure 37: Grid representation of the hydro-fleet model in the Nordic region.

The regular grid model for the hydro-fleet system is illustrated in Figure 37, where the input is the net load variation and the output is the simulated frequency. For an overview of the regular grid model for the hydro-fleet with all sub-elements visualized refer to Appendix C.

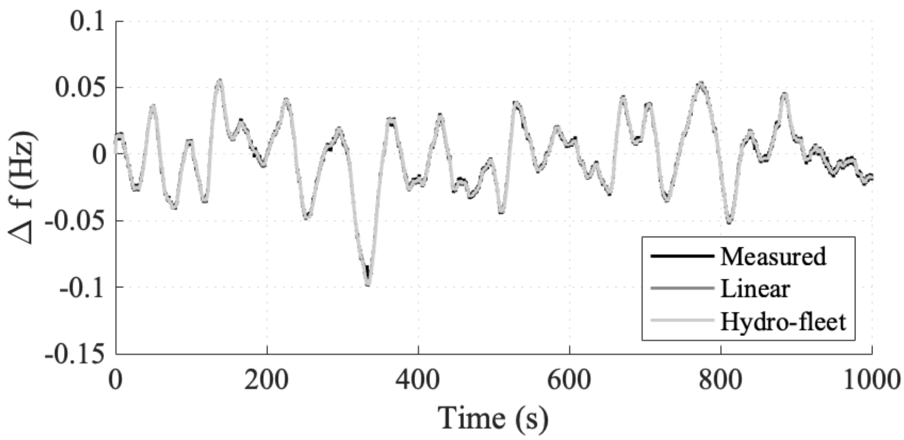

Figure 38: Measured and simulated frequency from the hydro-fleet model of the NPS for 15/11-2018.

The output of the grid model of the hydro-fleet model for 15/11-2018 is presented in Figures 38 where the simulated frequency from the hydro-fleet model is compared to the linear model and measured frequency. As can be seen the simulated frequency data follows the measured signal well, the smoother simulated profile can be explained from the components in the linear model are acting as linear filters, so some amount of noise is mitigated.

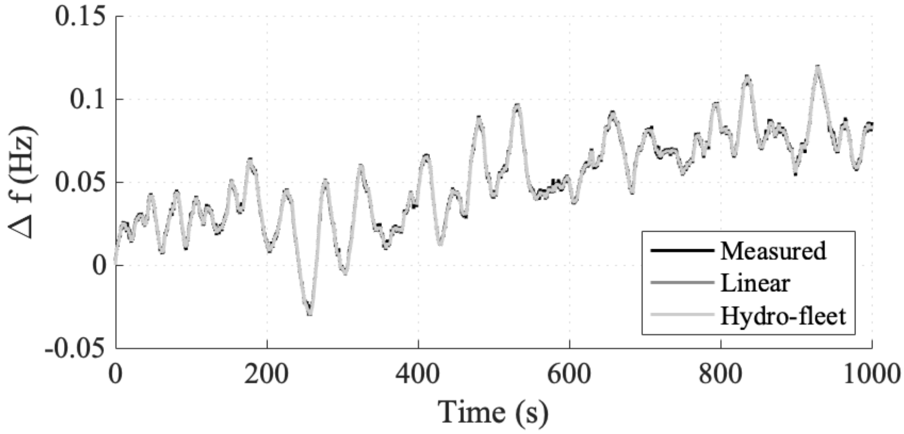

Figure 39: Measured and simulated frequency from the hydro-fleet model of the NPS for 21/3-2019.

The output of the grid model of the hydro-fleet model for 23/3-2019 is presented in Figures 39 where the simulated frequency from the hydro-fleet model is compared to the linear model and measured frequency. As can be seen the reconstructed frequency data follows the measured signal well, where the more smooth simulated data can be explained the same way as the previous example.

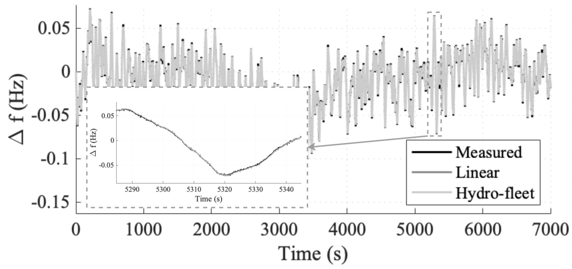

(a) Highest frequency dip 15/11-2018.

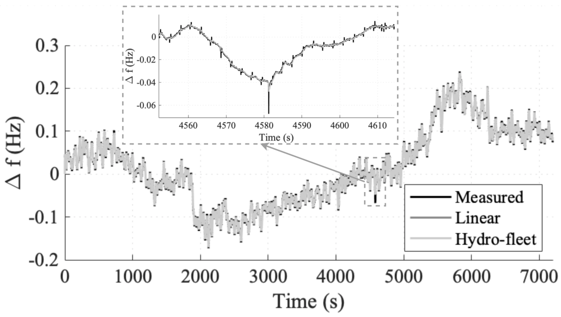

(b) Highest frequency dip 24/03-2019.

Figure 40: The highest frequency dips from the PMU data for 15/11-2018 and 24/03-2019.

The highest frequency dips from the measurement data are presented in Figure 40, to view how the hydro-fleet model behaves during a larger deviation. The frequency dips are illustrated in Figure 40a) and 40b) for 15/11-2018 and 24/3-2019, respectively. As can be seen for the case 2018 the simulated frequency follow the measured frequency well, while with the higher wind penetration case 2019 there is a slight deviation since the simulated frequency is smoothed out. An additional frequency dip is evaluated in Appendix D.

4.3.4 Conclusion hydro-fleet model

From the hydro-fleet model of the NPS, the simulated frequency data represents the measured frequency well. The simulated data has less noise content, or deviates less than the measured frequency, which can be explained by elements in the non-linear model are acting as linear filters and therefore there is not an exact match between the data.

4.4 Frequency quality and time domain analysis

In this section the results of the model in the time-domain are analyzed. The match between the simulated frequency data and the measured PMU data is elaborated on and presented in histogram form. To verify the system stability, a load step change is performed to evaluate the behavior of the specific turbines and the hydro-fleet model.

4.4.1 Simulated frequency data quality

The linear, hydro-fleet model and the measured frequency data are compared in histograms representing the frequency variation in Hz for 15/11-2018. The y-axis represents the normalized number of events in percentage and the x-axis is the range of frequency deviations. There are 25 bins for the histograms, where the range is -0.15:0.012:0.15.

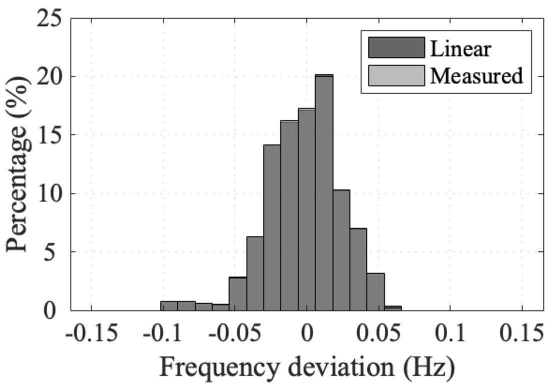

(a) Linear model compared to the measured frequency

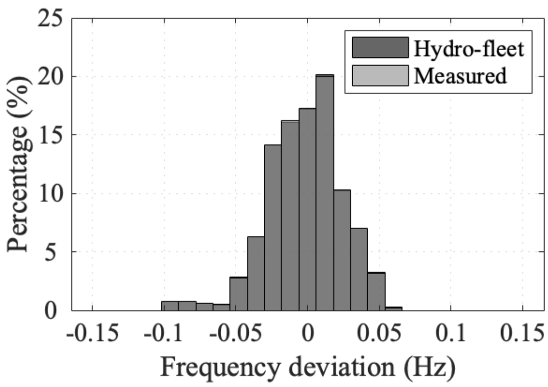

(b) Hydro-fleet model compared to the measured frequency

Figure 41: Histograms describing the variation between the measured and simulated frequency, for the linear and hydro-fleet models, 15/11-2018.

The histograms in Figure 41 describes the comparison in frequency deviations between the linear and hydro-fleet models simulated frequency. As can be seen the difference in variation is very minor. There are slight deviation in the bins, where the simulated data is higher, or pile up closer to the mean. Because the simulated signal is smoother as compared to the measured signal it could explain this decreased spread from the mean.

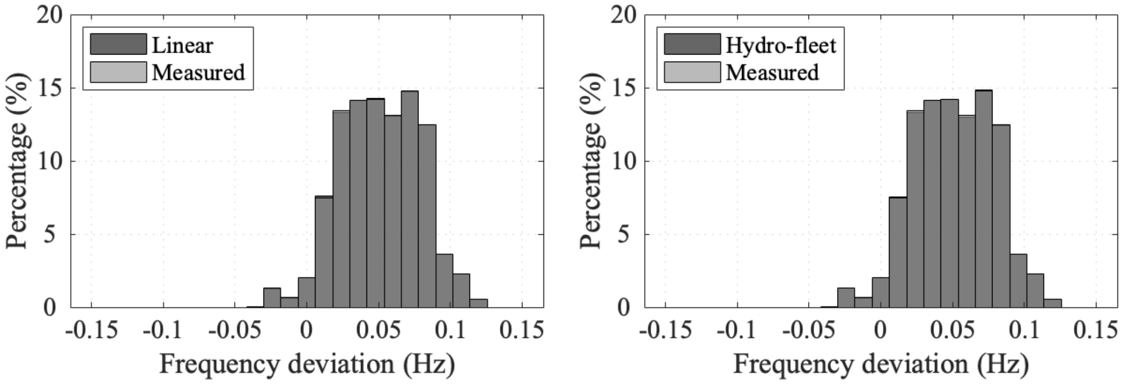

(a) Linear model compared to the measured frequency

(b) Hydro-fleet model compared to the measured frequency

Figure 42: Histograms describing the variation between the measured and simulated frequency, for the linear and hydro-fleet models, 21/3-2019.

The linear, hydro-fleet model and the measured frequency data are compared in histograms representing the frequency variation in Hz for 21/3-2019 in Figure 42. Here, it is noted that the distribution is shifted, since the data-set has a higher amount of wind power, and thus deviates more from the nominal. However, the simulated and measured data again match well, despite 21/3-2019 having a higher amount of wind power penetration.

4.4.2 Load step change evaluation

To evaluate how the different turbine models behaves the individual linear models of the different turbines are subject to a step change of +0.01 pu. The droop setting is 0.04 for all models and the parameter values are presented in Tables 12, 26 and 27.

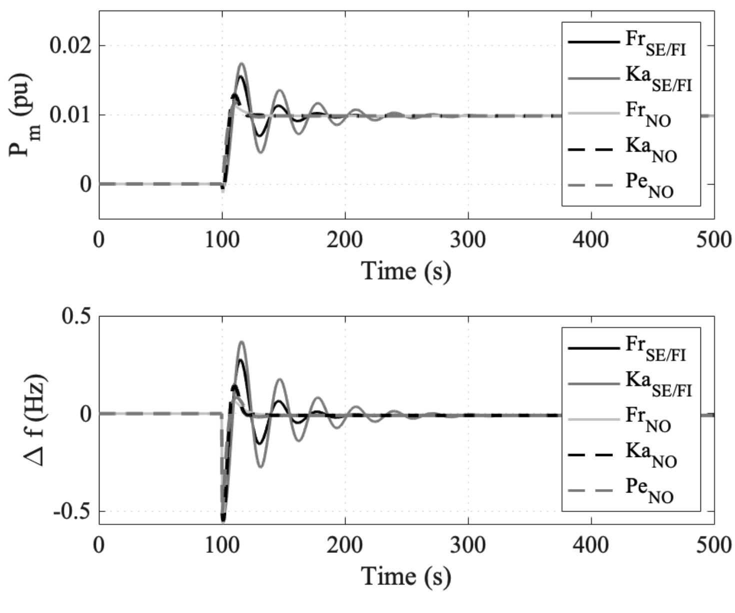

Figure 43: System frequency and power alterations after a step response for Francis, Kaplan and Pelton for SE, NO after a step change of (+0.01 pu).

As can be observed in Figure 43 all models tend to the same value, which is expected since the droop setting is the same. It can be seen that the Swedish/Finnish governor models are more volatile than the Norwegian.

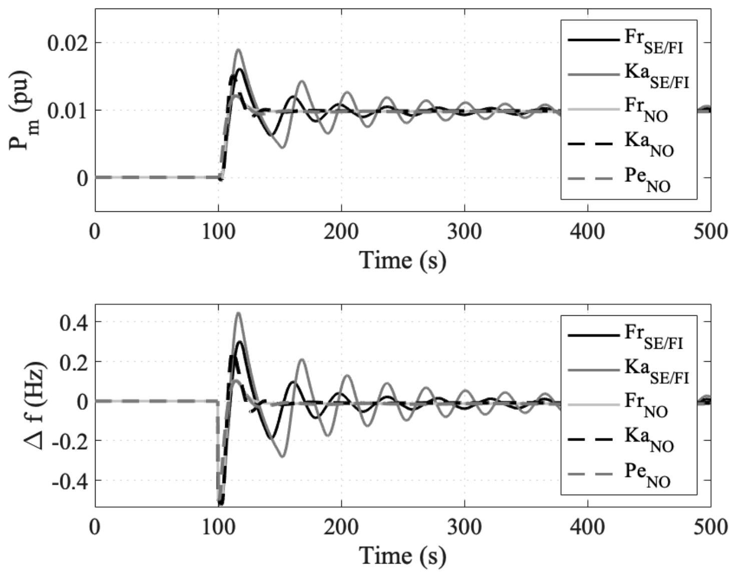

Figure 44: System frequency and power alterations after a step response with non-linear elements introduced for Francis, Kaplan and Pelton for SE, NO after a step change of (+0.01 pu).

The individual non-linear models for the different turbines are subject to a step change of +0.01 pu in Figure 44. The droop setting is 0.04 for all models and the parameter settings are unchanged. The effect of the backlash introduced in the non-linear model can be seen in the step response for $Fr_{(SE/FI)}$ and $Ka_{(SE/FI)}$. The unit share of the models are all 1 for the step change of the individual units, so the effect of the frequency variation around the nominal may not be as severe when the contribution is summed. The behavior in the initial step response 100-150 seconds where there is non-uniform behavior from the response can be explained by the saturation, i.e. the gate opening and closing interactions.

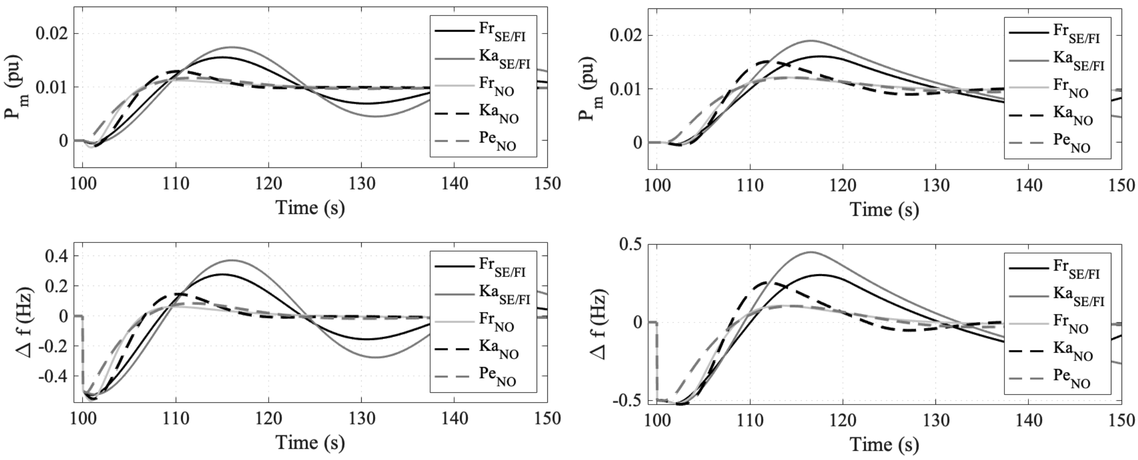

(a) Linear models step response. (b) Non-linear models step response.

Figure 45: Initial step response for the linear and non-linear models for Francis, Kaplan and Pelton for SE/FI and NO after a step change of (+0.01 pu).

In Figure 45, the initial part of the step responses are examined closer where Figure 45a) is the step response of the linear turbines and 45b) is the non-linear turbines. As can be seen the initial behavior of the non-linear system is less sharp then the linear model, the initial peaks reaches higher and creates a state for the SE/FI turbines where no equilibrium is reached.

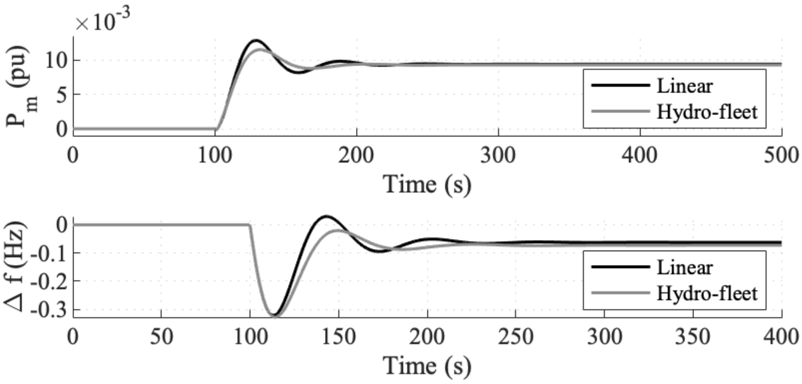

Figure 46: System frequency and power alterations after a step response for the hydro-fleet model of the NPS after a step change of (+0.01 pu) compared with a linear lumped Francis model.

Figure 46 presents a step change of +0.01 pu for the hydro-fleet model compared to the single linear lumped Francis turbine, $Fr_{(SE/FI)}$. In the hydro-fleet model the frequency variations die out after the initial step, implying that the model can handle the units utilizing a higher value for the backlash, e.g. $Fr_{(SE/FI)}$ and $Ka_{(SE/FI)}$.

4.4.3 Conclusion time domain analysis

From the histogram plots the variation in the measured frequency as compared to the simulated case there were slight deviations, where the stacks pile up closer to the mean. This could be explained by the elements acting as linear filters in the models were the simulated signal is smoothed out as compared to the measured signal and thus decreasing the spread from the mean. For a step change in the linear turbine models they all tended towards the same value which was expected since the droop settings are the same, where $R = 0.04$. For a step change in the non-linear turbine models the influence of backlash was visible, where the SE/FI-models did not reach an equilibrium point. However in the hydro-fleet model it tended towards a steady state, which implies that the model can handle the oscillatory behavior after the FCR-N ratio scaling is added in the hydro-fleet model.

4.5 Stability and frequency domain analysis

To analyze the stability of the power system model, a block diagram is composed for frequency domain analysis.

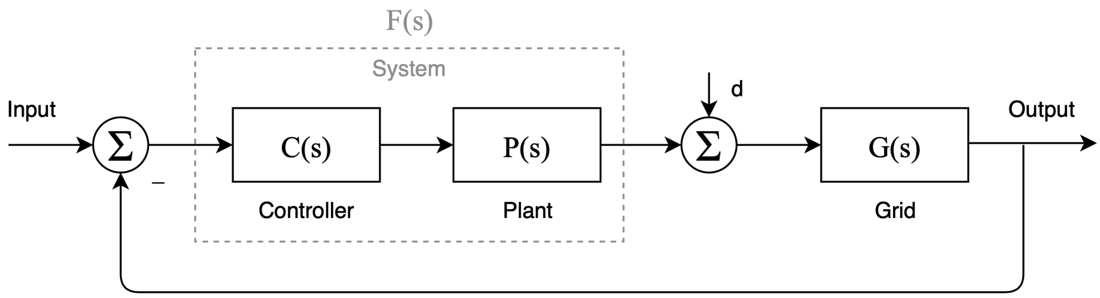

Figure 47: Frequency domain analysis block diagram of the power system.

The block diagram is illustrated in Figure 47. Here, $F(s)$ is the system model with sub-components $C(s)$, the controller and $P(s)$, the plant model. The grid is represented by $G(s)$ and the different system blocks are comprised of the following:

$$Controller: C(s) = \frac{K_p s + K_i}{T_y s^2 + (RK_p + 1)s + RK_i} \tag{4.4}$$

$$Plant: P(s) = \frac{-T_w Y_0 s + 1}{0.5 T_w Y_0 s + 1} \tag{4.5}$$

$$Grid: G(s) = \frac{1}{Ms + D}. \tag{4.6}$$

The parameters of the controller are described in Tables 12, 26 and in Table 27 the parameters for the plant and grid model are presented. The open-loop transfer function of the system is described by

$$\Phi(s) = F(s) \cdot G(s) = \frac{b_{01}s^3 + b_{11}s^2 + b_{21}s + b_{31}}{c_{01}s^4 + c_{11}s^3 + c_{21}s^2 + c_{31}s + c_{41}}, \tag{4.7}$$

where the specific coefficients for the transfer functions are described in Table 30 in Appendix A. The general expressions of the transfer function coefficients are described by

$$\begin{aligned}
&b_{01} = 0;\ b_{11} = -K_pY_0T_w;\ b_{21} = K_p - K_iY_0T_w;\ b_{31} = K_i;\\
&c_{01} = 0.5Y_0T_wMT_y;\ c_{11} = 0.5Y_0T_wM(1 + RK_p) + (0.5Y_0T_wD + M)T_y;\\
&c_{21} = 0.5Y_0T_wMRK_i + (0.5Y_0T_wD + M)(RK_p + 1) + T_yD;\\
&c_{31} = (0.5Y_0T_wD + M)(RK_i + D(RK_p + 1)\ c_{41} = RK_iD.
\end{aligned}$$

4.5.1 Nyquist stability

In order to evaluate the stability of the different hydro-units, the Nyquist stability criterion is used. The phase margin of a system should generally not be below 20-25°, in [17] it is set to $\varphi_m = 25°$, such that $M_s = \frac{1}{r} = \frac{1}{2sin(\frac{25\pi}{2\cdot 180})} = 2.31$. Therefore, to assure a robust design the response of the system should not enter the inscribed circle around the instability point -1. The radius of the circle is $r = \frac{1}{M_s} = 0.433$.

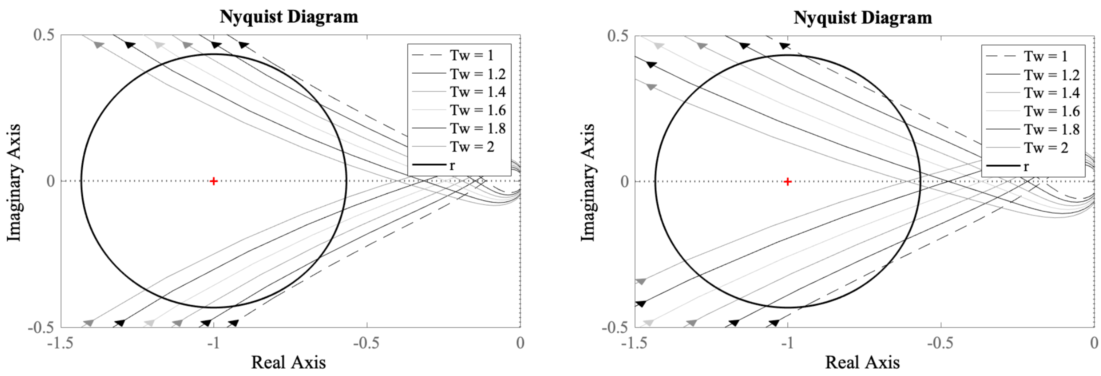

(a) Nyquist plot for the more general case, [3], where $M = 11$, $D = 0.5$.

(b) Nyquist plot for the specific case, 15/11-2018, where $M = 7.44$, $D = 0.31$.

Figure 48: Nyquist stability plot for the Swedish/Finnish Francis and Kaplan turbines for varied water-time constants T_w, from 1-2.

The Nyquist plot in Figure 48 describes the Swedish/Finnish parameter settings with a sweep of the water time constant, T_w. As can be seen the Swedish/Finnish governor does not fully comply with the robustness criteria for higher values of T_w. The typical value range for the Francis turbine $T_w : 1 - 1.4$ is barely outside the robustness criteria for the lower value, while the Kaplan turbine is inside the encircled region with $T_w = 1.6$. Figure 48a) represents a more general value of the system inertia and frequency dependency, i.e. $M = 11$ and $D = 0.5$, while 48b) represents the specific scenario for 15/11-2018, with $M = 7.44$ and $D = 0.31$. As can be seen the response is tending towards the unstable region in the more volatile system scenario and the high-head Francis turbines are also encompassed in the encircled area.

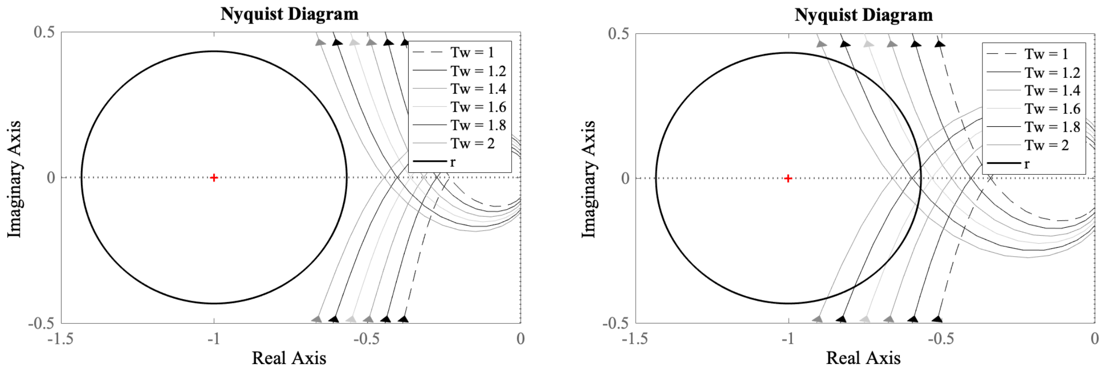

(a) Nyquist plot for the more general case, [3], where $M = 11$, $D = 0.5$.

(b) Nyquist plot for the specific case, 15/11-2018, where $M = 7.44$, $D = 0.31$.

Figure 49: Nyquist stability plot for the Norwegian Francis and Kaplan turbine for varied water-time constants T_w, from 1-2.

The Nyquist plot is described in Figure 49 for the Norwegian parameter settings of the Francis and Kaplan turbines with a sweep of the water time constant, T_w. As can be observed from Figure 49a), the response of the system does not enter the encircled robustness margin. For most of the common values of the Francis and Kaplan the model comply with the design criteria, but for very low-head turbines the robustness margin is reached for the lower inertia condition.

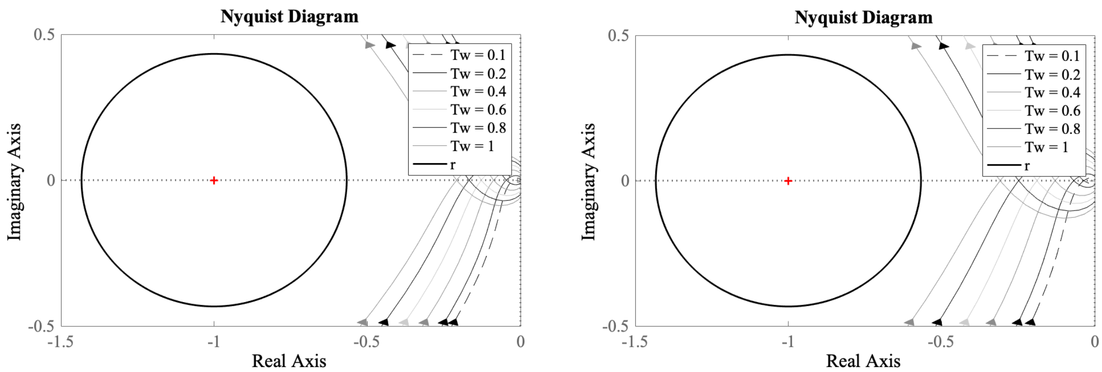

(a) Nyquist plot for the more general case, [3], where $M = 11$, $D = 0.5$.

(b) Nyquist plot for the specific case, 15/11-2018, where $M = 7.44$, $D = 0.31$.

Figure 50: Nyquist stability plot for the Norwegian Pelton turbine for varied water-time constants T_w, from 0.1-1.

In Figure 50 the Nyquist plot is described for the Norwegian parameter settings of the Pelton turbine with a sweep of the water time constant, T_w. Since the Pelton turbine is of the high head turbine variant, the values of the water time constant is therefore significantly lower for the sweep than for the previous cases, see (3.13) for the relationship between the head and the water time constant. As can be seen the Pelton system response also comply with the robustness margin. To evaluate the hydro-fleet model, the system is compared to a model of the Nordic region from [30]. The hydro unit is a one-area representation of the Nordic grid which utilize the linear penstock and turbine model, backlash and a scaling for the FCR-N based on the regulating strength 7530 MW/Hz with a similar calculation of $S_{n,FCR-N}$ as from (3.28).

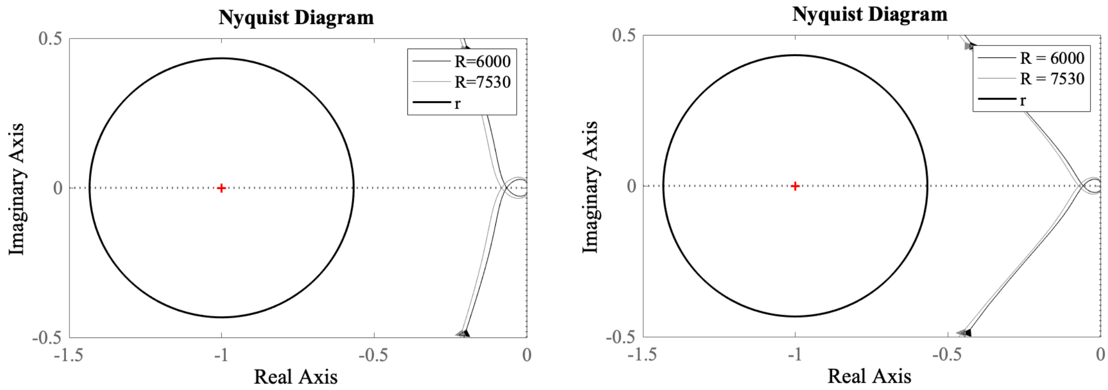

(a) Nyquist plot for a Nordic power system model according to [30].

(b) Nyquist plot for the suggested hydro-fleet model for the Nordic system.

Figure 51: Nyquist stability plot comparison for the model presented in [30] and the suggested hydro-fleet model of the Nordic power system.

A comparison between the hydro-fleet model and the one-area model presented in [30] is illustrated in Figure 51, to evaluate the behavior of the suggested model. In Figure 51a) the Nyquist plot for the one-area model of the NPS presented in [30] is shown and the hydro-fleet model is depicted in Figure 51b). Both models are outside the stability margin and the one-area model cross the real axis at 0.083, whereas the hydro-fleet model cross at 0.074. Since the behavior of the hydro-fleet is similar to the lumped one-area model of the Nordic region, this implies that the ratio estimation for the turbines are feasible.

4.5.2 Conclusion frequency domain analysis

The Swedish/Finnish Francis and Kaplan turbines are more prone to instability when subject to a change in the system inertia and the load frequency dependency, since they are not complying with the recommended criteria for robust stability, however they still exert stable behavior. The Norwegian Francis and Kaplan turbines adhere to the robustness criteria, however for the high-head variants the robustness margin is reached. Finally, the Norwegian Pelton turbine has a robust behavior for both cases. For the total hydro-fleet composed of the analyzed turbines, it has a similar behavior to another NPS representation, [30], which implies that the scaling ratios have been implemented with an acceptable accuracy.

5 Inertia estimation, forecasting and scenarios

In the Nordic region, the TSOs utilize an online tool for inertia estimation in the SCADA system. It tracks the generators inertia constants connected to the grid and the position of the breakers, however the connection points are somewhat scarce, but new information about the generators in the NPS and the inertia constants are updated continuously [48]. Initially this section is concerned with an inertia estimation and damping constant for the current year, 2019, for the specific frequency of the PMU-data for the generation mix at the hour it was collected. Furthermore, it address a lower inertia forecast of the NPS, or scenario for the year 2040. The production data used to calculate the inertia estimation is from the ENTSO-E transparency platform, where hourly production data based on the generation mix of the specific country or zone, for DK2, is available. Production data for the scenario cases 2040ref, 2040high and 2040low is also utilized for the inertia estimation. The inertia estimation tool that calculate the parameters is based on the production data and the estimated inertia constants from Table 1. The assumptions for the estimation are described in [7].

5.1 Case 15/11-2018

PMU-data from 15/11-2018 is utilized in the inertia estimation for the hour 16.00-17.00. The value of $H_{sys-nordic}$ is calculated to 3.72s for the specific time according to (2.10).

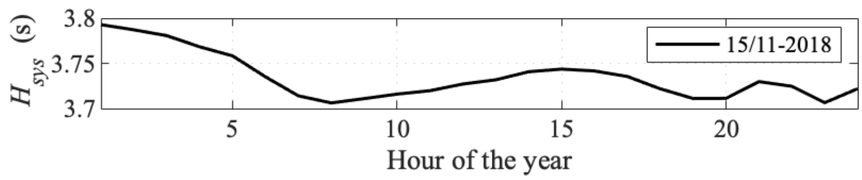

Figure 52: Power system inertia estimation, $H_{sys-nordic}$ for 15/11-2018.

The inertia estimation during the full day for 15/11-2018 is illustrated in Figure 52. The values of $H_{sys-nordic}$ varies from 3.71 to 3.79, with a mean value of 3.73 s.

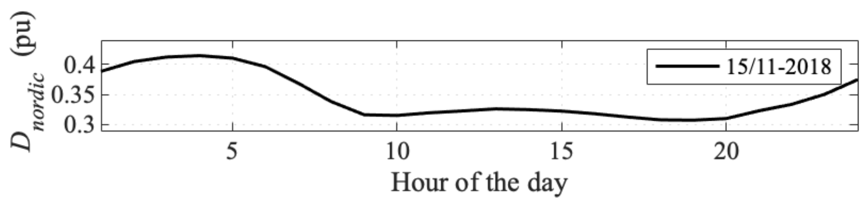

Figure 53: Power system frequency dependency, D_{nordic} for 15/11-2018.

The frequency dependency estimation during the day for 15/11-2018 is illustrated below in Figure 53. The values of D_{nordic} varies from 0.31 to 0.41, with a mean value of 0.35 pu. In the Swedish grid, the damping of the power system, or the frequency dependency of the load D, is 400 MW/Hz according to [49]. Under the assumption that the frequency dependency in the Nordic region is similar, and that the frequency is stable at 50 Hz, the value of D_{nordic} can be calculated for the specific time.

5.2 Scenario 2019

The different scenarios are based on the scenarios from the TYNDP2018, which elaborates on long-term scenarios for 2030 and 2040. SvK together with the Nordic TSOs have developed a common reference scenario for 2040 for the Nordic Grid Development Plan 2019, which has a higher level of detail for the Nordic countries than the TYNDP-scenarios. The base for these scenarios are the production data for the 2019 scenario. Since SvKs production data contain multiple sets of different weather years, the simulation for the 2019 scenario and the 2040ref scenario will be reffered to as weather year 1. The data for the 2019 scenario is solely based on SvKs estimated production data for the year.

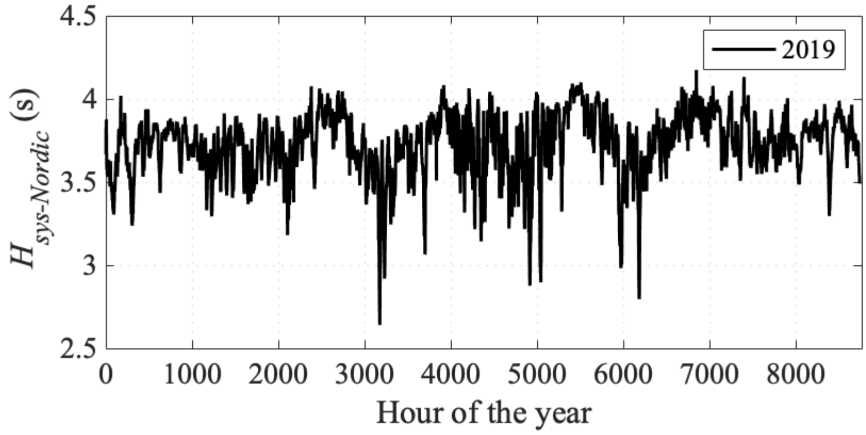

Figure 54: Power system inertia, $H_{sys-nordic}$ for 2019.

The inertia estimation for the 2019 scenario based on the production data from SvK is presented in Figure 54. The values of $H_{sys-nordic}$ varies from 2.64 to 4.17, with a mean value of 3.73 s.

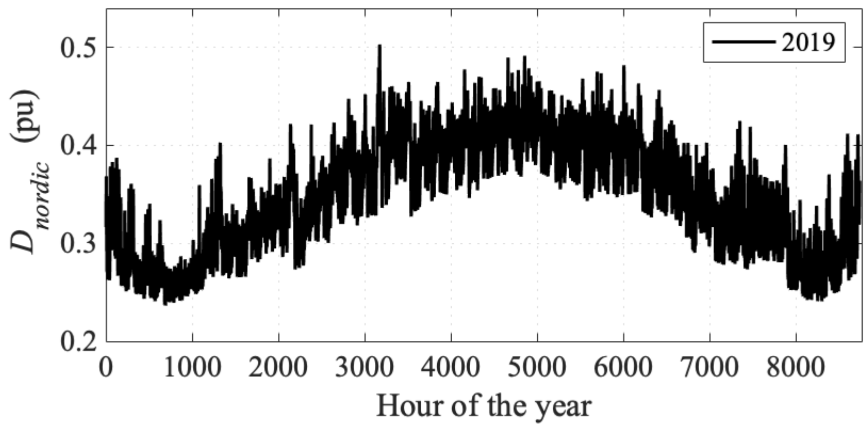

Figure 55: Power system frequency dependency, D_{nordic} for 2019.

The frequency dependency of the load for the 2019 scenario is presented in Figure 55. The values of D_{nordic} varies from 0.24 to 0.50, with a mean value of 0.34 pu. The kinetic energy of the system can be calculated according to (2.6), where

$$S_{b-sys} = \frac{P_{hydro}}{0.8\cos(\phi_{hydro})} + \frac{P_{nuclear}}{\cos(\phi_{nuclear})} + \frac{P_{thermal}}{\cos(\phi_{thermal})} + \frac{P_{wind}}{\cos(\phi_{wind})} + \frac{P_{solar}}{\cos(\phi_{solar})}, \quad (5.1)$$

which is the power system capacity, on an hourly basis for the Nordic region [7].

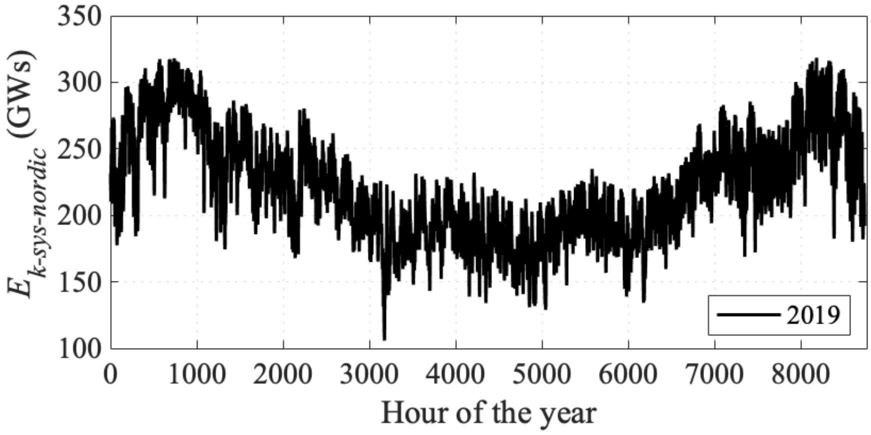

Figure 56: Kinetic energy in the power system, $E_{k,sys-nordic}$ for 2019.

As can be seen in Figure 56 the kinetic energy peaks in December with 318 GWs and the minimum occurs in April with 106 GWs, with a mean value for 2019 of 223 GWs.

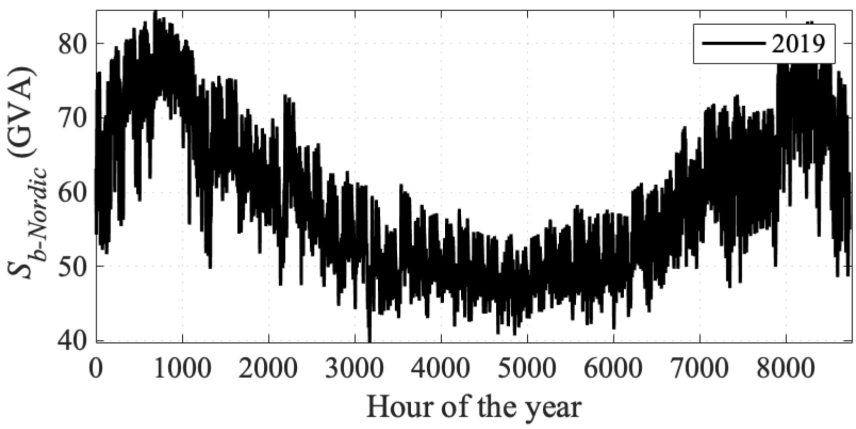

Figure 57: Power rating or online capacity in the power system, $S_{b,sys-nordic}$ for 2019.

The calculated capacity can be seen in Figure 57, which varies from 40 to 85, with a mean value of 60 GW. The 2019 scenario is used as a base case to compare with the inertia estimation for 2040.

5.3 Scenario 2040

The scenario 2040ref has been developed by the Nordic TSOs as a common reference scenario from the long-term market analysis LMA2018 and is based on SvKs estimated production data from a specific weather year [24].

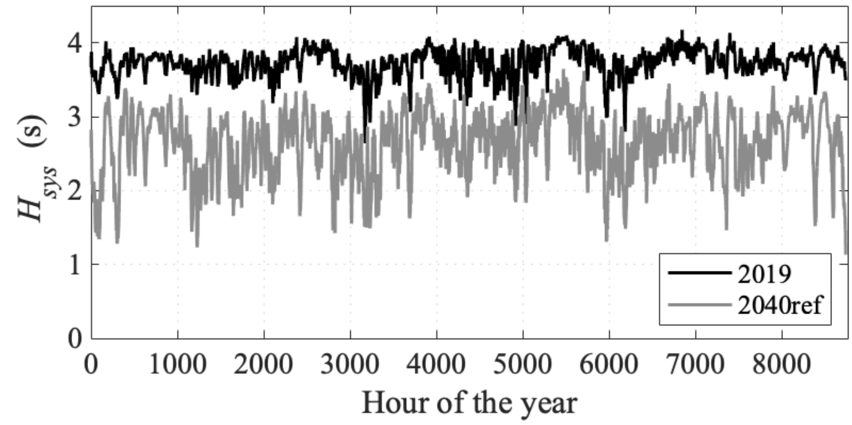

Figure 58: Power system inertia, $H_{sys-nordic}$ for 2019/2040ref.

The inertia estimation for the 2040ref scenario is presented in Figure 58. The values of $H_{sys-nordic}$ varies from 1.13 to 3.64, with a mean value of 2.64 s.

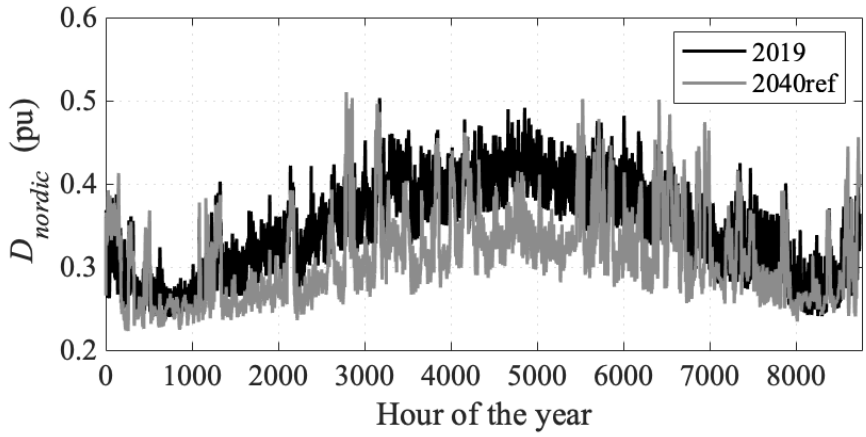

Figure 59: Power system frequency dependency, D_{nordic} for 2019/2040ref.

The frequency dependency of the load for the 2040ref scenario is presented in Figure 59. The values of D_{nordic} varies from 0.22 to 0.51, with a mean value of 0.31 pu.

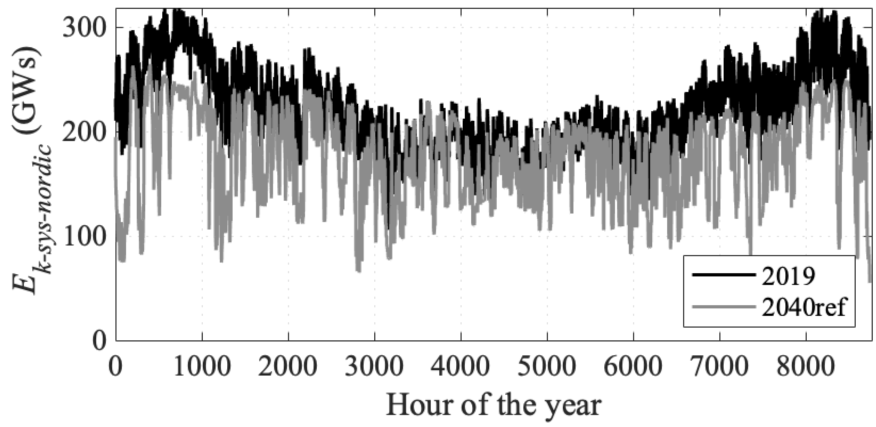

Figure 60: Power system kinetic energy, $E_{k-sys-nordic}$ for 2019/2040ref.

The kinetic energy of the power system for the 2040ref scenario is presented in Figure 60. As can be seen the kinetic energy peaks in December with 265 GWs and the minimum occurs in April with 55 GWs, with a mean value for 2040ref of 175 GWs.

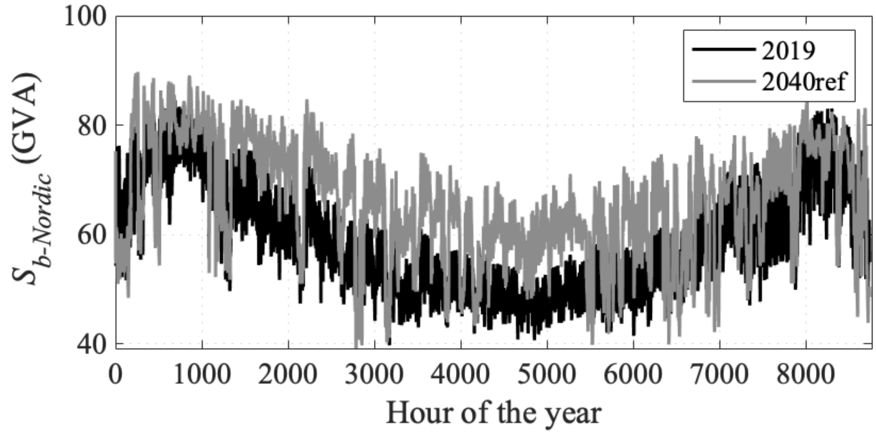

Figure 61: Power rating or online capacity in the power system, $S_{b,sys-nordic}$ for 2019/2040ref.

The calculated capacity can be seen in Figure 61, which varies from 39 to 90, with a mean value of 66 GW. The higher and lower scenarios are presented in Appendix B, where the inertia constants, load frequency dependency, kinetic energy and capacity are presented.

5.4 Forecasting ST2040, ENTSO-E

From the model of the hydro-fleet, a scenario for 2040 can be estimated based on scenario data from ENTSO-E and SvK. First the ENTSO-E scenario is presented and then the scenarios from SvKs LMA2018 report is elaborated on, since the production data from SvK can be used for further analysis. The ENTSO-E scenarios are the Sustainable Transition (ST), Distributed Generation (DG) and Global Climate Action (GCA). The common Nordic reference scenario in LMA2018 is based on the ST scenario from ENTSO-E, so it is used for the scenario estimation. From [21, 22], the percentage distribution of the installed capacity based on country is known. Thereby, the 2040 scenario is calculated by scaling production data from ENTSO-E:s transparency platform for 2019 to an estimation of the system inertia M, and the load frequency dependency D. From an inertia estimation of ST2040 for the evaluated hour, $M = 5.40$ s and $D = 0.32$ pu as compared to 2019 where $M = 7.02$ s and $D = 0.40$ pu. The kinetic energy is estimated to $E_k = 168$ GWs and the online capacity $S_b = 62$ GVA, as compared to $E_k = 177$ GWs and $S_b = 50$ GVA in 2019. The load disturbance is generated for the 2019 grid condition, from the measured PMU-data 23/3-2019, and is run in a regular grid model under weaker grid conditions, i.e. for ST2040.

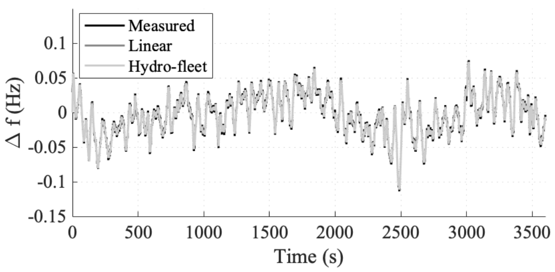

(a) Frequency data based on the 2019 ENTSO-E production data.

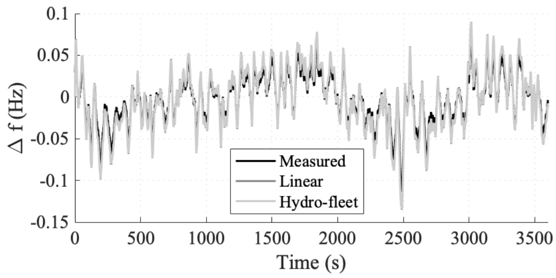

(b) Frequency data based on the 2040 ENTSO-E estimation

Figure 62: Frequency describing the variation between the measured and simulated frequency data, for 2019 and 2040 based on the ENTSO-E estimation.

The resulting frequency from the ENTSO-E scenario is presented in Figure 62. Here, it can be seen that the frequency of the hydro-fleet estimation starts to deviate from the measured data. The PoNB for the particular hour examined is $PoNB_{2019} = 0.4\%$ for the 2019 frequency and $PoNB_{2040} = 1.25\%$ for the 2040 estimate.

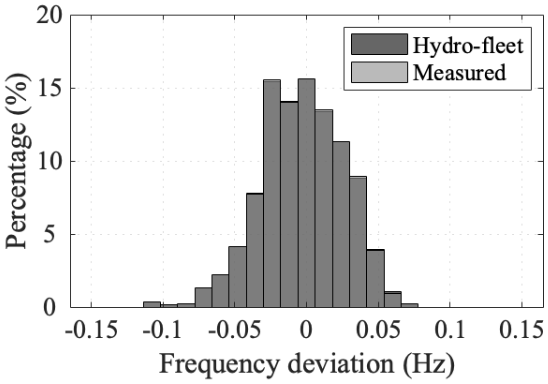

(a) Histogram based on the 2019 ENTSO-E production data.

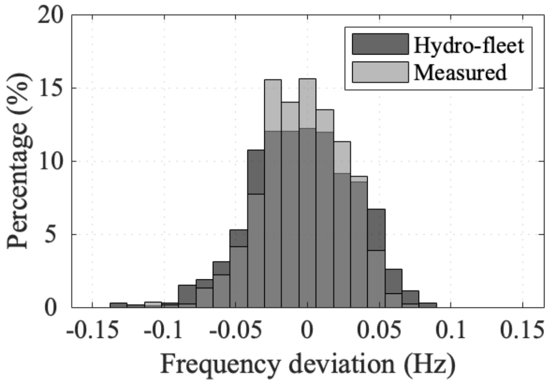

(b) Histogram based on the 2040 ENTSO-E estimation.

Figure 63: Histograms; evaluating the variation between the measured and simulated frequency data, for 2019 and 2040 based on the ENTSO-E estimation.

In Figure 63 the variation in frequency is more visible, where histograms illustrate the frequency deviations, comparing 2019 to 2040. As can be seen the frequency deviates more from the measured frequency data, since there is less inertia present in the system. The estimate for 2040 is more flattened as compared to the measured, since there are more events with higher variation from the mean. Note that the span is still mostly in normal operational conditions.

Table 17: Inertia estimations for the ST2040 scenario.

Year	M	%	D	%	E_k	%	S_b	%	PoNB	%
23/3-2019	7.02	1.0	0.4	1.0	177	1.0	50	1.0	0.004	1.0
23/3-2040	5.40	0.77	0.32	0.8	168	0.95	62	1.3	0.013	3.13

5.4.1 Regulating strength

Since the regulating strength is a crucial factor for the regulatory reserve products, the sensitivity for the parameter is evaluated for the estimated frequency data. The regulating strength of $R = 753$ MW was used as a reference and $R = 600$ MW, $R = 1058.2$ MW for a lower and upper value. The lower value is the amount of FCR-N for 2019 and the higher value is based on the reasoning from section 3.6.1.

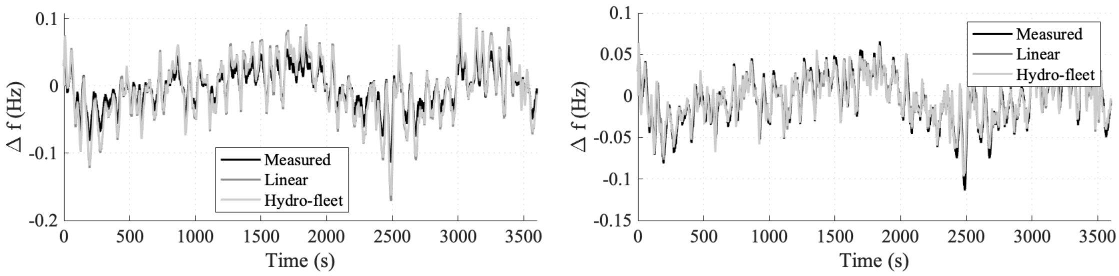

(a) Frequency data based on the ST2040 estimate for $R = 600$ MW.

(b) Frequency data based on the ST2040 estimate for $R = 1058.2$ MW.

Figure 64: Frequency describing the variation between the measured and simulated frequency data, for 2040 based on the ENTSO-E estimation for different regulating strengths.

The estimated frequency data for the different regulating strengths are illustrated in Figure 64. As can be seen the frequency deviations decrease for the higher regulatory strength. From the relationship between the regulatory strength and the kinetic energy (3.3) the regulatory strength for 2040 can be approximated, neglecting the frequency dependency of the load where $\frac{753}{50000} = \frac{R_{2040}}{62000}$, which results in $R_{2040} = 934$ MW. From Figure 64b) it can be observed that a higher level of regulatory strength lead to less frequency deviation as compared to Figure 64a).

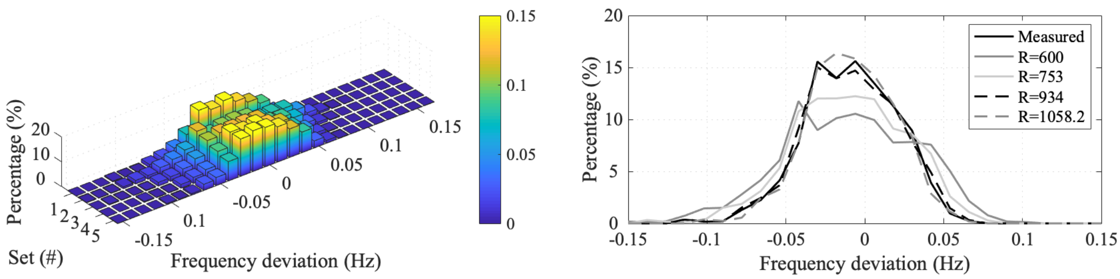

(a) Histograms describing the frequency data for ST2040.

(b) 2D-plot describing the frequency data for ST2040.

Figure 65: Histograms and 2D-plot describing the variation between the measured and simulated frequency data, for ST2040 based on ENTSO-E:s estimation for different regulating strengths.

To visualize the results from the different regulating strengths the scenarios are illustrated in Figure 65, where the measured data is used as a reference. Set 1 represents the measured

PMU-data and sets 2-5 represents 2040 for different regulatory strengths. Note that the area under the graphs do not represent the percentage distribution. As can be seen, for the same regulatory strength as 2019 the frequency deviations outside the normal band increases. If the regulatory strength is scaled to the online capacity the PoNB decrease, for $R = 934$ the $PoNB = 0.84\%$ compared to $R = 753$ the $PoNB = 1.3\%$.

5.5 Forecasting 2040ref, SvK

From the model of the hydro-fleet, a scenario for 2040ref can be estimated based on scenario data from SvK. SvK has production data estimates for 2040ref, therefore it is not necessary to scale the current installed capacity from ENTSO-E transparency platform. The inertia estimation is based purely on SvKs production data and the estimate for 2040ref. The specific hour analyzed is 10-11 23/3-2019, where the production data from the hour is used in the inertia estimation from the transparency platform. To be more specific about the 2040 estimation the date of the measured PMU-data is used, i.e. the hour 10-11 23/3-2040 for weather year 1. In Appendix A wind power production data from two different wind power facilities are presented. Thus, the time interval 10.00-11.00 23/3-2019 is selected for a higher wind power penetration scenario. The PMU data utilized is also presented in Appendix A from the selected hour. Note that the estimation is based on an hourly estimation and not a mean value for the year. From an inertia estimation of 2040ref for the evaluated hour $M = 5.36$ s and $D = 0.25$ pu as compared to 2019 where $M = 7.02$ s and $D = 0.40$ pu. The load disturbance is generated for the stronger grid condition from the measured PMU-data 23/3-2019 and is run in the regular grid model under weaker grid conditions, i.e. for 2040ref.

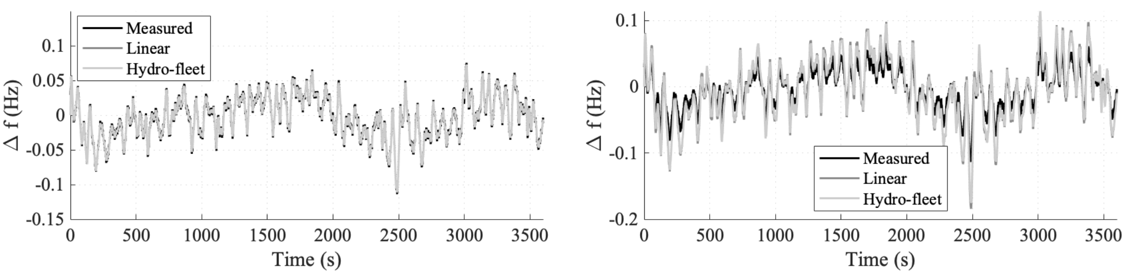

(a) Frequency data based on the 2019 SvK production data.

(b) Frequency data based on the 2040ref SvK production data estimate.

Figure 66: Frequency describing the variation between the measured and simulated frequency data, for 2019 and 2040ref based on SvKs estimation for weather year 1.

The resulting frequency from the 2040ref scenario is presented in Figure 66. Here, it can be seen that the frequency of the hydro-fleet estimation starts to deviate from the measured data. The PoNB for the particular hour examined is $PoNB_{2019} = 0.4\%$ for the 2019 frequency data and $PoNB_{2040ref} = 5.0\%$ for the 2040ref estimate. From the wind power production data in Appendix A the time interval 09.00-10.00 22/3-2019 is selected for a lower wind power penetration comparison. The scenario gives an inertia estimate for the 2040ref scenario of $M = 5.81$ s, $D = 0.25$ pu, $E_k = 233$ GWs and $S = 80$ GVA. The PoNB for the lower wind scenario is 3.0% as compared to 5.0% for the higher wind condition scenario for weather year 1. Thus, the estimation with higher wind power penetration shows a lowered inertia and a higher PoNB as compared to the estimation with lower wind in the generation mix.

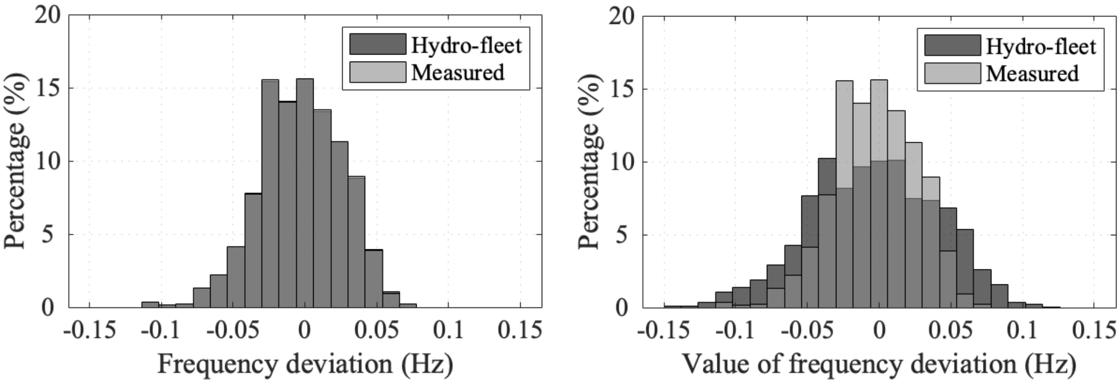

(a) Histogram based on the 2019 SvK production data.

(b) Histogram based on the 2040ref SvK production data.

Figure 67: Histograms; evaluating the variation between the measured and simulated frequency data, for 2019 and 2040ref based on SvKs estimations for weather year 1.

The deviation in frequency is more visible in Figure 67, where histograms illustrate the frequency deviations, comparing 2019 to 2040ref. As can be seen the frequency deviates more from the measured frequency profile, since there is less inertia present in the system. Note that the span is more outside the normal operational conditions then for the ENTSO-E scenario. The same method is utilized for the 2040high and 2040low scenarios, where the inertia estimation is calculated from the production data.

Table 18: Inertia estimations for the reference case 2040 along with the higher and lower estimations.

Year	M	%	D	%	E_k	%	S_b	%	PoNB	%
190323	7.03	-	0.4	-	177	-	50	-	0.004	-
2040low	5.19	0.97	0.28	1.12	185	0.87	71	0.9	0.024	0.47
2040ref	5.36	1.0	0.25	1.0	212	1.0	79	1.0	0.05	1.0
2040high	4.92	0.92	0.25	1.0	199	0.94	81	1.03	0.055	1.11

The higher and lower scenarios are presented in Appendix B and the 2040 scenario cases are summarized in Table 18. The 2040ref is used as a reference for the higher and lower estimations, where it can be seen that there are rather small variations between the different scenarios for the inertia M and the load frequency dependency D. The kinetic energy of the system, the online capacity and PoNB on the other hand vary quite much.

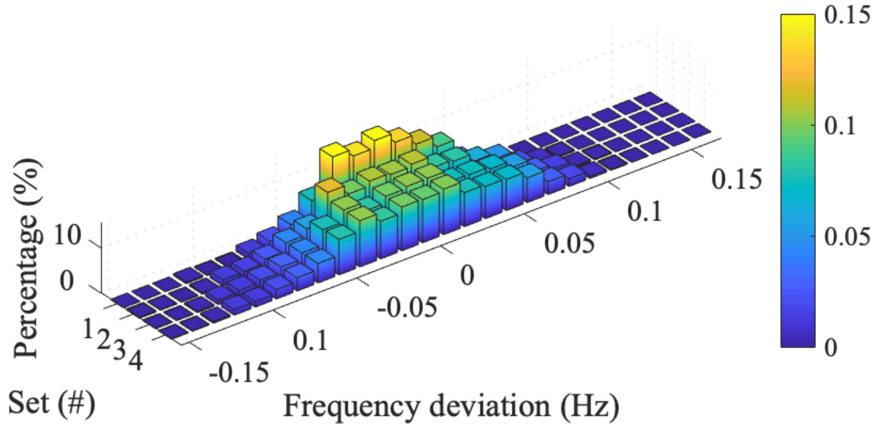

Figure 68: Histograms describing the variation between the measured and simulated frequency data, for 2019, 2040low, 2040ref and 2040high based on SvKs estimations for weather year 1.

To visualize the results from Table 18 the histograms from the scenarios are illustrated in Figure 68, where the 2019 estimation is used as a reference. Set 1 represents 2019 and sets 2-4 represents 2040low, 2040ref and 2040high, respectively. As can be seen, for all three estimations the frequency deviates more from the mean and the variations are higher due to the lower inertia condition.

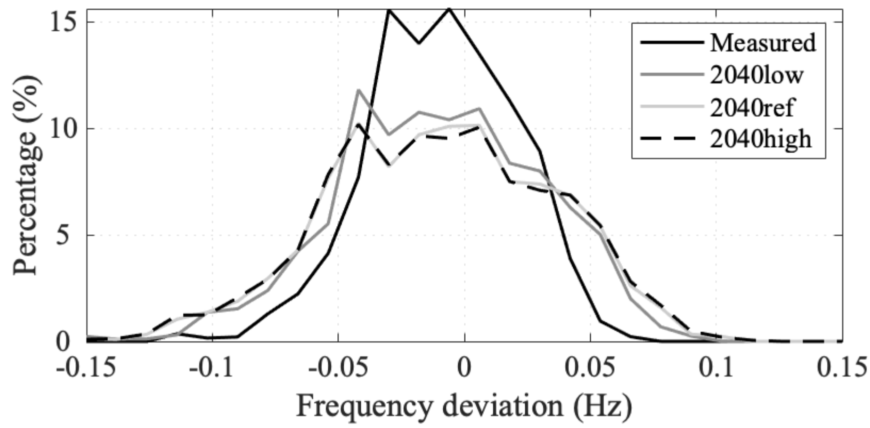

Figure 69: 2D-plot describing the variation between the measured and simulated frequency data for 2019, 2040low, 2040ref and 2040high based on SvKs estimations for weather year 1.

The histograms are represented in Figure 69 in 2D to more easily distinguish between the cases. A wider curve signifies a worsened frequency quality. From the 2D representation the variations between the different 2040 scenarios can be distinguished. The frequency deviation outside the normal band is higher for the 2040high scenario and lower for the 2040low scenario. The deviation outside the normal band is $PoNB_{2040low} = 2.4\%$, $PoNB_{2040ref} = 5.0\%$ and $PoNB_{2040high} = 5.5\%$ As can be expected, the 2040high scenario has a lower peak than the 2040low scenario and also deviates more from the mean.

5.5.1 Regulating strength

Since the regulating strength is a crucial factor in for the regulatory reserve products, the sensitivity for the parameter is evaluated for the estimated frequency data. The regulating strength of $R = 753$ MW was used as a reference and $R = 600$ MW, $R = 1058.2$ MW for a lower and upper value. The lowest value is the amount of FCR-N for 2019 and the higher value is based on the reasoning from section 3.6.1.

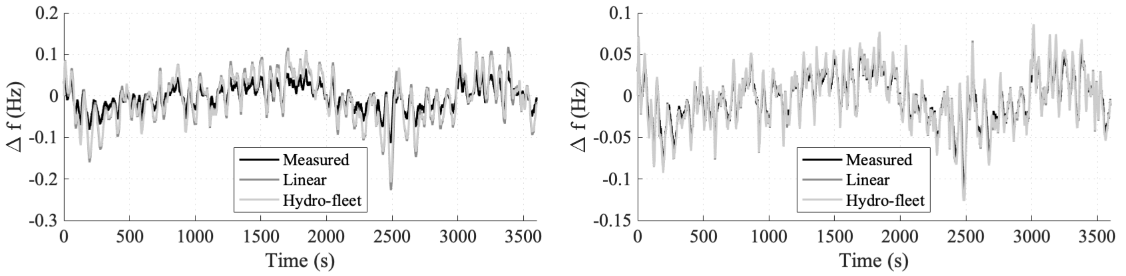

(a) Frequency data based on the 2040ref estimate for $R = 600$ MW.

(b) Frequency data based on the 2040ref estimate for $R = 1058.2$ MW.

Figure 70: Frequency describing the variation between the measured and simulated frequency data, for 2040ref based on SvKs estimation for weather year 1 for different regulating strengths.

The estimated frequency data for the different regulating strengths are illustrated in Figure 70. As can be seen the frequency deviations decrease for the higher regulatory strength. From the relationship between the regulatory strength and the kinetic energy (3.3) the regulatory strength for 2040 can be approximated, neglecting the frequency dependency of the load where $\frac{753}{50000} = \frac{R_{2040}}{79000}$, which results in $R_{2040} = 1190$ MW. From Figure 70b) it can be observed that a higher level of regulatory strength lead to less frequency deviation as compared to Figure 70a).

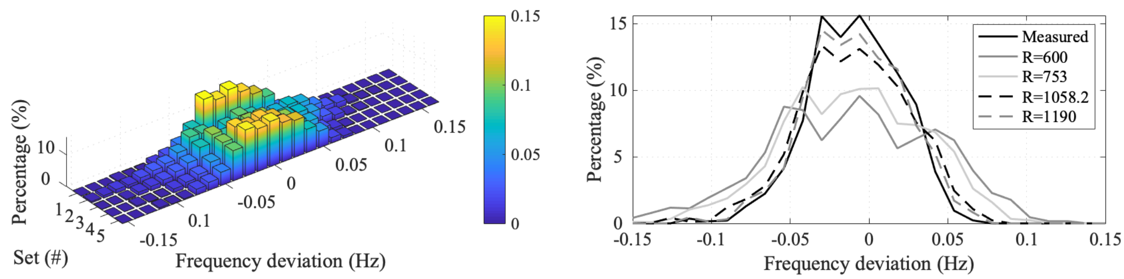

(a) Histograms describing the frequency data for 2040ref.

(b) 2D-plot describing the frequency data for 2040ref.

Figure 71: Histograms and 2D-plot describing the variation between the measured and simulated frequency data, for 2040ref based on SvKs estimations for weather year 1 for different regulating strengths.

To visualize the results from the frequency data the scenarios are illustrated in Figure 71, where the measured data is used as a reference. Set 1 represents the measured PMU-data and sets 2-5 represents 2040ref for $R = 600, R = 753$, $R = 1058.2$ and $R = 1190$ MW, respectively. As can be seen, for all four estimations the frequency deviates more from the mean and the variations are higher due to the lower inertia condition. In Figure 71b) the histograms are represented in 2D to more easily distinguish between the cases. As can be seen, for the same regulatory strength as 2019 the frequency deviations outside the normal band increases. If the regulatory strength is scaled to the online capacity the PoNB decrease, for $R = 1190$ the $PoNB = 1.0\%$ compared to $R = 753$ the $PoNB = 5.0\%$.

5.5.2 Weather year sensitivity analysis

To evaluate the sensitivity based on weather year 1 additional data-sets are run, weather years 1-5. The weather years are dependant on different temperature, weather conditions and inflow of water to hydro power reservoirs.

Table 19: Inertia estimations for the reference case 2040ref for 5 distinct weather years.

Year	Weather	M	%	D	%	E_k	%	S_b	%	PoNB	%
190323	1-5	7.03	-	0.4	-	177	-	50	-	0.004	-
2040	1	5.36	1.0	0.25	1.0	212	1.0	79	1.0	0.050	1.0
2040	2	4.27	0.8	0.26	1.04	162	0.76	76	0.96	0.039	0.79
2040	3	5.03	0.94	0.28	1.12	181	0.85	72	0.91	0.027	0.54
2040	4	5.38	1.0	0.34	1.36	159	0.75	59	0.75	0.011	0.23
2040	5	4.83	0.9	0.31	1.24	154	0.73	64	0.81	0.013	0.25
Average	1-5	4.98	0.93	0.29	1.15	174	0.82	70	0.89	0.028	0.56

The spread of the inertia constant, damping, kinetic energy, capacity and PoNB for the different weather years are presented in Table 19. The first weather year estimation is considered a reference for the other scenarios, to more clearly display the variation between the estimations. As can be seen the variation in the system inertia M is around 7% and the load frequency dependancy D is averaging a 15% spread. The kinetic energy vary roughly 18% and the spread is quite varied and the capacity has a spread of about 10%. The PoNB has increased significantly compared to the measured value, from 0.4% outside the normal band to an average of 2.8%, with high variations depending on the weather year.

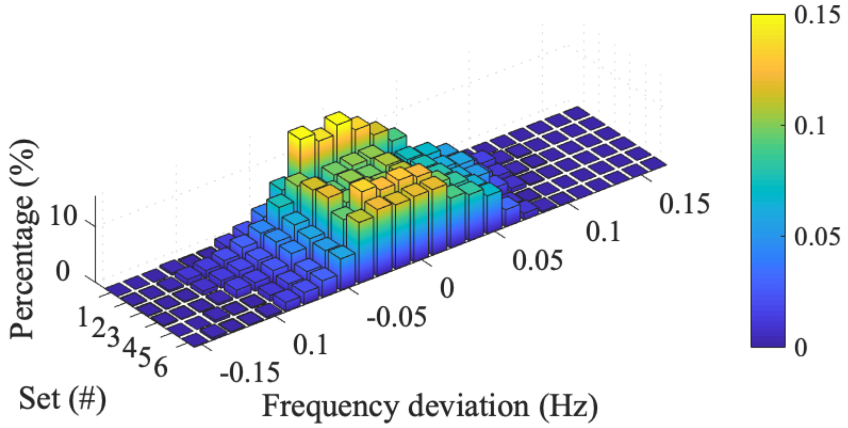

Figure 72: Histograms describing the variation between the measured and simulated frequency data for 2019 and 2040ref based on SvKs estimations for 5 distinct weather years.

The results from Table 19 are visualized in Figure 72, where the measured data is used as a reference. Set 1 represents 2019 and sets 2-6 represents five different weather years 1-5, respectively. As can be seen, for all five estimations the frequency deviates more from the mean and the variations are higher due to the lower inertia condition.

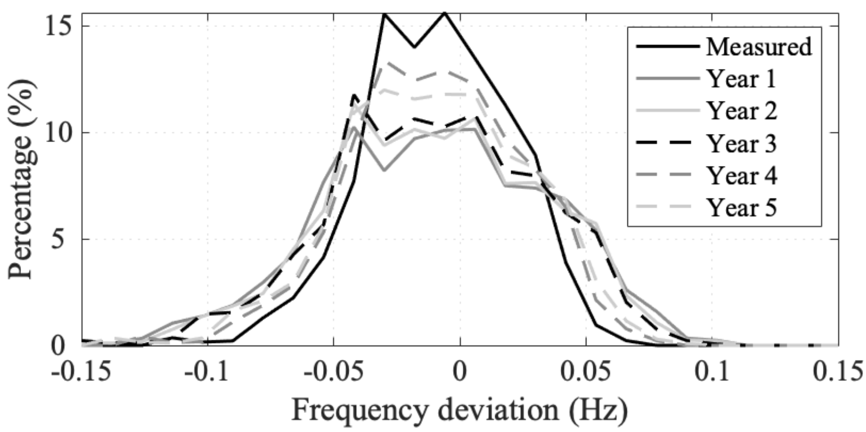

Figure 73: 2D-plot describing the variation between the measured and simulated frequency data 2040ref based on SvKs estimations for 5 distinct weather year.

The histograms are represented in Figure 73 in 2D to more easily distinguish between the cases. From the 2D representation the variations between the different 2040 weather years can be seen. The frequency deviation outside the normal band is highest for weather year 1 scenario and lowest for the weather year 4 scenario. The deviation outside the normal band is $PoNB_{wy1} = 5.0\%$ for the highest deviation and $PoNB_{wy4} = 1.1\%$ for the lowest deviation outside the normal band. As can be observed the weather conditions, temperature and inflow of water considerably affect the estimations.

5.5.3 Yearly estimations

Since the hourly representation of the frequency variation is heavily influenced by the specific weather condition and generation mix during the day, 23/3-2019, an analysis of the yearly mean values during the estimated scenarios is evaluated.

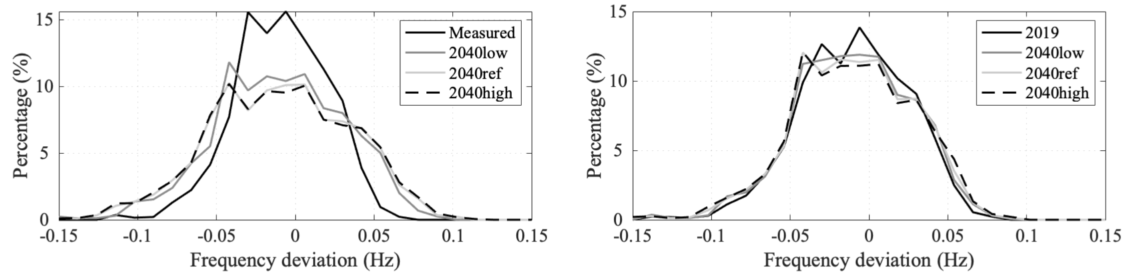

(a) Frequency for 2040ref for the hourly estimation.

(b) Frequency data 2040ref for the yearly estimation.

Figure 74: 2D-plot describing the variation between the measured and simulated frequency, hourly and yearly, for 2040ref based on SvKs estimations for weather year 1.

The hourly and yearly representation for the different reference scenarios are presented in Figure 74. As can be seen the variation is higher for the hourly estimation than the yearly estimation for the different scenarios. The 2019 frequency is also lowered in Figure 74b) as compared to 74a) since it represents the yearly average for 2019. The deviations outside the normal band is $PoNB_{2040ref,h} = 5.0\%$ for the hourly estimation as compared to $PoNB_{2040ref,y} = 1.5\%$ for the yearly average. The PoNB for the higher and lower estimations are presented in Appendix A. The weather condition sensitivity is investigated to evaluate how different weather years influence the estimation.

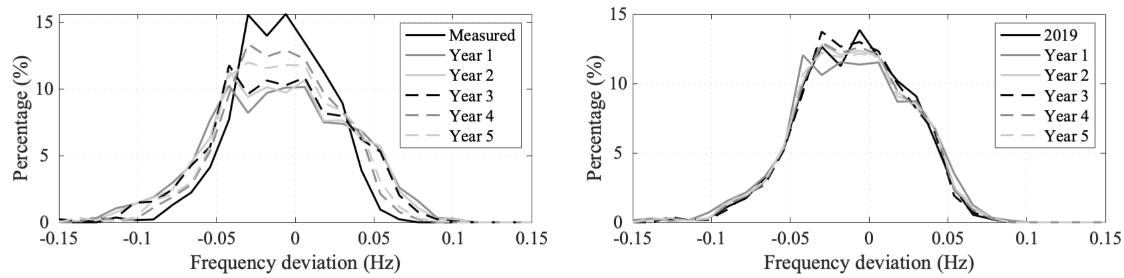

(a) Frequency for 2040ref for the hourly estimation.

(b) Frequency for 2040ref for the yearly estimation.

Figure 75: 2D-plot describing the variation between the measured and simulated frequency, hourly and yearly, for 2040ref based on SvKs estimations for weather years 1-5.

The hourly and yearly representation for the different weather years are presented in Figure 75. As can be seen the variation is higher for the hourly estimation than the yearly estimation for the different scenarios. The estimation for weather year 3 goes above the 2019 average, this could be explained by that the 2019 estimation is based on the weather year 1 conditions. For the hourly representation the deviation outside the normal band is $PoNB_{wy1,h} = 5.0\%$ for the highest deviation and $PoNB_{wy4,h} = 1.1\%$ for the lowest deviation outside the normal band. For the yearly representation the deviation outside the normal band is $PoNB_{wy1,y} = 1.5\%$ for the highest deviation and $PoNB_{wy4,y} = 1.1\%$ for the lowest deviation outside the normal band. The PoNB for the other weather year scenarios are presented in Appendix A.

5.5.4 Conclusion scenario 2040

In general, the frequency deviates more from the measured frequency, since there is less inertia present in the system for all estimations of 2040ref, the different higher and lower estimations and distinct weather years. The simulated frequency is mostly still in the span for normal operational conditions but there is an increase in the PoNB, which indicates that the deviations will increase further outside the normal band. The measured frequency had a $PoNB = 0.4\%$, the hourly lower estimation had $PoNB_{2040low} = 2.4\%$, the reference $PoNB_{2040ref} = 5.0\%$ and the higher estimation had $PoNB_{2040high} = 5.5\%$, indicating a trend that could be expected. This relation is also seen in the 2D-plot in Figure 69, where 2040high has a higher frequency deviation than 2040low. From the weather year analysis it can be observed in Figure 73 that the estimation of 2040ref is considerably influenced by the seasonal variations and the weather, with a deviation of 1.1-5.0% PoNB between the different weather years. The yearly average estimation showed a lower variation outside the normal band with a span of 1.1-1.5% PoNB. A sensitivity analysis of the regulatory strength for the 2040ref scenario showed that the relationship R/E_k as described in (3.3) seemed like a good prediction of how the reserve product should be adjusted to accommodate a lowered inertia condition. The scenario estimate based on the ENTSO-E installed capacity shows less deviation in the overall frequency variations than the scenarios based on the SvK production data.

6 Discussion

In this thesis, the models utilized are approximate representations and simplified as compared to a real system. Therefore, the level of detail is relevant to discuss, since the simplifications determine the behavior of the hydro-fleet system. The grid model considered is a lumped and linearised power system, which describes one rotating mass. The representations of the turbine and penstocks are also linear, disregarding the dynamics of the waterways along with non-compressible water. The runner regulator and the GVs have non-linearities introduced with backlash and limitations. The hydro-fleet model utilize PI-control with permanent droop, linearised turbine and waterways, along with a lumped power system model. These design decisions are relatively well used in hydro-modelling concerning for frequency regulatory action. Since the models are quite applied, one idea could be to utilize different E_p-settings for the Swedish turbines as suggested in [2], where the PI-controller is scaled to the droop of the governor for a less static system. An additional consideration for the model is the Pelton turbine control system, where the PI-control is based on an approximation for the workings of the needle and deflector in the turbine. Therefore, for a more accurate model, these element would also need to be considered.

The sensitivity analysis for the regulating strength was performed to evaluate how a different amount of FCR-N reserve power would affect the frequency for the 2040 scenario. The idea was to utilize the relationship between the regulating strength and the kinetic energy (3.3) to calculate how much of an increase or decrease the regulatory strength was required from the inertia estimation. Since the relationship between the current regulatory strength and the kinetic energy of the system in 2019 was known and the kinetic energy for the 2040 scenarios could be estimated, the corresponding regulatory strength could be calculated. The new regulatory strength would then mitigate or compensate for the frequency deviations introduced by the lower inertia conditions. The results suggest that the relation between the regulatory strength and the kinetic energy give an acceptable prediction of how the FCR-N should be altered to compensate the lowered power system inertia. However, because of the problems with instability issues and the coordination with additional regulating reserves, FCR-D etc, additional work is suggested to clarify the relationship between the regulatory strength and kinetic energy while accounting for the imbalance issues that may arise from a high regulatory strength.

To gain a better estimation of the net load disturbances for 2040, additional wind power production would have to be integrated in the hydro-fleet model. The current estimation is performed during a higher and lower wind power penetration level in the Nordic power system. However, the wind power generation in 2019 in about 20% of the total generation in the NPS, as compared to about 40% for an estimated installed capacity 2040 [24]. This means that the constitution of the generation mix in 2040 for a day with high wind penetration would differ quite much from the frequency data used for the estimation in this project. Since the current net load disturbance is constitutive of the sum of the different generation types, it is not that intuitive to introduce additional wind power generation to the current generation mix. Therefore an hour with higher wind generation was considered in this project as an acceptable alternative solution.

7 Conclusion

The main conclusion from this thesis is an estimation of the spread of the frequency deviations for distinct 2040 scenarios. Different scenario estimations for 2040 is taken into account, from SvK and ENTSO-E, along with distinct weather years from the estimated production data. A hydro-fleet grid inverse model of the power system has been developed to generate an approximate net load variation corresponding to the measured frequency data. Then different inertia estimations matching the distinct scenarios for 2040 have been evaluated using the net load variation to estimate the future frequency quality of the NPS. The kinetic energy of the NPS was estimated for the 2040ref scenario to a mean value of 175 GWs in 2040, as compared to 223 GWs in 2019. The estimation was based on the reference scenario 2040ref, using estimated production data from LMA2018, which is the common reference scenario for the Nordic TSOs in their system operator market models for 2040.

The estimation of the 2040low, 2040ref and 2040high scenarios shows an overall increase of frequency deviation outside the normal band, which means that the frequency quality is worsened. The hourly estimations for 23/3-2019 to 23/3-2040 shows a higher deviation from the nominal, where $PoNB_{2040ref} = 5.0\%$ and the high and low estimations $PoNB_{2040high} = 5.5\%$, $PoNB_{2040low} = 2.4\%$ respectively. The weather year sensitivity analysis shows that the inflow of water, weather and temperature during the distinct years significantly influence the estimation, with a spread of around 1.1-5.0% for 2040ref which influence the higher and lower estimations. The yearly estimations shows less variation in the estimates for the different scenarios and for the weather years sensitivity analysis, where $PoNB_{2040ref} = 1.5\%$ and the high and low estimations $PoNB_{2040high} = 1.7\%$, $PoNB_{2040low} = 1.3\%$ respectively. The weather year sensitivity analysis shows a lesser variation during the distinct years influencing the estimation, with a spread of around 1.1-1.5%.

From a sensitivity analysis of the regulating strength for the 2040ref scenario it is observed that the relationship between the kinetic energy and the regulatory strength give an acceptable indication of how much regulatory strength is needed to accommodate a decreased inertia in NPS. However, since the hydro-fleet model encompass the FCR-N, additional work is required to account for instability issues that may arise from a too high regulatory strength and coordination with other frequency reserve products in the Nordic region.

8 Future work

- FCR-N / FCR-D interaction
  Since this thesis work has mostly focused on the FCR-N aspect of power system operation, a follow-up would be to integrate the FCR-D product in the model so the model encompass the entire frequency containment reserve. SvK has investigated the interaction between the FCR products in [14], but an extension would be to include the transition for the hydro-fleet model.

- FFR product contribution - e.g. synthetic inertia support
  FFR is a new product or concept from SvK, which aims to help balance out a weaker grid condition, similarly to the introduction of the aFRR. This is also an interesting aspect, to incorporate the new product as complement to the primary frequency response for overall better frequency quality.

- aFRR / mFRR co-ordination
  The frequency replacement reserve is also an important aspect to consider, for rebalancing of larger faults and also to account for the hourly changes in the frequency reserve products.

- Thermal power contribution Finland + DK2
  Since the report only concern hydro power in the Nordic region, another aspect would be to introduce thermal power plants, since both Finland and Denmark utilize these to some extent for regulatory interactions. Currently Denmark is not incorporated in the model apart from the inertia estimation, since there is no hydro generating units in the country. Thus, complementing the hydro representation with thermal power plants would give a more complete system overview.

- CHP-plant for FCR control interactions
  This is connected to the previous point, with thermal power integration. Since many Swedish CHP-plants only aim to produce the desired thermal output, the electrical regulatory aspect is often neglected. CHP-plants can be utilized for frequency regulatory action and may play a more integral role in a future system, with a more unified heat and electricity sector.

- Increased wind power penetration levels in the generation mix
  For a more accurate representation for the frequency quality estimation for 2040, additional wind power generation would have to be introduced to the generation mix. Because the wind power penetration is 20% of the total installed capacity in 2019 in the Nordic region additional wind would have to be introduced to the generation mix. The estimated wind power penetration levels for 2040 is 40% for the NPS, therefore it is feasible to assume that there would be a further increase in the frequency variations.

- Revisit Pelton turbine modelling
  The Pelton turbine model is based on an approximation of a PI-controller established by measurements on Pelton turbines in Norway. Since the turbine is constituent of a needle and deflector, rather than the layout presented for the Francis and Kaplan models an improved model of the turbine would present a more detailed hydro-fleet model.

References

[1] W. Yang, P. Norrlund, and J. Yang, "Analysis on regulation strategies for extending service life of hydropower turbines," in *IOP Conference Series: Earth and Environmental Science*, 2016.

[2] W. Yang, P. Norrlund, L. Saarinen, J. Yang, W. Zeng, and U. Lundin, "Wear Reduction for Hydropower Turbines Considering Frequency Quality of Power Systems: A Study on Controller Filters," *IEEE Transactions on Power Systems*, vol. 32, no. 2, pp. 1191–1201, 2017.

[3] L. Saarinen, P. Norrlund, W. Yang, and U. Lundin, "Allocation of Frequency Control Reserves and its Impact on Wear on a Hydropower Fleet," *IEEE Transactions on Power Systems*, vol. 33, no. 1, pp. 430–439, 2017.

[4] R. M. Johnson, J. H. Chow, and M. V. Dillon, "Pelton turbine deflector overspeed control for a small power system," *IEEE Transactions on Power Systems*, vol. 19, no. 2, 2004.

[5] R. M. Johnson, J. H. Chow, and M. V. Dillon, "Pelton Turbine Needle Control Model Development, Validation, and Governor Designs," *Journal of Dynamic Systems, Measurement, and Control*, 2012.

[6] L. Wang, J. Wang, J. Zhao, D. Liu, W. Sun, Y. Zhao, X. Qi, G. Chen, and T. Zhao, "Governor tuning and digital deflector control of Pelton turbine with multiple needles for power system studies," *IET Generation, Transmission & Distribution*, 2017.

[7] M. Persson and P. Chen, "Kinetic energy estimation in the nordic system," in *20th Power Systems Computation Conference, PSCC 2018*, 2018.

[8] H. Kuisti, M .Lahtinen, M. Nilsson, K. Eketorp, E. Ørum, D. Whitley, A. Slotsvik, and A. Jansson, "NAG - Frequency Quality Report," Tech. Rep., 2015.

[9] J. Machowski, J. Bialek, and J. Bumby, *Power System Dynamics : Stability and Control*, 2nd ed. John Wiley & Sons, Incorporated, 2008.

[10] D. Karlsson and A. Nordling, *Svängmassa i elsystemet En underlagsstudie.* Stockholm: Kungl. Ingenjörsvetenskapsakademien (IVA), 2016. [Online]. Available: www.iva.se

[11] P. Kundur, *Power System Stability and Control.* New York: McGraw-Hill, 1994.

[12] Svenska Kraftnät, "Årsredovisning 2018," Tech. Rep., 2018.

[13] M. Kuivaniemi, N. Modig, and R. Eriksson, "FCR-D design of requirements," Tech. Rep., 2017.

[14] E. Agneholm, S. A. Meybodi, M. Kuivaniemi, P. Ruokolainen, J. N. Ødegård, N. Modig, and R. Eriksson, "FCR-D design of requirements - Phase 2," ENTSO-E, Tech. Rep., 2019. [Online]. Available: www.entsoe.eu

[15] E. Agneholm and E. Jansson Alexander, "FCP Project Summary report," Tech. Rep., 2017. [Online]. Available: https://www.svk.se/siteassets/om-oss/nyheter/nordic-common-project-for-review-of-primary-reserve-requirements--finalized-phase-1/1---fcp-project-summary-report.pdf

[16] Norconsult, “Nordic Grid - FNR Frequency Containment,” Tech. Rep., 2016.

[17] R. Eriksson, N. Modig, and A. Westberg, “FCR-N Design of Requirements,” Tech. Rep., 2017. [Online]. Available: www.entsoe.eu

[18] E. Ørum, L. Haarla, M. Kuivaniemi, M. Laasonen, A. Jerkø, I. Stenkløv, F. Wik, K. Elkington, R. Eriksson, N. Modig, and P. Schavemaker, “Future System Inertia 2,” Tech. Rep. [Online]. Available: www.entsoe.eu

[19] M. Persson, “Frequency Response by Wind Farms in Power Systems with High Wind Power Penetration,” Ph.D. dissertation, Chalmers University of Technology, 2017. [Online]. Available: https://research.chalmers.se/publication/250313

[20] ENTSO-E, “ENTSO-E transparency platform,” 2017. [Online]. Available: https://transparency.entsoe.eu

[21] ——, “Country Level Results - Scenario Report,” Tech. Rep., 2018.

[22] ——, “TYNDP 2018 Scenario Report,” Tech. Rep., 2018.

[23] ——, “Annex I - Country Level Results,” Tech. Rep., 2018.

[24] Kristin Brunge, Jonas Alterbeck, Erik Böhlmark, Emilia Helander, Erik Hellström, Anders Nilsberth, and Mira Rosengren Keijser, “LÅNGSIKTIG MARKNADSANALYS 2018 - Långsiktsscenarier för elsystemets utveckling fram till år 2040,” Svenska Kraftnät, Stockholm, Tech. Rep., 2019. [Online]. Available: https://www.svk.se/siteassets/om-oss/rapporter/2019/langsiktig-marknadsanalys-2018.pdf?_t_id=1B2M2Y8AsgTpgAmY7PhCfg==&_t_q=långsiktig+marknadsanalys&_t_tags=language:sv,siteid:40c776fe-7e5c-4838-841c-63d91e5a03c9&_t_ip=192.121.1.150&_t_hit.id=SVK_WebUI_Mo

[25] IEEE Std 1207-2011, “IEEE Guide for the Application of Turbine Governing Systems for Hydroelectric Generating Units,” IEEE, NY, Tech. Rep., 2011.

[26] G. Boyle, *Renewable Energy*, 2nd ed. Oxford, UK: Oxford University Press, 2003. [Online]. Available: http://oro.open.ac.uk/id/eprint/3044

[27] T. Bambaravanage, A. Rodrigo, and S. Kumarawadu, *Power Systems Modeling, Simulation, and Control of a Medium-Scale Power System.* Singapore: Springer, 2018. [Online]. Available: http://www.springer.com/series/4622

[28] K. J. Åström and T. Hägglund, *Advanced PID control.* ISA, 2006. [Online]. Available: https://app.knovel.com/hotlink/toc/id:kpAPIDC001/advanced-pid-control/advanced-pid-control

[29] L. Saarinen, “The Frequency of the Frequency. On hydropower and grid frequency control,” Ph.D. dissertation, Uppsala University, 2017. [Online]. Available: http://urn.kb.se/resolve?urn=urn:nbn:se:uu:diva-308441

[30] L. Saarinen, P. Norrlund, W. Yang, and U. Lundin, “Linear synthetic inertia for improved frequency quality and reduced hydropower wear and tear,” *International Journal of Electrical Power and Energy Systems*, vol. 98, pp. 488–495, 6 2018.

[31] A. Stoorvogel, *The H control problem: A state space approach.* Ann Arbor: University of Michigan, USA, 2 2000.

[32] F. R. Schleif and R. R. Angell, “Governor Tests by Simulated Isolation of Hydraulic Turbine Units,” *IEEE Transactions on Power Apparatus and Systems*, 1968.

[33] J. Woodward, “Hydraulic-turbine transfer function for use in governing studies,” *Proceedings of the Institution of Electrical Engineers*, vol. 115, no. 3, pp. 424–426, 1968.

[34] D. G. Ramey and J. W. Skooglund, “Detailed Hydrogovernor Representation for System Stability Studies,” *IEEE Transactions on Power Apparatus and Systems*, 1970.

[35] L. Ekmarker, “Frequency control - Optimal distribution of FCR-N in real-time,” Tech. Rep., 2014. [Online]. Available: http://www.teknat.uu.se/student

[36] L. Saarinen, P. Norrlund, and U. Lundin, “Field Measurements and System Identification of Three Frequency Controlling Hydropower Plants,” *IEEE Transactions on Energy Conversion*, vol. 30, no. 3, pp. 1061–1068, 2015.

[37] Working Group on Prime Mover and Energy Supply Models for System Dynamic Performance Studies, “Hydraulic turbine and turbine control models for system dynamic studies,” Tech. Rep. 1, 1992.

[38] Statnett, “Funksjonskrav i kraftsystemet,” Tech. Rep., 2012.

[39] W. Yang, P. Norrlund, C. Y. Chung, J. Yang, and U. Lundin, “Eigen-analysis of hydraulic-mechanical-electrical coupling mechanism for small signal stability of hydropower plant,” *Renewable Energy*, vol. 115, pp. 1014–1025, 2018.

[40] IEC, “Draft IEC 61970: Energy Management System Application Program Interface (EMS-API) - Part 302: Common Information Model (CIM) for Dynamics Specification,” 2014.

[41] M. Brezovec, I. Kuzle, and T. Tomisa, “Nonlinear digital simulation model of hydroelectric power unit with Kaplan turbine,” *IEEE Transactions on Energy Conversion*, vol. 21, no. 1, pp. 235–241, 3 2006.

[42] G. Styrbro, B. Agerholm, T. Toivonen, O. Håkon Hoelsæter, and J. Magnusson, “Nordisk Regelsamling 2004,” Tech. Rep., 2004. [Online]. Available: http://pfbach.dk/firma_pfb/historien/data_files/Nordisk_regelsamling_2004.pdf

[43] L. Saarinen, P. Norrlund, U. Lundin, E. Agneholm, and A. Westberg, “Full-scale test and modelling of the frequency control dynamics of the Nordic power system,” in *IEEE Power and Energy Society General Meeting*, vol. 2016-November. IEEE Computer Society, 11 2016.

[44] Statens energimyndighet, “Vad avgör ett vattenkraftverks betydelse för elsystemet - Underlag till nationell strategi för åtgärder inom vattenkraften,” Tech. Rep., 2014. [Online]. Available: https://www.energimyndigheten.se/globalassets/nyheter/2014/vad-avgor-ett-vattenkraftverks-betydelse-for-elsystemet.pdf

[45] Svenska Kraftnät, “Regler för upphandling och rapportering av FCR-N och FCR-D - Produktion,” Tech. Rep., 2018. [Online]. Available: www.ediel.se/Portal.

[46] Fingrid, “Grid Code Specifications for Power Generating Facilities VJV2018,” Tech. Rep., 2018.

[47] Nordic Energy Regulators, “Statistical Summary of the Nordic Energy Market 2014,” Tech. Rep., 2014. [Online]. Available: http://www.nordicenergyregulators.org/wp-content/uploads/2015/03/Main-developments-and-trends1.pdf

[48] E. Ørum, M. Kuivaniemi, M. Laasonen, A. I. Bruseth, E. A. Jansson, A. Danell, K. Elkington, and N. Modig, “Future system inertia,” ENTSO-E, Tech. Rep., 2016. [Online]. Available: www.entsoe.eu

[49] G. Le Dous, *Voltage stability in power systems: load modelling based on 130kV field measurements*, no: 324. ed., ser. Technical report L School of Electrical and C. U. o. T. Computer Engineering, Eds. Department of Electric Power Engineering, Chalmers University of Technology, 1999.

Appendix

A Model parameters and raw data

Tables

Table 20: Installed capacity of different energy sources for Norway, for distinct scenarios ranging from 2020 - 2040 [21].

Production type (MW)	2020	ST2040	DG2040	GCA2040
Hydro	35000	37000	37000	37000
Wind	3000	5000	6500	11000
Solar	0	0	6500	2500
Thermal and other	600	1100	0	0
Total	38600	43100	50000	50500

Table 21: Installed capacity of different energy sources for Finland, for distinct scenarios ranging from 2020 - 2040 [21].

Production type (MW)	2020	ST2040	DG2040	GCA2040
Hydro	3200	3200	3200	3200
Nuclear	2800	4000	4000	4000
Wind	2000	8000	8000	8000
Solar	0	2000	6000	6000
Thermal and other	9300	9000	6000	8400
Total	17300	26200	27200	29600

Table 22: Installed capacity of different energy sources for Denmark, for distinct scenarios ranging from 2020 - 2040 [21].

Production type (MW)	2020	ST2040	DG2040	GCA2040
Wind	7000	13000	12500	15000
Solar	1000	5000	7500	7500
Thermal and other	5000	3500	2500	2500
Total	13000	21500	22500	25000

Table 23: Measured values for time delays, constants and deadband for Kaplan (S2, S3) and Francis (S4, S5) turbine variants in Sweden [16].

Symbol	Description	S2	S3	S4	S5	Unit
$T_{del,Y}$	Servo valve delay	0.097	0.3	0.35	0.23	[s]
$T_{del,\alpha}$	Servo runner delay	0.41	0.4	-	-	[s]
BL_Y	Backlash servo valve	0.00029	0.0003	0.0003	0.0009	[pu]
BL_{gv}	Backlash guide vane	0.0004	0	0	0.0023	[pu]
BL_α	Backlash servo runner	0.00132	0.017	-	-	[pu]
T_Y	Time constant servo valve	0.25	0.2	0.2	0	[s]
T_α	Time constant servo runner	0.9	1	-	-	[s]
Y_0	Unit loading	0.75	0.77	0.67	0.71	[pu]
R_Y	Power alteration servo valve	0.79	0.6	1.23	1.14	[pu/pu]
R_α	Power alteration servo runner	0.37	0.4	-	-	[pu/pu]
T_w	Water time constant	1.7	1.6	0.74	1.1	[s]

Table 24: Average values for different backlash parameters throughout the turbines [16]. High Francis represents high-head and similarly Medium Francis describe low-to-medium head Francis turbines.

Symbol	Description	High Francis	Medium Francis	Kaplan	Pelton	Unit
BL_Y	Main servo valve	0.0003	0.0003	0.0003	-	[pu]
BL_{gv}	Guide vane stem	0.003	0.0012	0.0003	-	[pu]
BL_a	Runner servo valve	-	-	0.0006	-	[pu]
BL_{mo}	Linkage motion loss	0.0025	0.001	0.001	-	[pu]
BL_{tot}	Total backlash	0.006	0.0025	0.017	0.0005	[pu]

Table 25: Country-based installed capacity of the HPPs in the Nordic region in terms of the water time constant [14].

T_w, Water time constant [s]	Norway [MW]	Sweden [MW]	Finland [MW]
≤ 1.2	21429	7612	742
1.21-1.4	4204	2146	129
1.41-1.6	2347	1909	354
1.61-1.8	0	1275	49
1.81-2.0	0	1758	680
2.01-2.2	0	0	56

Table 26: Parameters specifically for the different turbine types [3, 16, 40].

Symbol	Description	Francis	Kaplan	Pelton	Unit
T_α	Time constant servo runner	-	1.3	-	[s]
T_w	Water time constant	1.4	1.6	0.4	[s]
R_y	Power alteration servo valve	1	0.5	1	[pu/pu]
R_α	Power alteration servo runner	0	0.5	0	[pu/pu]
U_o	Max gate opening velocity	0.011	0.011	0.016	[pu/s]
U_c	Max gate closing velocity	-0.011	-0.011	-0.016	[pu/s]
BL_Y	Backlash servo valve	0.003	0.0003	0.0005	[pu]
BL_{gv}	Backlash guide vane	0.0003	0.0003	-	[pu]
BL_α	Backlash servo runner	-	0.0006	-	[pu]

Table 27: Common parameter values for the turbine models [3, 16, 40].

Symbol	Description	Value	Unit
$T_{del,Y}$	Servo valve delay	0.3	[s]
$T_{del,\alpha}$	Servo runner delay	0.4	[s]
T_y	Actuator time constant	0.2	[s]
G_{max}	Maximum gate opening	1	[pu]
G_{min}	Minimum gate opening	0	[pu]
Y_0	Unit loading	0.8	[-]

Table 28: Transfer function coefficients for the different turbine types in the Nordic region.

	T_w	b_{01}	b_{11}	b_{21}	b_{31}	c_{01}	c_{11}	c_{21}	c_{31}	c_{41}
SE/FI_{Fr}	1.4	0	-1.12	0.53	0.42	0.83	5.86	8.06	0.45	0.0053
SE/FI_{Ka}	1.6	0	-1.28	0.46	0.42	0.95	6.48	8.09	0.45	0.0053
NO_{Fr}	1.4	0	-3.36	2.66	0.30	0.83	6.19	8.65	0.44	0.0038
NO_{Ka}	1.6	0	-3.84	2.62	0.30	0.95	6.86	8.68	0.44	0.0038
NO_{Pe}	0.4	0	-0.8	2.34	0.50	0.24	2.81	8.33	0.49	0.0063

Table 29: Percentage outside normal band (PoNB) for the hourly and yearly estimations of the 2040ref, 2040high and 2040low scenarios.

	2040low	2040ref	2040high	Unit
Hourly PoNB	2.4	5.0	5.5	%
Yearly PoNB	1.3	1.5	1.7	%

Table 30: Percentage outside normal band (PoNB) for the hourly and yearly estimations for five distinct weather years.

	Year 1	Year 2	Year 3	Year 4	Year 5	Unit
Hourly PoNB	5.0	4.0	2.7	1.1	1.3	%
Yearly PoNB	1.5	1.2	1.1	1.2	1.3	%

Raw data

To analyze the inertia estimations and different scenarios, PMU data is utilized in the report from Gothenburg in Sweden.

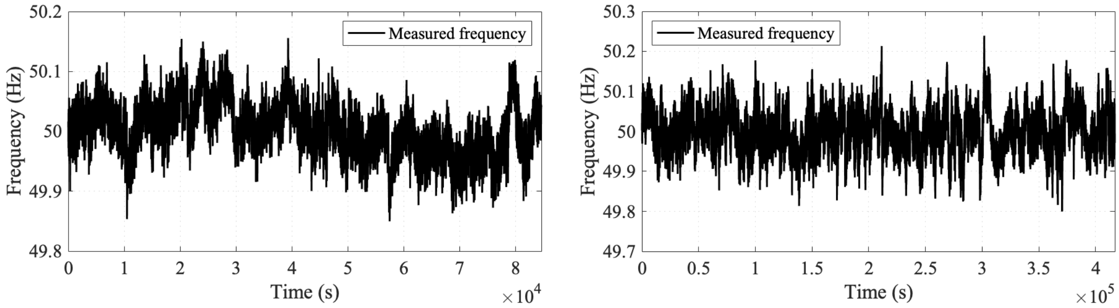

(a) Measured frequency data for the day 15/11-2018.

(b) Measured frequency data, between 21/3-2019 and 25/3-2019.

Figure 76: PMU frequency data from a day with normal wind strength, 15/11-2018 and a data-set with higher wind penetration 21/3-2019 to 25/3-2019.

The PMU data is illustrated in Figure 76, where Figure 76a) represents one day of data with normal weather conditions and Figure 76b) represents a five day period with higher wind power penetration levels. As can be seen the different PMU data sets differ in terms of events that are outside of the normal frequency band 50$\pm$0.1 Hz.

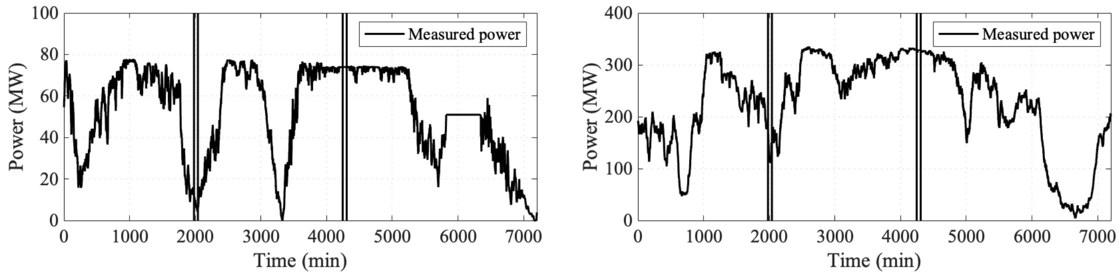

(a) Measured power data-set 1.

(b) Measured power data-set 2.

Figure 77: Unidentified and measured minute data from two wind power production facilities between 21/3-2019 and 25/3-2019.

Figure 77 represents unidentified and measured minute data from two wind power production facilities during a five day period. Figure 77a) and 77b) illustrates data sets from a smaller and larger wind power production facility, respectively. As can be seen the wind power production peaks around the intervals 1050-1250, 2500-3000 and 4000-5000 min. The interval used in the report is the hour between 4245 and 4305 min, which represent 10.00-11.00 23/03-2019 with high wind power penetration. As a comparison between a higher and lower wind power penetration scenario, the hour between 1980 and 2040 is selected, which represents 09.00-10.00 22/03-2019.

B Scenario estimations 2040

The two complementary scenarios to the reference scenario from LMA2018 are the high scenario 2040high and the low scenario 2040low. From the common reference scenario 2040ref the fuel price, emissions and electricity consumption have been varied produce the scenarios. The higher and lower scenarios 2040high and 2040low are estimated for weather year 1.

Scenario 2040high

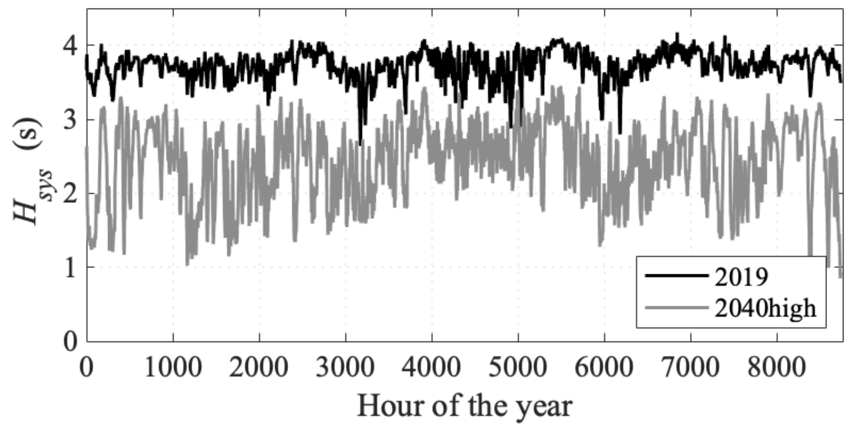

Figure 78: Power system inertia, $H_{sys-nordic}$ for 2019/2040high.

For the 2040high case the inertia estimation is presented in Figure 78. The values of $H_{sys-nordic}$ varies from 0.85 to 3.46, with a mean value of 2.42 s, as compared to the 2.64 s reference case.

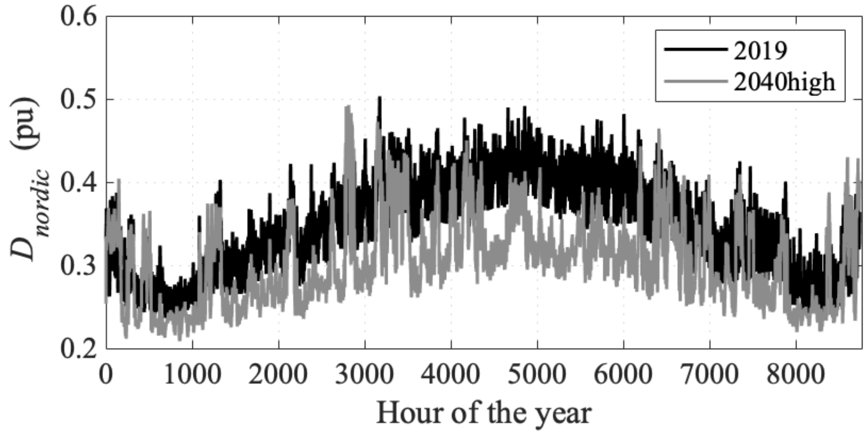

Figure 79: Power system frequency dependency, D_{nordic} for 2019/2040high.

The frequency dependency of the load for the 2019 scenario is presented in Figure 55. The values of D_{nordic} varies from 0.21 to 0.49, with a mean value of 0.30 pu, as compared to the 0.34 pu reference case.

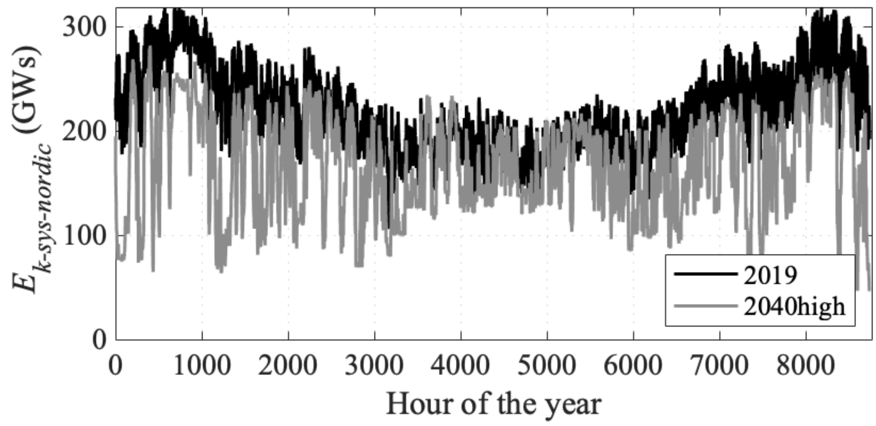

Figure 80: Power system kinetic energy, $E_{k-sys-nordic}$ for 2019/2040high.

The kinetic energy of the power system for the 2040high scenario is presented in Figure 80. As can be seen the kinetic energy peaks in December with 282 GWs and the minimum occurs in April with 46 GWs, with a mean value for 2040high of 166 GWs, as compared to the 175 GWs reference case.

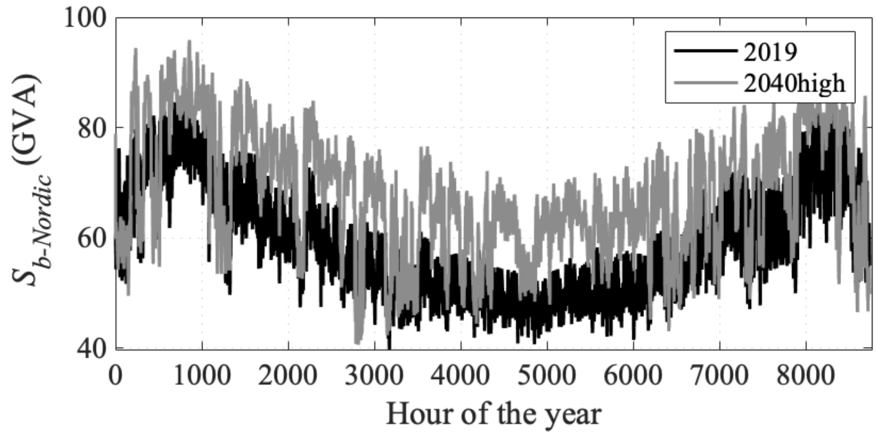

Figure 81: Power rating or online capacity in the power system, $S_{b,sys-nordic}$ for 2019/2040high.

The calculated capacity can be seen in Figure 81 below, which varies from 41 to 96, with a mean value of 68 GVA, as compared to the 66 GVA reference case.

Forecasting 2040high, SvK

From the verified model of the hydro-fleet, a scenario for 2040high can be estimated based on scenario data from SvK. From an inertia estimation of 2040high for the evaluated hour M = 4.92s and D = 0.25pu as compared to 2019 where M = 7.02s and D = 0.40pu.

The net load disturbance is generated for the stronger grid condition, from the measured PMU-data 190323 and is run in the regular grid model under weaker grid conditions, i.e. for 2040high.

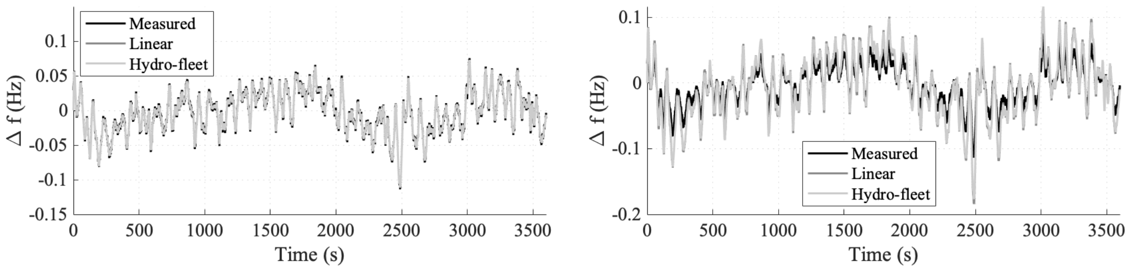

(a) Frequency data based on the 2019 SvK production data.

(b) Frequency data based on the 2040ref SvK production data estimate.

Figure 82: Frequency describing the variation between the measured and simulated frequency data, for 2019 and 2040high based on SvKs estimation for weather year 1.

The resulting frequency data is presented in Figure 82. Here, it can be seen that the frequency of the hydro-fleet estimation starts to deviate from the measured data. The PoNB for the particular hour examined is $PoNB_{2019} = 0.4\%$ for the 2019 frequency and $PoNB_{2040high} = 5.54\%$ for the 2040high estimate.

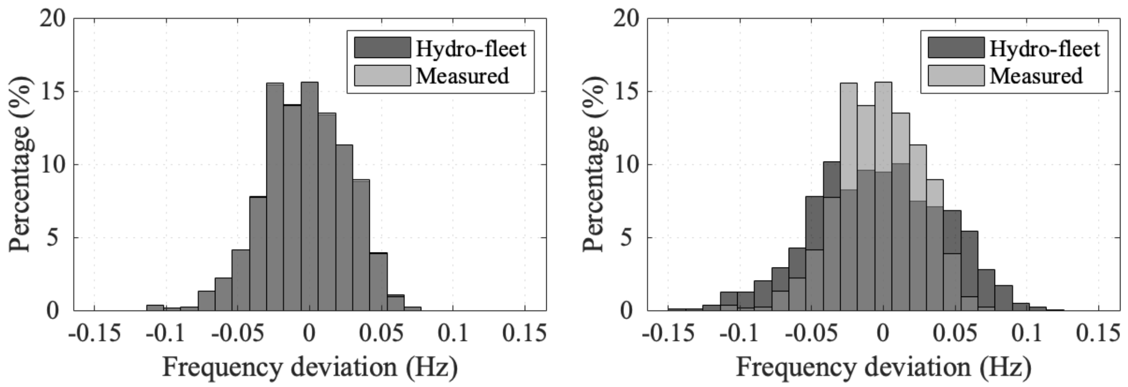

(a) Histogram based on the 2019 SvK production data.

(b) Histogram based on the 2040ref SvK production data.

Figure 83: Histograms describing the variation between the measured and simulated frequency data, for 2019 and 2040high based on SvKs estimations for weather year 1.

In Figure 83 the variation in frequency is more visible, where histograms illustrate the frequency deviations, comparing 2019 to 2040high. As can be seen the frequency deviates more from the measured frequency, since there is less inertia present in the system. Note that the span is still in normal operational conditions, but it is feasible that the deviations will increase further outside the normal band.

Scenario 2040low

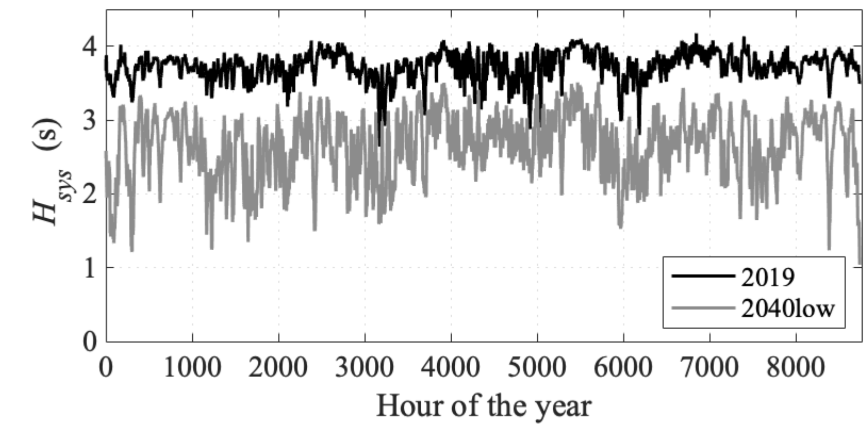

Figure 84: Power system inertia, $H_{sys-nordic}$ for 2019/2040low.

For the 2040low case the inertia estimation is presented in Figure 84. The values of $H_{sys-nordic}$ varies from 1.04 to 3.52, with a mean value of 2.64 s, as compared to the 2.64 s reference case.

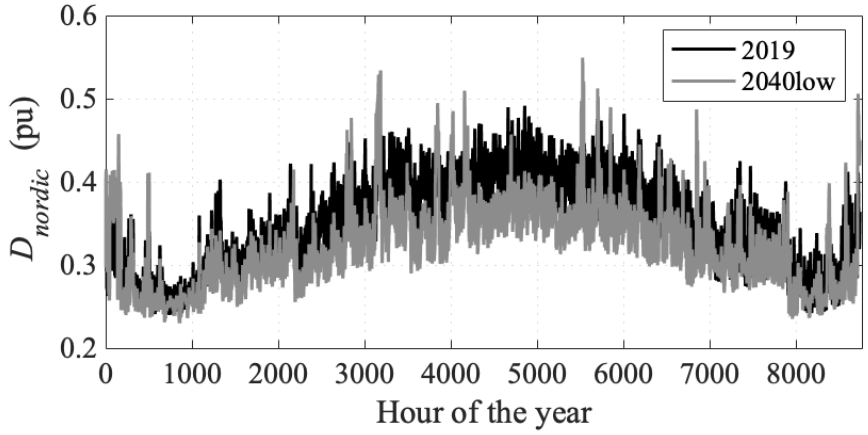

Figure 85: Power system frequency dependency, D_{nordic} for 2019/2040low.

The frequency dependency of the load for the 2019 scenario is presented in Figure 85. The values of D_{nordic} varies from 0.23 to 0.55, with a mean value of 0.32 pu, as compared to the 0.34 pu reference case.

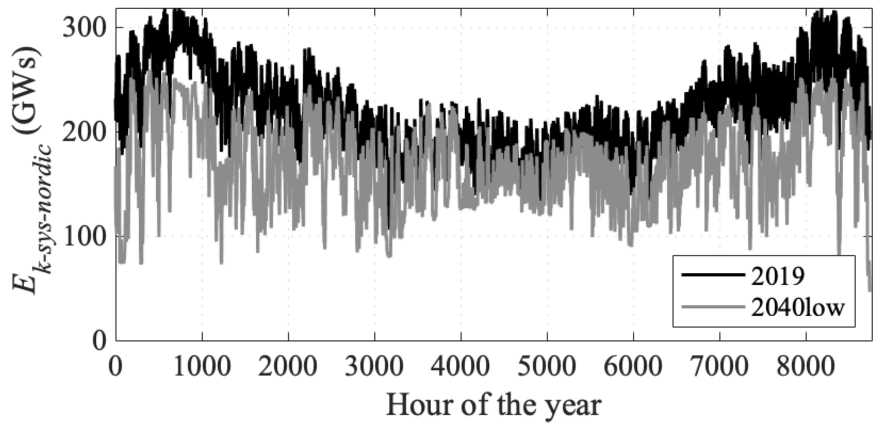

Figure 86: Power system kinetic energy, $E_{k-sys-nordic}$ for 2019/2040low.

The kinetic energy of the power system for the 2040low scenario is presented in Figure 86. As can be seen the kinetic energy peaks in December with 259 GWs and the minimum occurs in April with 46 GWs, with a mean value for 2040high of 169 GWs, as compared to the 175 GWs reference case.

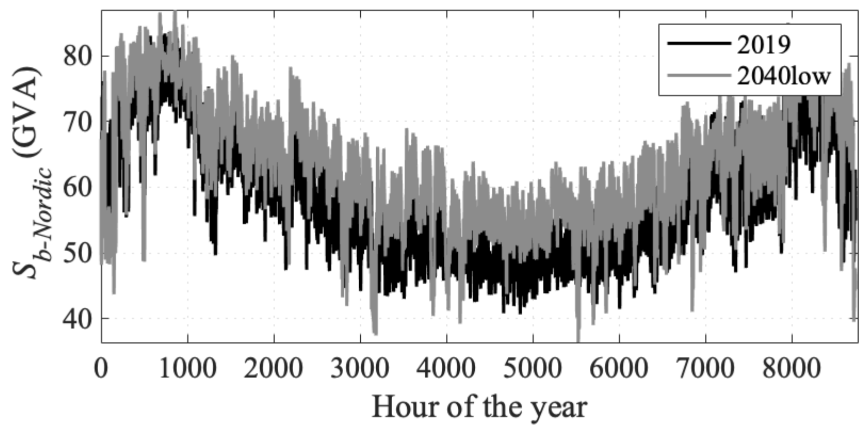

Figure 87: Power rating or online capacity in the power system, $S_{b,sys-nordic}$ for 2019/2040low.

The calculated capacity can be seen in Figure 81, which varies from 36 to 87, with a mean value of 64 GVA, as compared to the 66 GVA reference case.

Forecasting 2040low, SvK

From the verified model of the hydro-fleet, a scenario for 2040low can be estimated based on scenario data from SvK. From an inertia estimation of 2040low for the evaluated hour $M = 5.19$ s and $D = 0.25$ pu as compared to 2019 where $M = 7.02$ s and $D = 0.40$ pu. The net load disturbance is generated for the stronger grid condition, from the measured PMU-data 190323, and is run in a regular grid model under weaker grid conditions, i.e. for 2040low.

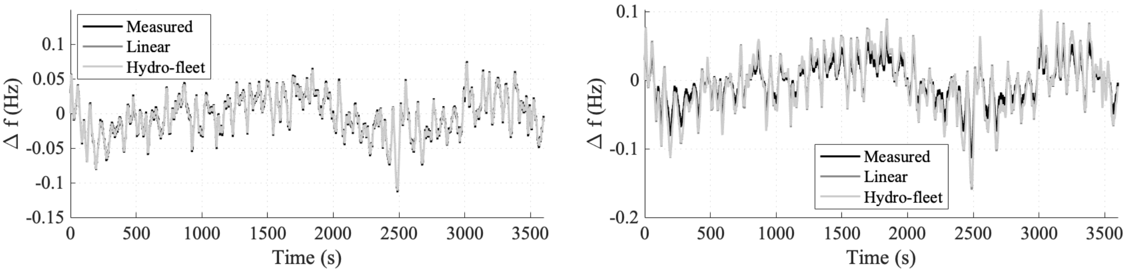

(a) Frequency data based on the 2019 SvK production data.

(b) Frequency data based on the 2040low SvK production data estimate.

Figure 88: Frequency describing the variation between the measured and simulated frequency data, for 2019 and 2040low based on SvKs estimation for weather year 1.

The resulting frequency data is presented in Figure 88. Here, it can be seen that the frequency of the hydro-fleet estimation starts to deviate from the measured data. The PoNB for the particular hour examined is $PoNB_{2019} = 0.4\%$ for the 2019 frequency data and $PoNB_{2040low} = 2.4\%$ for the 2040low estimate.

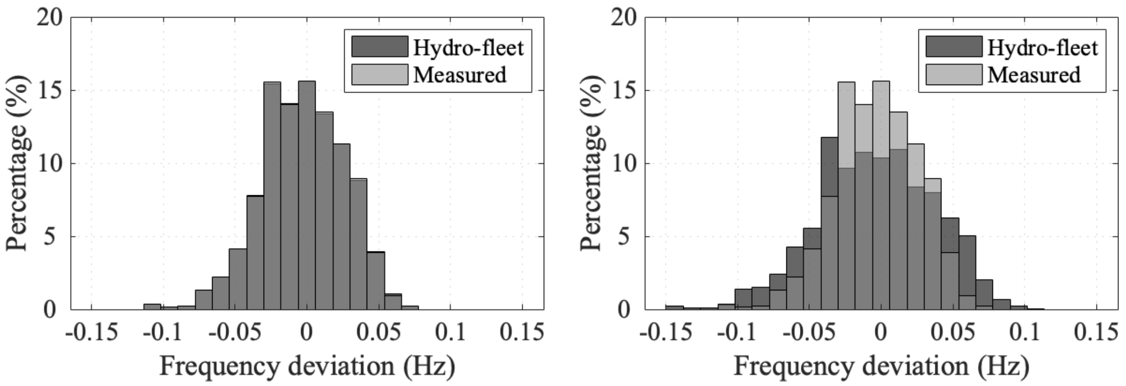

(a) Histogram based on the 2019 SvK production data.

(b) Histogram based on the 2040low SvK production data.

Figure 89: Histograms describing the variation between the measured and simulated frequency data, for 2019 and 2040low based on SvKs estimations for weather year 1.

In Figure 89 the variation in frequency is more visible, where histograms illustrate the frequency deviations, comparing 2019 to 2040low. As can be seen the frequency deviates more from the measured frequency profile, since there is less inertia present in the system. Note that the span is still in normal operational conditions, but it is feasible that the deviations will increase further outside the normal band.

Additional 2040ref estimate

In order to compare the scenario 2040ref for weather year 1 with higher wind power penetration levels, additional scenarios are evaluated.

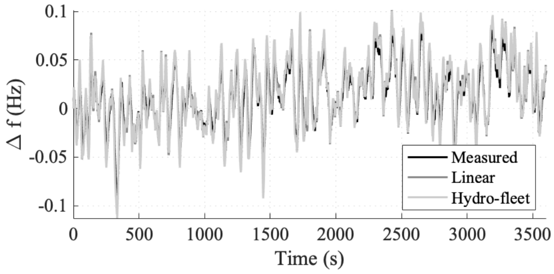

(a) Frequency data based on the 2040ref SvK production data estimate.

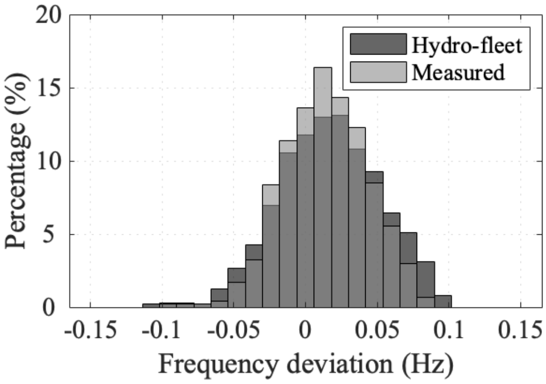

(b) Histogram based on the 2040ref SvK production data.

Figure 90: Frequency and histograms describing the variation between the measured and simulated frequency data, for 15/11-2018 and 2040ref based on SvKs estimations for weather year 1.

From the frequency data in Figure 76a) 16.00-17.00 15/11-2018 is selected which is presented in Figure 90. The inertia estimate for the 2040ref scenario is $M = 4.89$ s, $D = 0.26$ pu, $E_k = 189$ GWs, $S_b = 77$ GVA. The PoNB for the hour is 0.5%, as compared to 5.0% for the higher wind condition scenario for weather year 1.

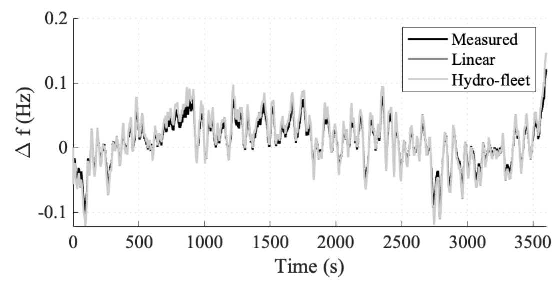

(a) Frequency data based on the 2040ref SvK production data estimate.

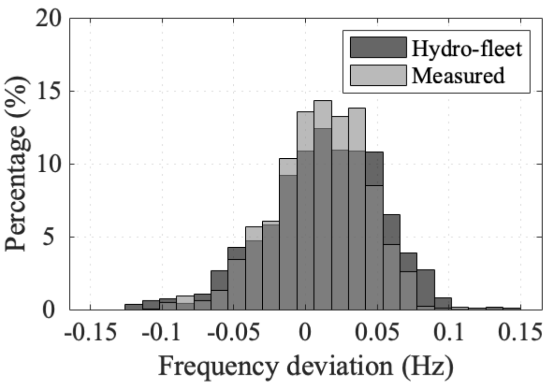

(b) Histogram based on the 2040ref SvK production data.

Figure 91: Frequency and histograms describing the variation between the measured and simulated frequency data, for 22/03-2019 and 2040ref based on SvKs estimations for weather year 1.

From the wind power production data in Figure 77 the time interval 09.00-10.00 22/3-2019 is selected for a lower wind power penetration comparison. The scenario is presented in Figure 91. The inertia estimate for the 2040ref scenario is $M = 5.81$ s, $D = 0.25$ pu, $E_k = 233$ GWs, $S_{base} = 80$ GVA. The PoNB for the lower wind scenario is 3.0% as compared to 5.0% for the higher wind condition scenario for weather year 1.

C Complete grid models

To expand on the models illustrated in the report, this section presents the complete, or full-scale models of the grid inverse and the regular grid systems.

Grid inverse

The full-scale grid inverse model is presented in Figure 92 below, to get an overview of the entire system. From the top, the two first hydro-units represent the Swedish Francis and Kaplan HPPs, the three following are the Norwegian Francis, Kaplan and Pelton HPPs and the final two represent the Finnish Francis and Kaplan HPPs. The input is the frequency signal, fed from the left, through the grid inverse and generating the net load disturbance, which is the output on the right.

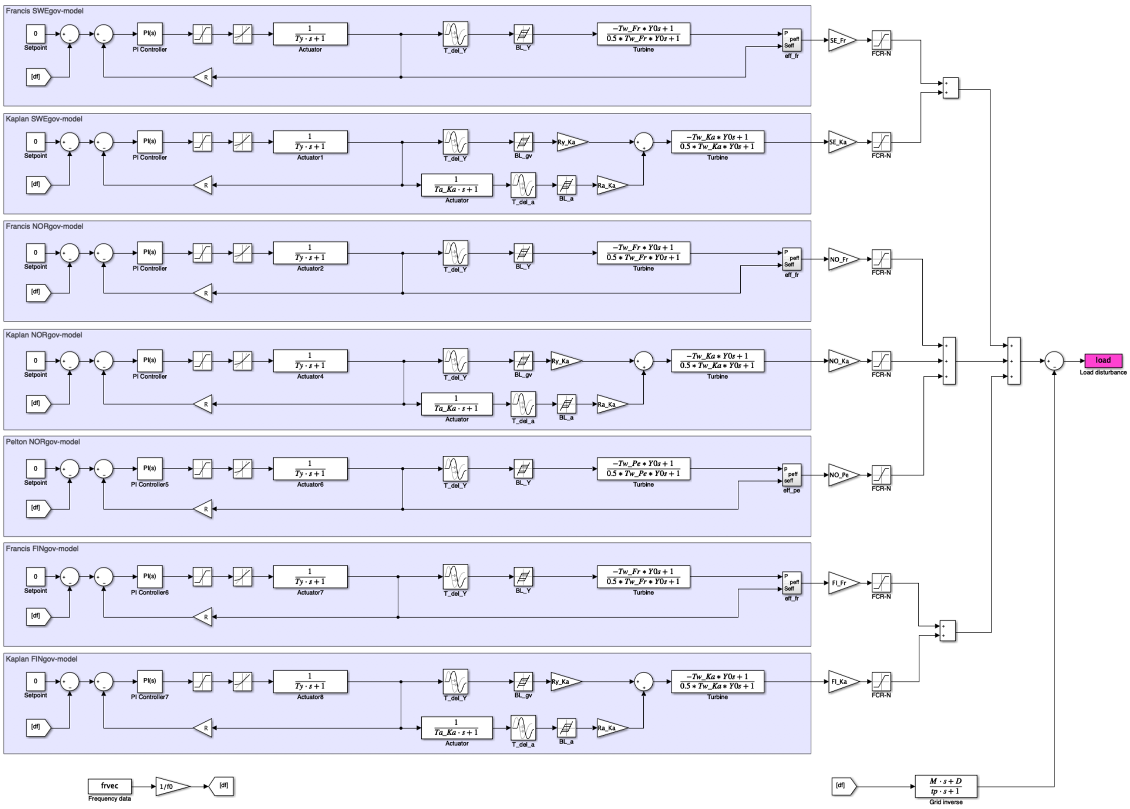

Figure 92: Full-scale grid inverse model for the NPS.

Regular grid

The full-scale regular grid model is presented in Figure 93 below, to get an overview of the entire system. From the top, the two first hydro-units represent the Swedish Francis and Kaplan HPPs, the three following are the Norwegian Francis, Kaplan and Pelton HPPs and the final two represent the Finnish Francis and Kaplan HPPs. The input is the net load disturbance, following the regular grid and generating a simulated frequency data, which is the output on the right, along with the power deviation.

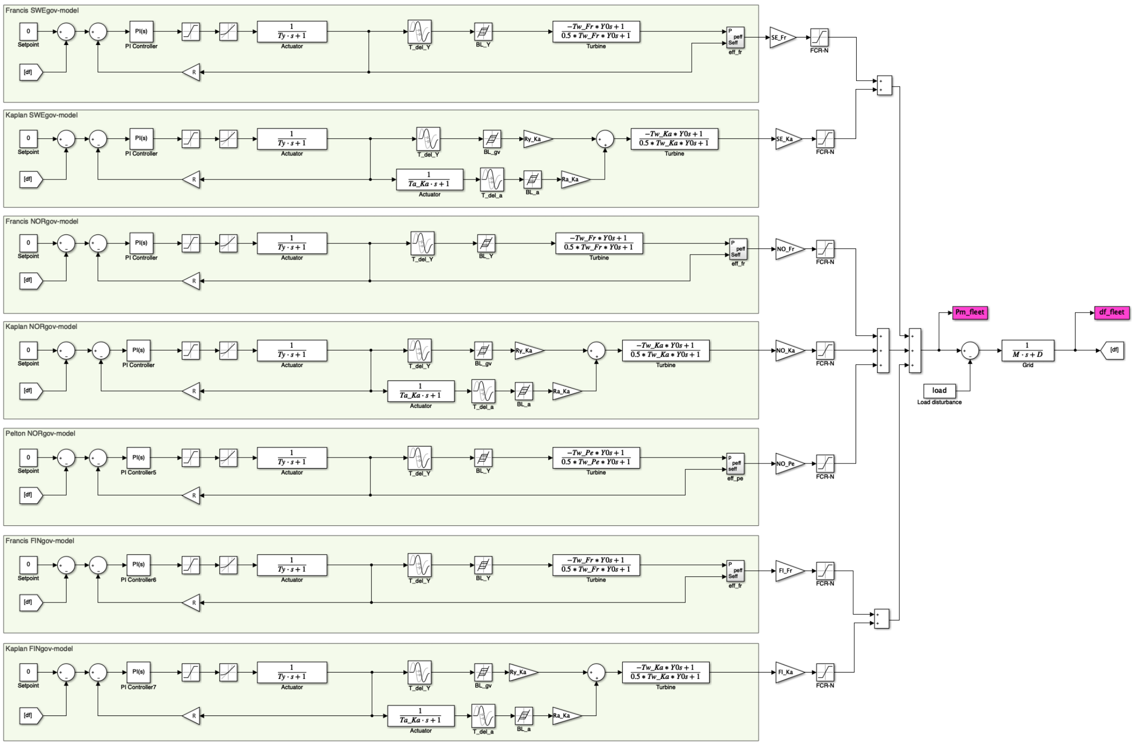

Figure 93: Full-scale regular grid model for the NPS.

D Frequency dip evaluation

To assess how the model behaves during a higher frequency deviation from the nominal, apart from the ±0.1Hz span, a frequency dip of -0.3Hz is evaluated. In Figure 94 the system experience a frequency dip that deviates outside the FCR-N region. Note that the measured frequency data is sampled at 1Hz.

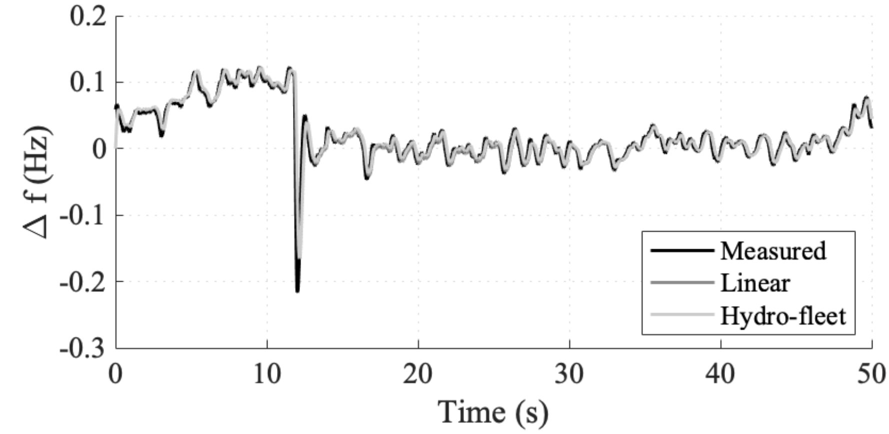

Figure 94: Frequency data for the measured and simulated models, linear and hydro-fleet model respectively during a -0.2Hz frequency dip.

As can be seen the model follows the frequency deviation well, even outside the normal operating region and the difference is ca 0.0054Hz between the measured and simulated frequency for the frequency nadir.

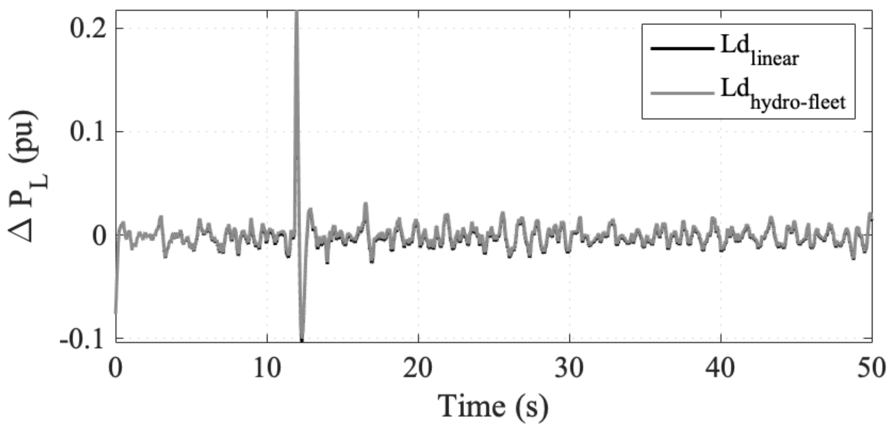

Figure 95: Net load profile for the linear and aggregated models during a -0.3Hz frequency dip.

The net load variation is presented in Figure 95, where it can be seen that the net load increases during the dip, which is expected behavior from the load profile.

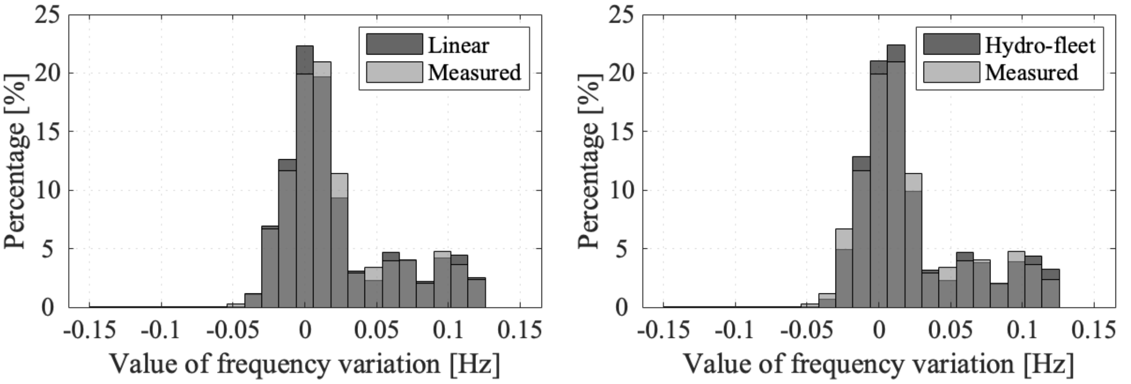

(a) Linear model compared to the measured frequency

(b) Hydro-fleet model compared to the measured frequency

Figure 96: Histograms describing the variation between the measured and simulated frequency profiles during a -0.3Hz frequency dip.

The frequency variation between the measured values and simulated model is presented in Figure 96, where it can be seen that the frequency variation overlap is almost identical.

E Kaplan turbine power alteration

In the hydro-fleet model it is assumed that the power alteration of the GVO and the runner changes are $R_Y = R_a = 0.5$, however in reality the runner blade angle is adjusted so the runner and the GVO excert an optimal behavior. Therefore the Kaplan turbine is subject to a step change for three different governor settings, to evaluate the behavior of the turbine. The first governor settings are the standard $R_Y = R_a = 0.5$, the second governor settings are $R_Y = 1$, $R_a = 0$ and the third settings are $R_Y = R_a = 0.5$ with a higher time constant for the filter of the servo runner. The initial value of the time constant is $T_\alpha = 0.4$ s, which is set to $T_\alpha = 1.0$ s instead.

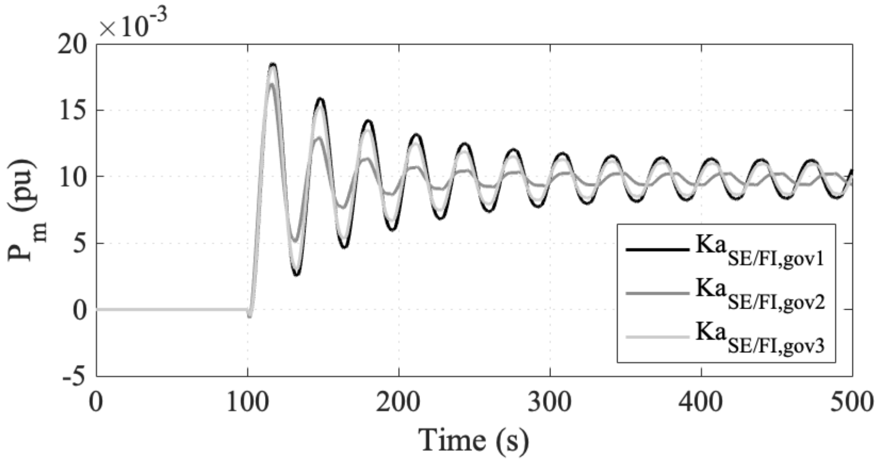

Figure 97: Power deviation after a step response for a Kaplan turbine for three different governors after a step change of (+0.01 pu).

The step change for the power deviation is presented in Figure 97. As can be seen the turbine with the second governor settings appear to deviate less during the initial step and is closer to reaching an equilibrium state than the other governor settings.

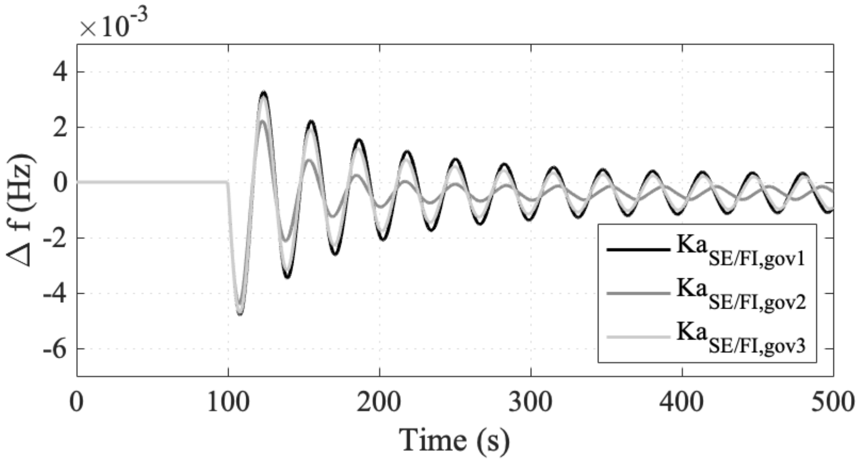

Figure 98: System frequency after a step response for a Kaplan turbine for three different governors after a step change of (+0.01 pu).

The step change for the system frequency is described in Figure 98. Similarly to Figure 97, the behavior of the second governor settings generates a lower initial frequency dip and oscillatory behavior.